

University of Strathclyde
Department of Naval Architecture, Ocean and Marine Engineering

Three-Dimensional wave measurement by image processing

Guangwei Zhao

Hydrodynamics & Ocean Renewable Energy Laboratory

May 6, 2024

This thesis is the result of the author's original research. It has been composed by the author and has not been previously submitted for examination, which has led to the award of a degree.

The copyright of this thesis belongs to the author under the terms of the United Kingdom Copyright Acts as qualified by the University of Strathclyde Regulation 3.50. Due acknowledgement must always be made of the use of any material contained in or derived from this thesis.

Abstract

The free surface of water serves as a reservoir of vital information for understanding the dynamics of oceans, making accurate measurement imperative. Various wave probes have been developed to fulfil this purpose, each employing distinct principles to capture the nuances of the free water surface. From resistance and capacitance wave probes to ultrasonic wave probes and pressure transducers, these devices provide precise measurements but are not without limitations.

In response to these challenges, researchers have sought alternative approaches, and this thesis delves into the integration of the Stereo vision principle as a contactless method for ocean wave measurement. Beyond traditional marine research, the foray of the Department of Computer Science into computer vision, emulating the human visual system, presents a unique opportunity. This interdisciplinary synergy harnesses mathematical algorithms and image processing techniques to detect objects and characters within images and videos, with applications extending to ocean and marine engineering.

The thesis unfolds with a background exploration of wave measurement techniques, comparing traditional methods with emerging optical technologies. The cross-disciplinary potential of computer vision and marine science is highlighted as a promising avenue for non-contact wave measurement, offering advancements in accuracy and efficiency. The subsequent sections detail a novel approach utilising stereo vision and structured light for contactless full-field measurement of

Abstract

water waves. This method proves adaptable, allowing customisation of measurement speed and data points, with confirmed sub-millimetre accuracy through validation tests.

A comparative analysis is provided, evaluating resistance wave probes, ultrasonic wave probes, and optical technology, offering valuable insights into wave measurement techniques. The study addresses limitations in understanding spatial distribution within an Oscillating Water Column (OWC) device, showcasing the effectiveness of optical wave measurement in exploring complex dynamics within the OWC device. Further investigations include the study of a small underwater ellipsoid in motion, providing detailed wave field results. The research chapter concludes by employing the optical measurement technique to investigate water surface height information during the entry of an underwater ellipsoid and a floating box into a lock. These findings contribute to an enhanced understanding of lock entry hydrodynamics, providing a foundation for numerical simulations and advancing knowledge in maritime engineering.

In summary, the integration of optical techniques and computer vision emerges as a transformative approach, revolutionising the study and comprehension of dynamic water surfaces in marine research.

Contents

Abstract	ii
List of Figures	vii
List of Tables	xii
Preface/Acknowledgements	xiv
1 Introduction	1
1.1 Background	1
1.2 Computer vision	2
1.2.1 Passive method	3
1.2.2 Active method	4
1.3 Literature review	6
1.4 Aims & Objectives	13
1.5 Novelty and contribution to the knowledge	13
1.6 Thesis outline	15
2 Methodology	17
2.1 Introduction	17
2.2 Principles	18
2.2.1 Stereo vision	18

Contents

2.2.2	Structured light	20
2.3	Experiment	21
2.3.1	Test facility	21
2.3.2	Experiment set up	23
2.3.3	Calibration and synchronisation	24
2.4	Validation experiment	26
2.4.1	Static validation experiment	26
2.4.2	Dynamic validation experiment	29
2.4.3	Sensitivity test	31
2.5	Measurement results	32
2.5.1	Regular wave	32
2.5.2	Irregular wave	34
2.6	Summary	37
3	Comparative analysis of optical and traditional wave measurement techniques	39
3.1	Introduction	39
3.2	Experiment setup	42
3.2.1	Calibration	44
3.2.2	Validation	46
3.2.3	Test plan	47
3.3	Results	48
3.3.1	Spatial information	48
3.3.2	Time information	52
3.4	Discussions	53
3.4.1	Resistance wave probe	54
3.4.2	Ultrasonic wave probe	55
3.4.3	Optical technology	56

Contents

3.5	Summary	57
4	Water surface inside Oscillating Water Column	59
4.1	Introduction	59
4.2	Experiment	62
4.2.1	Test facility	62
4.2.2	Model	62
4.2.3	Set up	63
4.2.4	Test plan	65
4.3	Results	66
4.3.1	Calibration uncertainty	66
4.3.2	Measured results	66
4.4	Summary	75
5	Underwater ellipsoid	77
5.1	Introduction	77
5.2	Experiment	79
5.2.1	Model	79
5.2.2	Setup	80
5.3	Results	82
5.3.1	Validation of the optical technique	82
5.3.2	Velocity measurement and results	83
5.3.3	Wave information measurement	84
5.4	Summary	92
6	Lock entry problem	93
6.1	Introduction	93
6.2	Experiment set up	95
6.2.1	Underwater ellipsoid	95

Contents

6.2.2	Floating box	96
6.3	Results	98
6.3.1	Ellipsoid	99
6.3.2	Box	103
6.4	Summary	108
7	Conclusions & Future work	111
7.1	Conclusions	111
7.2	Future improvement	115

List of Figures

1.1	Working principle of LiDAR. Figure is taken from Awange and Kiema (2019).	4
1.2	Time-multiplexing encode pattern. Figure is taken from Hall-Holt and Rusinkiewicz (2001).	5
1.3	Direct encode pattern. Figure is taken from Salvi et al. (2010). . .	6
1.4	Spatial neighbourhood encode pattern. Figure is taken from Elahi et al. (2020).	7
1.5	Results from light refraction method. Figure is taken from Gomit et al. (2013).	8
1.6	Results from TOF method. Figure is taken from Zhang et al. (2021). .	9
1.7	Results from particle motion method. Figure is taken from Fleming et al. (2018).	11
1.8	Results from WASS. Figure is taken from Bergamasco et al. (2017). .	12
1.9	Thesis outline.	15
2.1	(a) The epipolar geometry of two-view stereo vision system.(b) Pinhole model of a camera. The global coordinate is fixed on the pinhole.	18
2.2	Checkerboard pattern projected on the wavy surface.	21
2.3	Kelvin Hydrodynamics Tank. (a) Tank; (b) Wave maker; (c) Beach. . .	22

List of Figures

2.4	3D Compact Wave Tank in Kelvin Hydrodynamics Laboratory . . .	23
2.5	Experimental setup for wave measurement.	24
2.6	Binary clock. When the LED is on, it is 1, and when it is off, it is 0.	25
2.7	PVC disc with checkerboard	27
2.8	(a) Experimental setup of cylinder measurement. (b) The measured points (red dots) and the standard cylinder (blue cylinder).	28
2.9	(a) The detected points projected on a horizontal plane. (b) Comparison of measurement and theoretical motion at a fixed point in xy plane.	30
2.10	Radiated waves on the free surface.	31
2.11	Regular wave measurement result. (a) Filmed image and recognised points in camera 1. (b) Filmed image and recognised points in camera 2. (c) Reconstructed wavy surface with low-density checkerboard. (d) Reconstructed wavy surface with high-density checkerboard.	33
2.12	Irregular wave measurement result.	35
2.13	Irregular wave measurement result.	36
2.14	Comparison with ultrasonic wave probe.	37
3.1	Left: The resistance wave probe. Right: The ultrasonic wave probe.	42
3.2	Experiment setup. Left: General setup. Right: wave probes. . . .	43
3.3	Measuring position.	44
3.4	Calibration plate and set up.	45
3.5	Ultrasonic wave probe calibration	45
3.6	(a) Test 01; (b) Test 07; (c) Test 16.	51
3.7	Wavefield measurement results of the optical technique. Left: crest; Right: trough.	52

List of Figures

3.8	Close-up examination of one peak in the measurement results of Test 16.	54
4.1	OWC model used in the test.	62
4.2	Experiment setup of the OWC.	64
4.3	Comparison of measurement results.	68
4.4	Response Amplitude Operator (RAO) of these two wave measurement techniques.	70
4.5	Water surface inside the OWC in one wave period (T_p).	74
5.1	The ellipsoidal model maintains neutral buoyancy in water.	79
5.2	Details of the experimental setup, the red line indicates the projection area on the water surface.	80
5.3	Projector (left) and cameras (right) used for the stereo vision system.	81
5.4	When the speed is 0.187m/s, the measured time history data of a specific point on the centre line. (a) Data for the entire movement. The vertical cursors indicate the period during which the ellipsoid passes through the measurement area. (b) Zoom in to the range within the cursors.	85
5.5	When the speed is 0.187m/s, the measured spatial data. The number only represents the order of each frame and does not refer to the frame number in the video.	86
5.6	Wave Field Measurement at Velocity 0.187 m/s: Entering Moment (Upper Left), Model Arrival at Middle (Upper Right), Leaving Moment (Lower Left), Model Fully Exiting (Lower Right)	87

List of Figures

5.7	When the velocity was 0.305 m/s, the measured time history data of a specific point on the centre line. (a) Data for the entire movement. The vertical cursors indicate the period during which the ellipsoid passes through the measurement area. (b) Zoom in to the range within the cursors.	88
5.8	When the velocity was 0.305 m/s, the measured spatial data. The number only represents the order of each frame and does not refer to the frame number in the video.	89
5.9	Wave field measurement at the velocity equal to 0.305 m/s.	91
6.1	Ellipsoid inside the lock area.	96
6.2	Measurement points inside the lock area.	96
6.3	Floating box entering the lock.	98
6.4	Experiment setup for measuring the water surface inside the lock area	99
6.5	Time history results of $Wp2$ and $Wp3$	100
6.6	Measured result of the ellipsoid entering the lock under 1m water depth condition. (a) $F_r = 0.051$; (b) $F_r = 0.136$	101
6.7	Measured result of the ellipsoid entering the lock with the step bottom under different speeds.	102
6.8	Wave probe result of the box entering the lock with and without seeding. (a) $F_r = 0.021$; (b) $F_r = 0.062$	104
6.9	Wave probe result of the box entering the lock at different speeds.	106
6.10	Wave field measurement results. From box entry to Piston phenomenon occurs.	107
6.11	Resistance and moment of the box entering the lock at different speeds	108
6.12	Wave and resistance of the box entering the lock at different speeds.	109

List of Figures

7.1 New cameras set up in the future. 116

List of Tables

2.1	Average of distances between points	28
3.1	Different wave measurement techniques Validation	47
3.2	Test matrix.	48
4.1	Geometry details of the OWC	63
4.2	Test matrix for OWC	66
4.3	Calibration of the Ultrasonic wave probe and optical method . . .	67
4.4	The water column motion amplitude obtained after <i>sine</i> fitting of the measurement results	68
5.1	Velocity measurement	84
6.1	Geometry details of the box and lock	97

Preface/Acknowledgements

I extend my profound gratitude to my supervisor, Dr Zhiming Yuan, whose unwavering support, insightful guidance, and scholarly expertise have been indispensable throughout this doctoral journey. His mentorship not only shaped the content of this thesis but also provided me with the opportunity to navigate the challenging path towards earning my Ph.D. Without his invaluable assistance, this accomplishment would not have been possible.

I express my sincere appreciation to Dr Saishuai Dai, my line manager in the part-time Research Assistant role. His constructive feedback and role as the director of the Kelvin Hydrodynamics Laboratory have played a pivotal role in enhancing my experimental skills. Dr. Dai's leadership and provision of opportunities for diverse experiments have been instrumental in the development of this research.

Special thanks are extended to Dr Laibing Jia for his intellectual support during my PhD study. His profound insights and assistance were invaluable in overcoming challenging problems encountered in the course of my experimental work.

Heartfelt thanks are extended to the Department of Naval Architecture, Ocean & Marine Engineering and the University of Strathclyde for creating a conducive academic environment and providing the essential resources for this research.

I am deeply grateful to my friends, Mr Yi Huang, Mr Wenxuan Xia, Dr

Preface/Acknowledgements

Yihan Liu, Dr Momchil Terziev, and Dr Roberto Ravenna, whose camaraderie has made my PhD journey more engaging and manageable. Their support and shared experiences have been a source of encouragement.

To my family, I extend my sincere appreciation for their unwavering support and encouragement, which have served as a constant pillar sustaining me through the peaks and troughs of this academic pursuit. Their steadfast belief in my capabilities has been a driving force.

Lastly, I acknowledge the invaluable assistance provided by the Kelvin Hydrodynamic staff – Mr Steven Black, Mr Grant Dunning, Mr Bill Wright, and Mr Martin Dowling. Their contributions and collaboration have enriched the outcomes of this research, and I am sincerely grateful for their support.

Chapter 1

Introduction

1.1 Background

The free surface of water holds a wealth of valuable information crucial for marine research. Accurate measurement of water surface information is an essential component of this endeavour, and various types of wave probes have been developed to fulfil this purpose(Lange et al., 1982). These probes employ distinct principles to capture the dynamics of the free water surface. One such device is the resistance wave probe, which relies on changes in resistance of the device at different water surface heights to glean information about the water level. Capacitance wave probes operate on a similar principle but measure capacitance instead of resistance. In contrast, the ultrasonic wave probe harnesses the time-of-flight principle, leveraging the speed of ultrasonic waves to calculate the distance between the probe and the water surface, ultimately providing data on water surface motion. In coastal engineering, pressure transducers placed at the water bottom are used to measure wave height. While these wave probes offer precise and stable measurements, they are not without limitations, including the inability to determine wave direction, limited measurement points, and specific hardware

Chapter 1. Introduction

requirements. In response to these challenges, some researchers opt to deploy multiple wave probes at distinct locations within a wave field to gather comprehensive data. Recent technological advancements have kindled the exploration of more efficient methods to obtain these critical measurements. One such alternative approach, proposed in the last century, involves Doppler sonar technology for contactless ocean wave measurement (Pinkel and Smith, 1987).

The Department of Computer Science has ventured into the field of computer vision, which aims to emulate the human visual system. This interdisciplinary field leverages mathematical algorithms and image processing techniques to detect objects and characters within images and videos while also offering the capability to reconstruct three-dimensional information about objects (Szeliski, 2022). Although computer vision primarily originated for solid object detection, its potential applications extend to the Department of Ocean and Marine Engineering. Here, the integration of computer vision techniques presents an innovative approach to wave surface measurements. By harnessing the power of computer vision, researchers can explore non-contact methods of capturing wave motion data, opening up new avenues for enhancing the accuracy and efficiency of oceanographic research. This cross-disciplinary synergy between computer vision and marine science has the potential to revolutionise the way of studying and understanding the dynamic behaviour of water surfaces.

1.2 Computer vision

Computer vision in the context of 3D reconstruction encompasses a diverse array of algorithms, each grounded in distinct principles and methodologies. This field is paramount in computer science and engineering due to its ability to transform 2D images into comprehensive 3D models. The algorithms employed for this purpose can be broadly categorised into two primary classes: active and passive

(Zhang, 2018), each with its unique attributes and applications. The distinction between active and passive 3D reconstruction methods forms the bedrock of this research domain, allowing us to explore their respective advantages and limitations.

1.2.1 Passive method

Passive methods predominantly employ the stereo vision principle in stereopsis. The critical phases of the stereopsis process, as outlined by Dhond and Aggarwal (1989), encompass preprocessing, establishing correspondence, and recovering depth information. Within this framework, image preprocessing assumes a central role, involving the identification of image locations meeting specific feature characteristics.

In the earlier iterations of stereo algorithms, there was a reliance on area-based matching schemes, aligning area patches from two images (Gennery, 1979). However, in contemporary stereo algorithms, there is a prevailing preference for direct feature matching, highlighting the increased significance of robust feature detectors. Recognition of physical discontinuities in a scene, typically manifesting as local changes in grey-level intensity in an image, has resulted in a heightened dependence on edges as matching primitives (Marr and Hildreth, 1980; Canny, 1986).

Emphasising the pivotal nature of the matching stage in stereo computation, when confronted with two or more views of a scene, the establishment of correspondence among homologous features becomes imperative. These features signify the representation of the same physical entity in each view. The realisation of depth information recovery will be expounded upon in subsequent sections of this thesis.

1.2.2 Active method

Active methods for 3D measurement primarily rely on Time-of-Flight (TOF) technology or structured light technology. In TOF-based systems, cameras equipped with either infrared (IR) or laser light sources emit light pulses, which are subsequently reflected back from the surface of the object to the camera. Measuring the time it takes for the light to return to the camera enables the calculation of the distance to the measurement point. Notably, certain TOF cameras are equipped with a built-in function that can transmit infrared (IR) light and measure the phase delay of the reflected infrared light emitted by the cameras themselves (Hansard et al., 2012). With knowledge of the phase delay, the time of reflection can be accurately determined, allowing the camera to generate results that incorporate the distance to the measurement surface. Utilising this distance information, the three-dimensional shape of the object can be reconstructed, with the camera serving as the coordinate origin for extracting the necessary data. LiDAR technology is a prominent application of this TOF-based approach (Awange and Kiema, 2019).

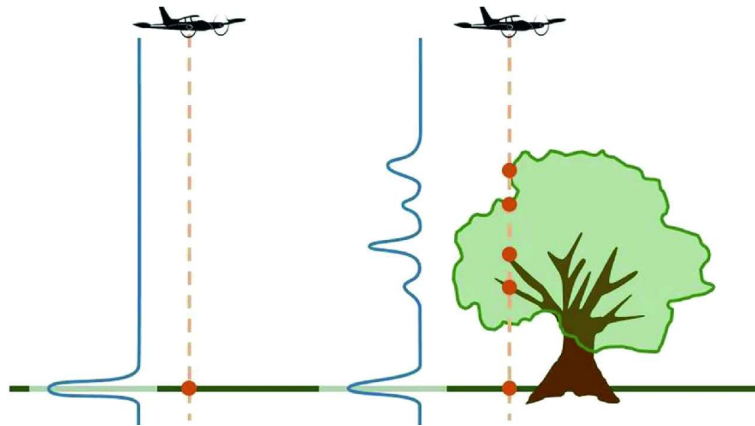


Figure 1.1: Working principle of LiDAR. Figure is taken from Awange and Kiema (2019).

Structured light technology, on the other hand, involves the active projection

Chapter 1. Introduction

of structured patterns onto the surface of the object using a specialised projection device (Zhang, 2018). These projected patterns carry encoded information, which in turn enhances the accuracy of matching results. As the projected pattern conforms to the shape of the object, capturing the area covered by the pattern with a camera and analysing the distortion of the pattern, along with the known encoding information, allows for the computation of three-dimensional information pertaining to the measurement object.

Presently, structured light pattern encoding strategies can be primarily classified into three categories: time-multiplexing, direct codification, and spatial neighbourhood methods (Pages et al., 2003). The time-multiplexing strategy encodes information based on time, involving the projection of a series of patterns onto the object and the subsequent analysis of the temporal encoding information of each pixel (Posdamer and Altschuler, 1982; Valkenburg and McIvor, 1998; Mimou et al., 1981; Caspi et al., 1998; Horn and Kiryati, 1999; Gühring, 2000; Bergmann, 1995; Hall-Holt and Rusinkiewicz, 2001). This approach is known for its ease of implementation and its ability to achieve high accuracy and resolution performance. However, it may not be suitable for measuring water surfaces due to its inability to respond to rapid changes.

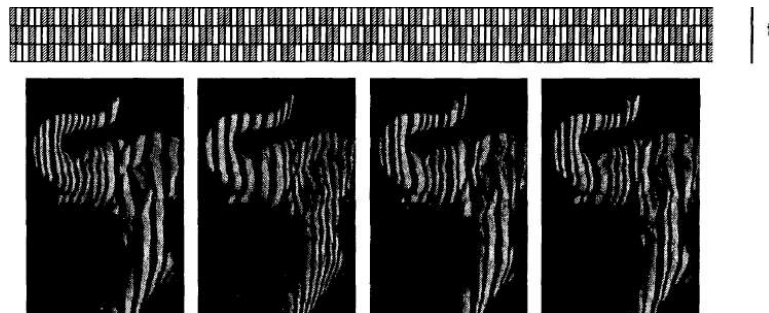


Figure 1.2: Time-multiplexing encode pattern. Figure is taken from Hall-Holt and Rusinkiewicz (2001).

In contrast, the direct encoding strategy assigns a specific feature, such as

colour or grayscale, to each pixel of the projected pattern (Carrhill and Hummel, 1985; Hung, 1993; Tajima and Iwakawa, 1990; Sato, 1999; Salvi et al., 2010). The information is then analysed to achieve matching without the need for temporal changes. Nevertheless, this strategy requires that the feature points remain nearly constant throughout the entire process, limiting its applicability in wave measurement scenarios.

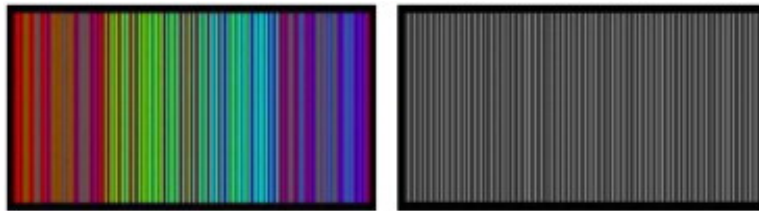


Figure 1.3: Direct encode pattern. Figure is taken from Salvi et al. (2010).

The spatial neighbourhood strategy combines the information from surrounding pixels to identify matching points (Boyer and Kak, 1987; Ito and Ishii, 1995; Maruyama and Abe, 1993; Zhang et al., 2002; Salvi et al., 1998; Vuylsteke and Oosterlinck, 1990; Morano et al., 1998; Elahi et al., 2020). It does not impose strict requirements on feature points over time, making it suitable for dynamic measurements. However, it necessitates the completeness of the pattern, demanding additional attention during wave measurement procedures.

1.3 Literature review

In the field of optical techniques for measuring water surfaces, several innovative techniques have emerged, each offering unique advantages and challenges. These methods are employed to ascertain various aspects of water surface characteristics, providing valuable insights for research and practical applications. This section will delve into these optical methodologies, elucidating their principles, related studies, and limitations.

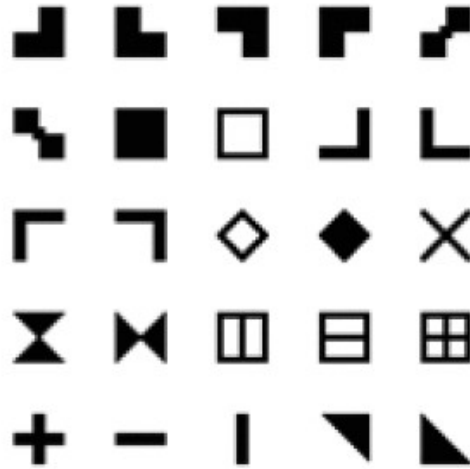


Figure 1.4: Spatial neighbourhood encode pattern. Figure is taken from Elahi et al. (2020).

One prominent optical approach is predicated upon the phenomenon of light refraction through the air-water interface. A seminal study by Zhang and Cox (Zhang and Cox, 1994) exemplifies this technique. They positioned a camera above the water surface and a coloured source screen beneath a large horizontal underwater lens. The gradient of the wave elevation was quantified by observing the camera image of the coloured source screen in detail. Moisy et al. (Moisy et al., 2009) developed a method known as free-surface synthetic Schlieren (FS-SS). It relied on digital image correlation (DIC) algorithms to reconstruct wave height. By analysing the displacement between a reference image and the refracted image of a random point pattern through the interface, this approach facilitated the water surface measurements. Gomit et al. (Gomit et al., 2013) also adopted a similar principle, projecting a laser sheet below the free surface and employing three cameras for data capture. Two cameras were used to capture the refraction image from different viewpoints above the water surface. Another camera was placed under the transparent test chamber to record the reference image. However, it is imperative to acknowledge the limitations of this method.

Chapter 1. Introduction

The position of refraction points may not match the reference points because of the strong curvature of the interface. There is also a limitation associated with the angle of the incident light and the orientation of the surface, which may cause measurement problems.

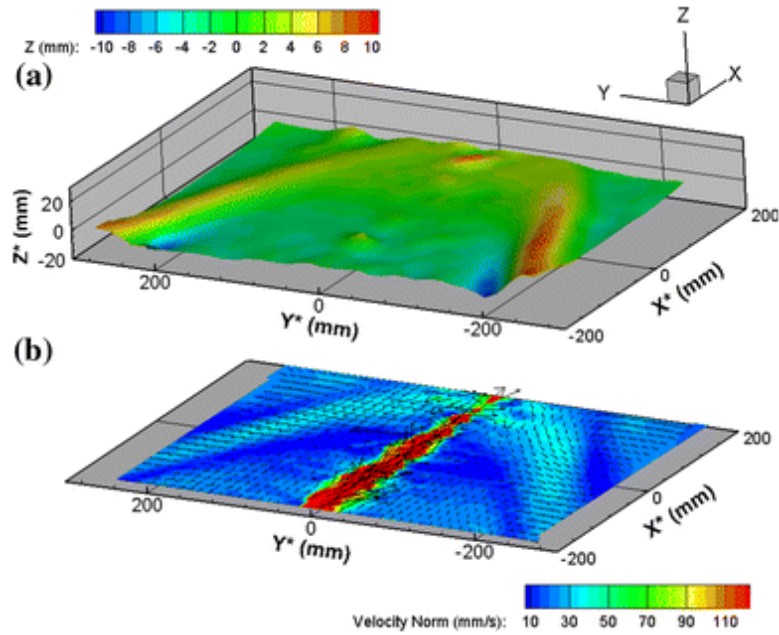


Figure 1.5: Results from light refraction method. Figure is taken from Gomit et al. (2013).

The other optical technique for the measurement of water surfaces revolves around the time-of-flight (TOF) principle, with LiDAR technology serving as a prime illustration of this approach, as elucidated by Awange and Kiema (2019) in their study. LiDAR systems emit specific light sources towards the surface of objects and subsequently gauge range information by evaluating the duration it takes for the light to return after interacting with the target. Recent advancements in this field, as demonstrated by Zhang et al. (2021), have introduced a technique that integrates a Single Photon Avalanche Diode (SPAD) detector array in the laboratory. In this technology, an independent light source (solid-state laser) is used to illuminate the water surface. The emitted laser pulses interact

with the water surface and are subsequently reflected back towards the SPAD detector array, which is capable of capturing and registering individual photons of the reflected light. By analysing the time interval between the emission of the laser pulse and the detection of the reflected photon by the SPAD array, precise information regarding the elevation of the water surface can be derived. Although this method is widely used at present, one notable limitation is the dependency on the availability of sufficient reflected light for accurate measurement. In scenarios where the sensor cannot receive an adequate quantity of reflected photons, such as when measuring extremely turbid or optically challenging water bodies, the accuracy of the water surface information may be compromised.

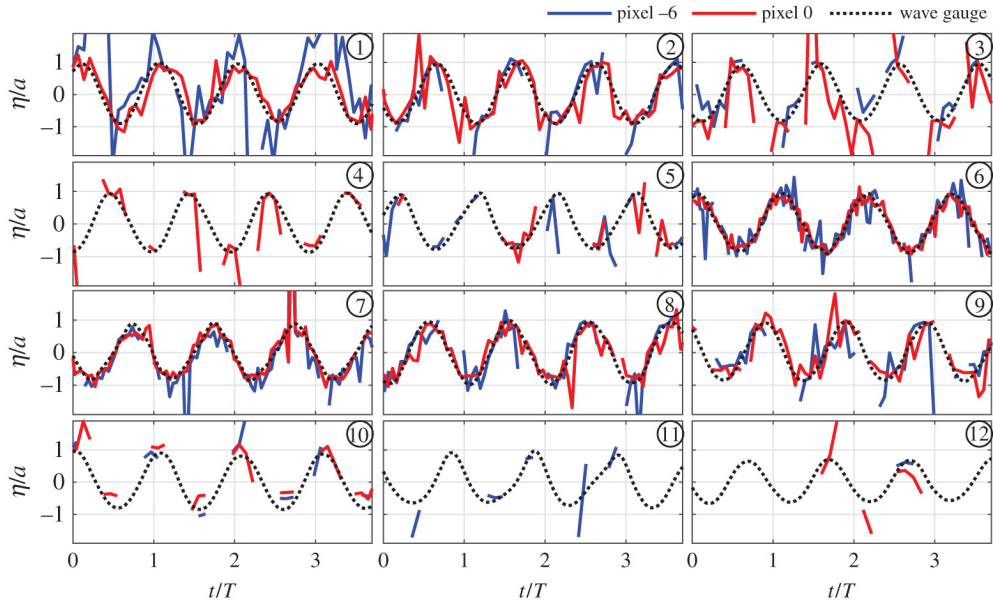


Figure 1.6: Results from TOF method. Figure is taken from Zhang et al. (2021).

Another method measures the water surface by analysing the location of the floating particles. Douxchamps et al. (Douxchamps et al., 2005) used 9mm diameter white wooden beads as tracer particles. Employing stereo measurements, an antidune flow pattern was reconstructed. This technique provided insights into the dynamic behaviour of water surfaces by tracking the movement

Chapter 1. Introduction

of these particles. Building upon this foundation, Fleming et al. (Fleming et al., 2018) advanced this particle-based approach through the utilisation of proprietary videogrammetry software, DaVis. They conducted post-processing of stereoscopic images obtained from multiple synchronised machine vision cameras. To enhance the visibility and trackability of particles, ultraviolet light served as the primary source of illumination, exciting fluorescent flakes dispersed within the fluid. A high-pass filter was employed to selectively capture the fluorescence, resulting in improved data quality and accuracy. So far, the floating particles technology can give a decent result but it is constrained to scenarios where floating particles are naturally present or can be introduced. Moreover, the use of tracer particles introduces considerations related to particle size, which may necessitate careful calibration and correction to account for systematic errors in measurements. Additionally, practical concerns such as safety protocols for the handling and dispersion of tracer particles, as well as the need for subsequent cleanup, should be taken into account when employing this method.

In addition to the previously mentioned methodologies for water surface measurement, several alternative technologies have been devised by researchers, each offering unique capabilities and insights into the complex dynamics of water surfaces. One such innovative contribution to the field is the work of Bergamasco et al. Bergamasco et al. (2017), who have developed a powerful open-source software known as WASS, an acronym for Wave Acquisition Stereo System. This software represents a significant advancement in water surface analysis, as it autonomously generates stereo image estimations and dense point clouds. It achieves this by leveraging a fast 3D dense stereo reconstruction process, drawing upon the robust capabilities of the OpenCV library. Tsubaki and Fujita Tsubaki and Fujita (2005) proposed a method which involves the introduction of an opaque-white dye into the water, coupled with the projection of a random pattern onto the surface.

Chapter 1. Introduction

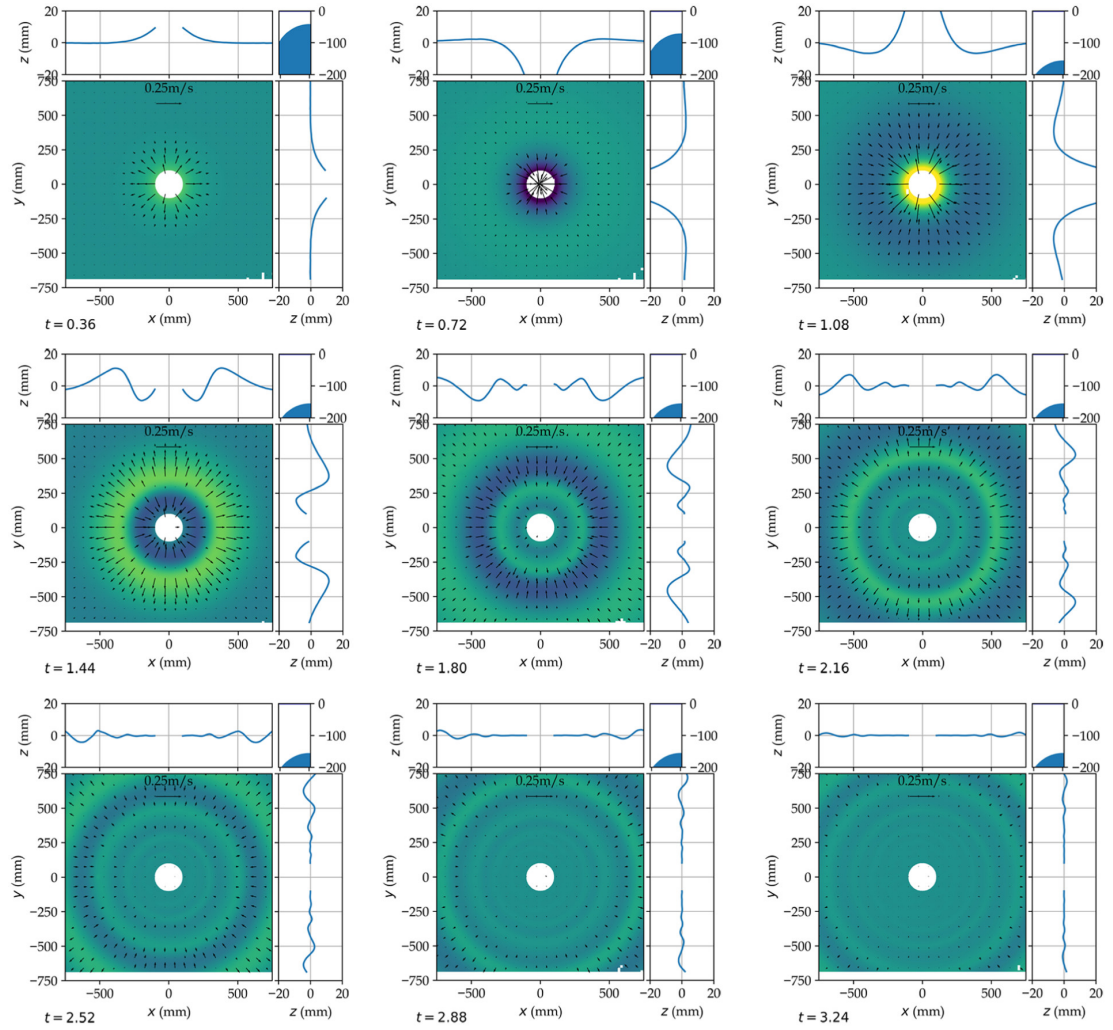


Figure 1.7: Results from particle motion method. Figure is taken from Fleming et al. (2018).

The wavy surface was then reconstructed by a technology based on stereo vision. Cochard and Ancey Cochard and Ancey (2008) have contributed to the field through the development of technologies rooted in fringe projection profilometry. This method relies on the projection of fringe patterns onto the water surface, which are subsequently analysed to derive information about surface profiles and deformations. Aureli et al. (Aureli et al., 2011) implemented a light absorption based method for measuring the water surface in rapidly changing flows. The core

1.4 Aims & Objectives

This PhD project proposed a method capable of measuring deformations in the water surface by image processing. The final aim is to apply this method to some practically relevant problems. So far, this research includes the following objectives:

- To validate the accuracy of the proposed method both on the solid wavy surface and the free water surface.
- To find out the sensitivity and limitations of the method.
- Extend the capability of the method to a variety of practical problems and demonstrate its use.

1.5 Novelty and contribution to the knowledge

Novelty of the research

- This thesis introduces a novel optical wave measurement method that integrates stereo vision and structured light techniques. Successfully implemented at the Kelvin Hydrodynamics Laboratory, this method has been utilised across various scenarios.
- The proposed optical method offers adjustable spatial density wave field measurements. In comparison to conventional wave measurement techniques, it is cost-effective and non-disruptive to the water surface.
- With no requirement for high-power light sources, this method poses no safety hazards to experiment operators. The light source employed in this technique is harmless.

Chapter 1. Introduction

- Notably, this is the first work within the laboratory that eliminates the need for water treatment. It relies solely on ambient dust, rendering it an environmentally friendly approach.
- Within this thesis, diverse scenarios have been investigated using the optical technique, providing detailed spatial wave field results to enhance understanding of hydrodynamic phenomena.

Contribution to the knowledge

- The thesis conducts a comparative analysis of the proposed optical technique against traditional wave measurement methods. The advantages and disadvantages of each technique are discussed, aiding researchers in selecting the most suitable approach for their experimental requirements.
- Complete measurement of the water surface within an Oscillating Water Column has been achieved, offering insights into the behaviour of water columns within such devices. This contributes to the advancement of future Wave Energy Converter development.
- Measurement of Kelvin wake and Bernoulli hump generated by a moving ellipsoid is presented, with detailed wave field results provided. In contrast to KCS ship wave field measurements, this optical technique reduces the huge amount of effort and yields superior results.
- The thesis captures the piston phenomenon of fluid inside a lock during the entry processes of an ellipsoid and a box. This phenomenon, characterised by the simultaneous rising and falling motion of the free surface, aids in understanding the unsteady effects of free surfaces and the impacts of sudden waterway constriction and lock gate closure.

1.6 Thesis outline

This thesis introduces a novel wave measurement method and presents case studies demonstrating its efficacy in collecting experimental data. The cases encompass both wave measurements conducted in open water areas and those within specific structures, providing a comprehensive assessment of the capabilities of the method. The thesis is organised into several sections, as outlined in Figure 1.9:

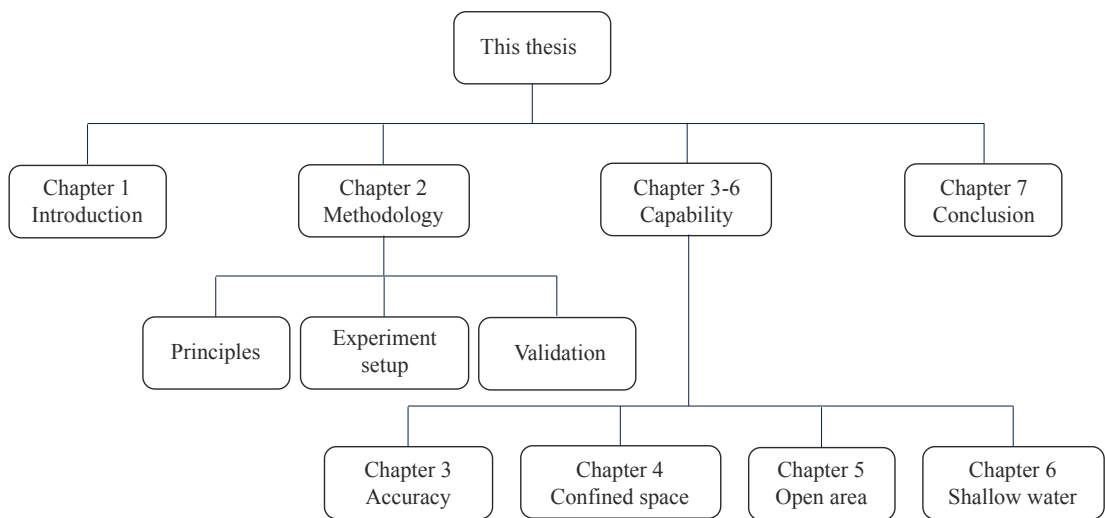


Figure 1.9: Thesis outline.

In this research, the proposed wave measurement method is detailed, along with the experiments conducted to validate its effectiveness. Comparative analyses are performed between traditional wave measurement methods and the proposed approach to highlight its advantages.

Furthermore, the application of the method within Oscillating Water Column (OWC) systems is explored, demonstrating its utility in confined water surface conditions. Additionally, the method is extended to measure steady waves generated by moving underwater objects, showcasing its adaptability to varying hydrodynamic scenarios, including the free surface behaviour observed when

Chapter 1. Introduction

underwater objects and floating boxes enter locks. The thesis concludes with a summary of the findings and outlines avenues for future research.

Chapter 2

Methodology

2.1 Introduction

The proposed optical technique combines active and passive 3D reconstruction methodologies to effectuate non-intrusive, comprehensive measurements of water wave phenomena. To facilitate this, structured spatial patterns are projected onto the water surface through the application of the spatial neighbourhood technique, thereby furnishing a reliable and controllable grid of measurement points. This intricate pattern adheres to the contours of the water surface, permitting variable point densities to be captured by stereo cameras across the entire expanse of the observed field. This fusion of active and passive scanning techniques serves to surmount the challenges associated with point detection and matching encountered in stereo vision applications. The integration of stereo vision ensures homogeneity and stability to the measurement process across the entire field of view.

2.2 Principles

2.2.1 Stereo vision

For the passive method-stereo vision technology, the epipolar geometry is used (Hartley and Zisserman, 2003), and the principal points are P_1 and P_2 , respectively. A point in space X is projected on image planes C_1 and C_2 marked with x_1 and x_2 , respectively. C_1, C_2, P_1, P_2 and X are coplanar, called the epipolar plane. Cameras are modelled with a pinhole model, which is a good approximation for a lens-based camera in mid and long focal lengths, as shown in Figure 2.1 (b). In this model, the image is projected on the image plane through a ray across the pinhole. Another plane is considered symmetrical with the pinhole image plane. On this plane, the projection relationship is similar to the image plane, but the image is erect, and this plane is exactly the C_1 and C_2 planes in Figure 2.1 (a).

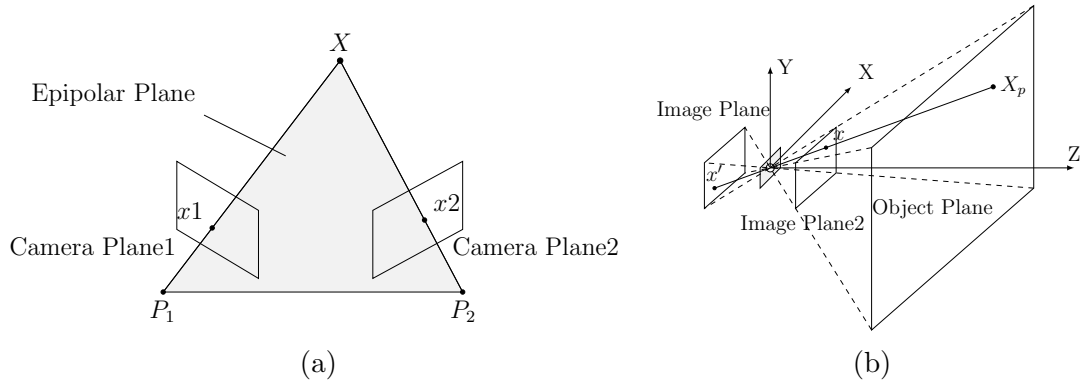


Figure 2.1: (a) The epipolar geometry of two-view stereo vision system.(b) Pin-hole model of a camera. The global coordinate is fixed on the pinhole.

Figure 2.1 (b) shows the global coordinate. Using homogeneous coordinates, spatial point $X(X, Y, Z, 1)$ project on two cameras $x_1(x_1, y_1, 1)$ and $x_2(x_2, y_2, 1)$. From

our camera model, the point projection relation can be written as:

$$\begin{bmatrix} x \\ y \\ 1 \end{bmatrix} = \begin{bmatrix} \frac{f}{Z} & 0 & 0 & 0 \\ 0 & \frac{f}{Z} & 0 & 0 \\ 0 & 0 & \frac{1}{Z} & 0 \end{bmatrix} \begin{bmatrix} X \\ Y \\ Z \\ 1 \end{bmatrix} \quad (2.1)$$

where f is the focal length of the camera model, defined as the distance between the image plane and pinhole. The relation between image coordinates x, y and pixel coordinates u, v can be written as:

$$\begin{bmatrix} u \\ v \\ 1 \end{bmatrix} = \begin{bmatrix} \frac{1}{dx} & -\frac{1}{dx \tan \theta} & u_0 \\ 0 & \frac{1}{dy \sin \theta} & v_0 \\ 0 & 0 & 1 \end{bmatrix} \begin{bmatrix} x \\ y \\ 1 \end{bmatrix} \quad (2.2)$$

where du and dv are pixel widths in the u and v directions. The intrinsic parameter matrix for the pinhole model can be defined as:

$$K = \begin{bmatrix} f_x & s & u_0 \\ 0 & f_y & v_0 \\ 0 & 0 & 1 \end{bmatrix} \quad (2.3)$$

In this matrix, f_x and f_y represent the pixel focal length on the camera's axis direction and a projection transform. u_0 and v_0 are principal points under the pixel coordinate and represent a transition transform from the camera coordinate to the pixel coordinate. s is the skewness factor, which represents the skew of the camera. The intrinsic matrix is described by camera properties like focal length, principal point position, and pixel size describe the intrinsic matrix.

To represent the camera location, another matrix called the extrinsic matrix is needed. The coordinate of camera one is fixed as a global coordinate if the

coordinate of camera two can transform to the global coordinate through 3x1 transition vector T and a 3x3 rotation matrix R , the extrinsic matrix for both two cameras can be written as:

$$M_1 = \begin{bmatrix} 1 & 0 & 0 & 0 \\ 0 & 1 & 0 & 0 \\ 0 & 0 & 1 & 0 \\ 0 & 0 & 0 & 1 \end{bmatrix} \quad M_2 = \begin{bmatrix} R & T \\ 0 & 1 \end{bmatrix} \quad (2.4)$$

At this stage, the relationship between spatial point X and image point x can be written as:

$$x = K \cdot [R|T] \cdot X \quad (2.5)$$

Because of the homogeneous coordinate, each matrix function can give two independent functions. With two cameras, four independent functions can be acquired for three variables. If the epipolar relation can be satisfied strictly, these four functions can be reduced into three. In practice, the least square solution is used to estimate the spatial point of X .

2.2.2 Structured light

The checkerboard pattern was used as the structured light pattern; one sample pattern is shown in Figure 2.2. This pattern comprises alternating black and white blocks, having a strong contrast between adjacent segments. The intersection points, or cross-points, of the checkerboard exhibit a remarkable capacity for subpixel-accurate localisation. Moreover, the versatility of the checkerboard extends to its ability to correctly identify distorted variations (Ruffi et al., 2008; Ha, 2009). This distinctive attribute allows for the projection of the checkerboard pattern onto non-uniform, deformed surfaces while reliably detecting the

reference points of the checkerboard.

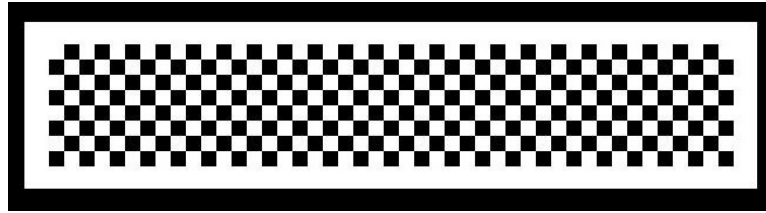


Figure 2.2: Checkerboard pattern projected on the wavy surface.

The adaptability of the checkerboard pattern is further evident in its variable density, a feature that affords control over the distribution of reference points. By adjusting the density of the checkerboard, users can tailor their approach to achieve differing point densities as required by the specific application.

An essential consideration in employing the checkerboard pattern is the configuration of its rows and columns. To prevent erroneous matching, it is advisable to maintain an arrangement in which one of the dimensions (either rows or columns) is odd while the other is even. This strategic choice mitigates the likelihood of spurious associations, contributing to the robustness and reliability of the structured light imaging process.

2.3 Experiment

2.3.1 Test facility

The Kelvin Hydrodynamics Tank (see Figure 2.3) serves as the primary towing test facility within the Kelvin Hydrodynamics Laboratory at the University of Strathclyde. It boasts dimensions of $76\text{m} \times 4.6\text{m} \times 2.5\text{m}$ and features a highly reliable four-flap type absorbing wave maker. This wave maker plays an important role in absorbing the reflected and radiated waves from the device, ensuring the consistency of the generated wave during a single test.

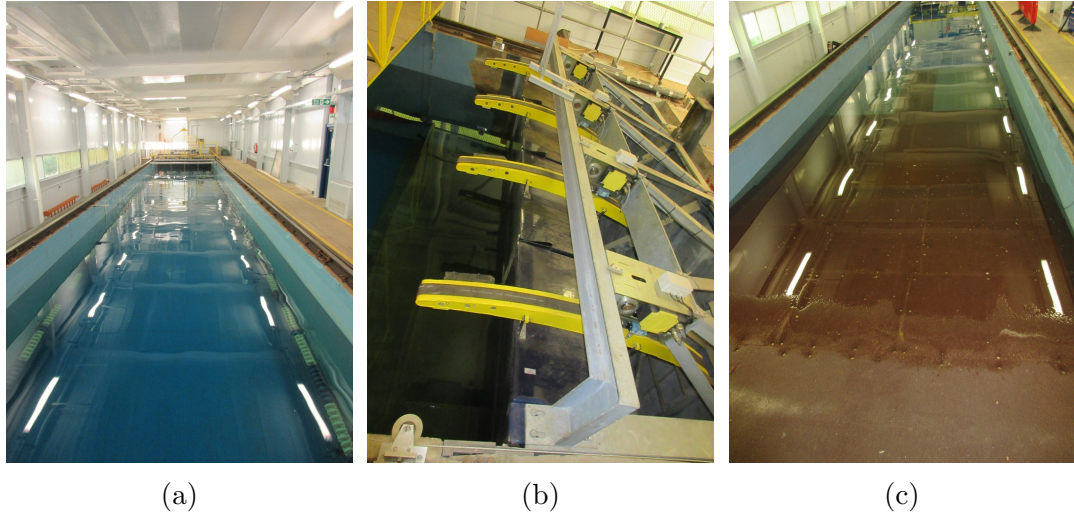


Figure 2.3: Kelvin Hydrodynamics Tank. (a) Tank; (b) Wave maker; (c) Beach.

To further enhance testing conditions, a high-quality variable slope beach has been installed at the end of the tank to absorb the waves and prevent reflection onto the testing objects, with a reflection coefficient typically below 5%. Additionally, the tank is equipped with a wall-mounted heater to minimise temperature variations.

A 3D compact wave tank housed on the ground floor of the Kelvin Hydrodynamics Laboratory at the University of Strathclyde (see Figure 2.4) was also used for the tests. This wave tank, boasting a total length of 9.267m and a width of 3.150m, maintained a fixed water depth of 1.0m. A portion of the tank, measuring 2.945m in length, was occupied by the wave maker and a wave-absorbing beach, leaving the test section of 6.322m in length. A highly reliable eight-flap type absorbing wave maker was deployed. This wave maker can absorb the reflected and radiated waves from the device, ensuring the consistency of the generated wave during a single test.

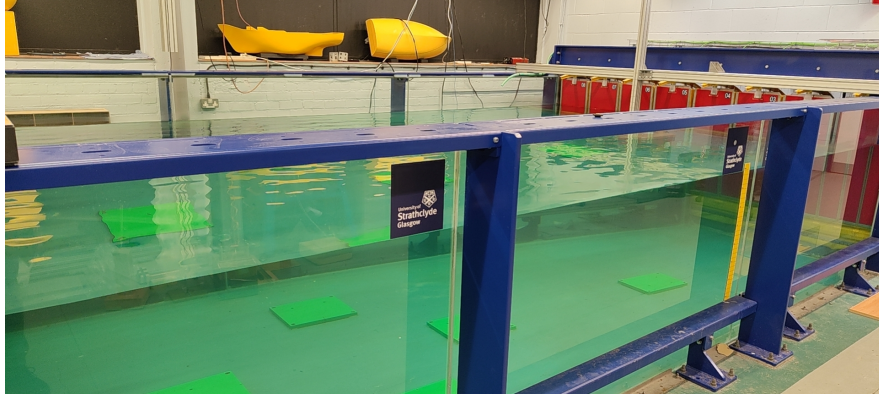


Figure 2.4: 3D Compact Wave Tank in Kelvin Hydrodynamics Laboratory

2.3.2 Experiment set up

The experimental setup, shown in Figure 2.5, comprises a designed measuring system. This system incorporates a pair of cameras equipped with global shutters, serving the role of stereo cameras, and a high-quality projector, which is instrumental in projecting image patterns with known encoding information onto the water surface. A crucial aspect in optimising the imaging process involves consideration of both the incident angle and the reflection angle of the light emitted from the projector. During the experimental phase, the cameras were configured to operate at their maximum capability, recording images at the rate of 60 frames per second (fps). Furthermore, the camera settings were finely tuned to capture images at a resolution of 4k, thereby facilitating the detailed scrutiny of the reflected patterns. Notably, the projector emerged as the exclusive source of illumination within the controlled experimental environment, a strategic choice aimed at enhancing the quality and accuracy of the imaging results from cameras.

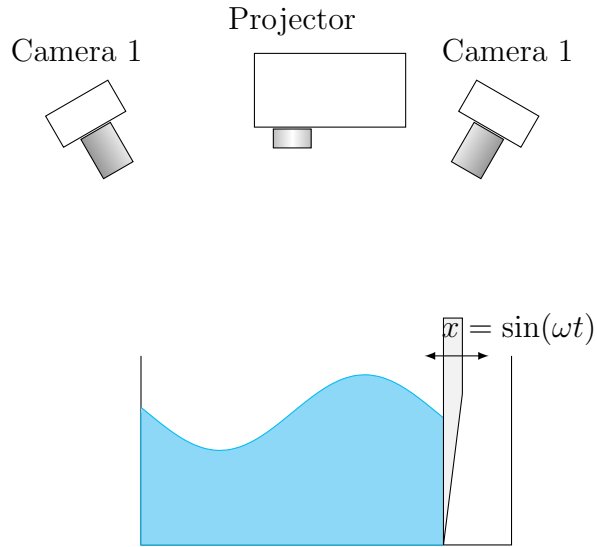


Figure 2.5: Experimental setup for wave measurement.

2.3.3 Calibration and synchronisation

The precise calibration of cameras is of paramount importance to ensure the attainment of accurate and dependable outcomes within the context of stereo-vision systems. This process necessitates the access of various parameters for each camera, including lens distortion, intrinsic parameters, and extrinsic parameters. The ultimate objective is to enable the cameras to capture three-dimensional spatial information accurately. In this study, the calibration method originally proposed by Zhang et al. (Zhang, 2000) was adopted. To facilitate this calibration, a standard checkerboard grid characterised by a 10mm grid size was employed. Fifteen distinct photographs of the checkerboard grid, captured from diverse positions and orientations, were utilised to calibrate each camera. It is important to underscore that one of the cameras served as a reference point, and its coordinates were defined as the primary coordinate for the stereo-vision system, as previously elucidated. This particular coordinate system could subsequently be transformed into the global coordinate system during subsequent data processing stages. The

Chapter 2. Methodology

calibration results will be discussed in detail within the context of each individual experiment, offering insight into the precision and accuracy achieved.

The synchronisation of cameras, within the context of this experimental setup, constitutes a critical procedural aspect. This synchronisation ensures that all cameras capture images at the same time. The significance of this synchronisation is particularly pronounced in applications wherein the cameras are deployed to record dynamic or moving subjects. In such scenarios, any temporal discrepancies between the captured images can introduce substantial inaccuracies in the final output.

In the proposed experimental framework, a master-slave configuration was adopted to accomplish this synchronisation. One camera was designated as the master camera, responsible for emitting a precise timing signal that governed the temporal coordination of other slave cameras. This coordination was imperative to measure alterations in the water surface. To evaluate the efficacy of this synchronisation procedure, a cluster of eight light-emitting diode (LED) lights, depicted in Figure 2.6, was employed as a pivotal component of this setup. These

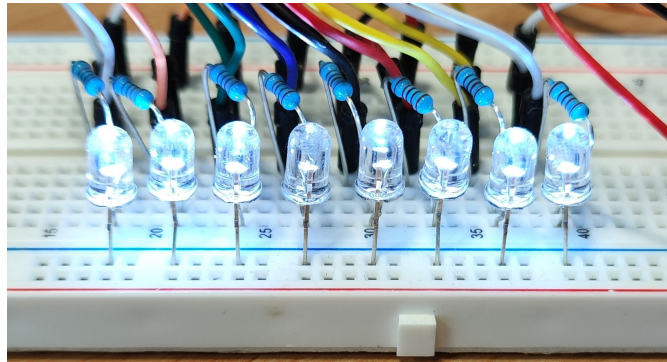


Figure 2.6: Binary clock. When the LED is on, it is 1, and when it is off, it is 0.

LED lights were lit via control signals transmitted from an Arduino Nano (a microcontroller). This arrangement facilitated the generation of binary signals accurate to within 1 millisecond. Each camera, in turn, captured video footage of

the LED array, and subsequently, the synchronisation accuracy was assessed by comparing the on/off states of the LED array across the individual video frames of each camera. Upon examination, it was ascertained that the maximum temporal deviation between the two cameras was a mere 2 milliseconds. Such a minimal discrepancy is unlikely to engender appreciable inaccuracies within the context of the stereo-vision system.

2.4 Validation experiment

2.4.1 Static validation experiment

The initial phase of validation for the proposed method involved a static experimental setup, intended to assess the performance of the system. This preliminary experiment employed a small PVC disc with a 50mm diameter upon which a checkerboard pattern was affixed, as shown in Figure 2.7. The disc was positioned at a fixed distance of 10cm from the cameras. The checkerboard itself was created in AutoCAD, with each checkerboard point maintaining a consistent separation of 4.00mm. A series of images were captured with the checkerboard pattern in its original position, and then the disc was rotated to vary the orientation of the pattern in relation to the cameras. This sequence of actions was repeated three times, resulting in different positional configurations of the checkerboard relative to the camera planes.

Subsequent to the acquisition of these image sets, the algorithm reconstructed the checkerboard points in the global coordinate system. Table 2.1 displays the average results of the computed distances between these points. The numerical labels 1~12 correspond to the serial identification of the individual checkerboard points. The row and column headings within the table indicate the pair of points utilised for distance calculations. The maximum measurement discrepancy ob-

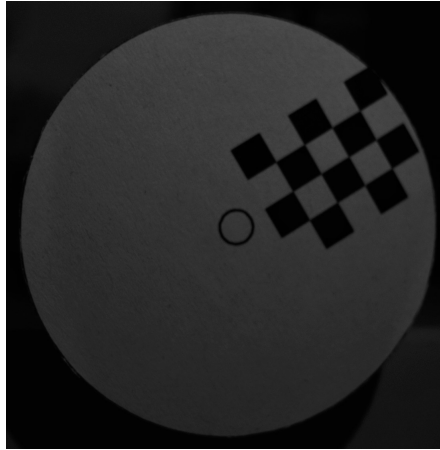


Figure 2.7: PVC disc with checkerboard

served during this validation experiment was a mere 0.06mm, and the maximum standard error estimate stood at 0.07mm. Based on the ITTC guideline, The 95% coverage was 0.21mm.

In a subsequent phase of static validation, the performance of the method was gauged concerning the camera-to-object distance. For this purpose, the small PVC disc was substituted with a larger standard cylinder, boasting a 100mm diameter and a height of 200mm. The camera was positioned 1m away from the central axis of the cylinder, as shown in Figure 2.8 (a). To facilitate the process, a checkerboard stripe was projected onto the surface of the cylinder. To ensure accurate measurements, a mask was generated by the program based on the prescribed mask width and the placement of two reference dots along the cylinder's central line. Prior to the corner detection of the checkerboard, the masked area was filled with black colour, while the checkerboard region within the test area was clearly defined and detected.

In this test scenario, obtaining the global coordinate information of each point on the cylinder presented a formidable challenge. Therefore, the diameter of the cylinder was employed as a proxy for error estimation. In an effort to validate the accuracy of the method, the diameter was measured using a calliper, yielding

Table 2.1: Average of distances between points

(mm)	1	2	3	4	5	6	7	8	9	10	11	12
1		3.99	8.02	4.03	5.72	8.99	8.01	8.99	11.35	11.99	12.67	14.44
2	3.99		3.99	5.69	4.03	5.68	8.95	8.02	8.95	12.63	11.99	12.64
3	8.02	3.99		8.96	5.66	4.04	11.31	8.94	8.01	14.39	12.63	11.99
4	4.03	5.69	8.96		4.03	8.01	3.98	5.68	8.96	7.96	8.94	11.31
5	5.72	4.03	5.66	4.03		3.99	5.65	3.99	5.64	8.90	7.96	8.91
6	8.99	5.68	4.04	8.01	3.99		8.93	5.63	3.97	11.26	8.89	7.96
7	8.01	8.95	11.31	3.98	5.65	8.93		4.02	8.01	3.98	5.68	8.95
8	8.99	8.02	8.94	5.68	3.99	5.63	4.02		3.99	5.63	3.98	5.63
9	11.35	8.95	8.01	8.96	5.64	3.97	8.01	3.99		8.92	5.63	3.99
10	11.99	12.63	14.39	7.96	8.90	11.26	3.98	5.63	8.92		4.02	7.99
11	12.67	11.99	12.63	8.94	7.96	8.89	5.68	3.98	5.63	4.02		3.97
12	14.44	12.64	11.99	11.31	8.91	7.96	8.95	5.63	3.99	7.99	3.97	

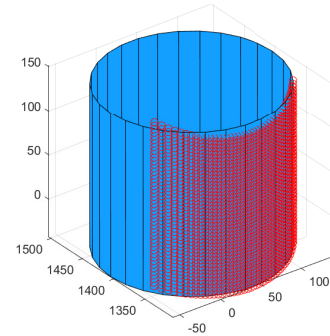
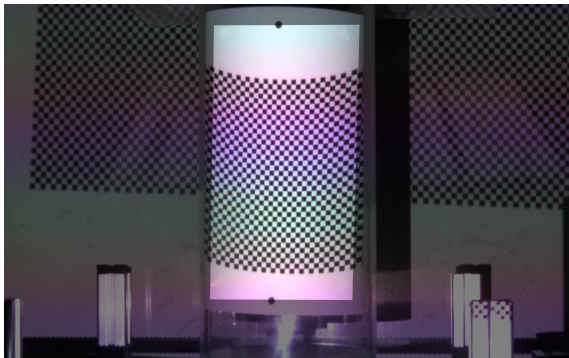


Figure 2.8: (a) Experimental setup of cylinder measurement. (b) The measured points (red dots) and the standard cylinder (blue cylinder).

a reading of 99.8mm.

The results of the measurements performed on the static cylinder are presented in Figure 2.8 (b), which indicates an estimated cylinder diameter of 99.6mm.

This measurement deviated by a marginal 0.2mm from the caliper-derived value, with a corresponding 95% coverage of 0.54mm. The comparative analysis of measurements conducted at various distances revealed a consistent trend: as the distance between the cameras and the object increased, the measurement error also exhibited a corresponding increase. Nevertheless, it is noteworthy that the proposed method consistently delivered impressive results in the context of static surface measurements.

2.4.2 Dynamic validation experiment

While the static result of the presented measurement method yields good outcomes, it is essential to acknowledge that the movement of objects can introduce certain challenges in this method. Therefore, the incorporation of a dynamic validation test becomes imperative. In the context of the experimental procedure described herein, the configuration remained consistent with the static cylinder test, with the only exception of imparting linear motion to the cylinder, thus endowing it with a sinusoidal velocity profile.

The outcomes of the measurement on the moving surface are visually represented in Figure 2.9. Evidently, the points acquired from the measurement conform well to the cylinder, as demonstrated in the projection plot. The average radius measures approximately 99.8mm, which aligns perfectly with the calliper-based measurement. It is noteworthy to emphasise that the variance between the measured points and the reference standard cylinder, as shown in Figure 2.9 (a), remains remarkably low, with the most substantial deviation within 500 frames being a mere 0.4mm. Furthermore, it is noteworthy that over 90% of the data points achieved an accuracy level of 0.2mm, underscoring the precision of this dynamic measurement approach.

The comprehensive assessment of dynamic performance within this measure-

Chapter 2. Methodology

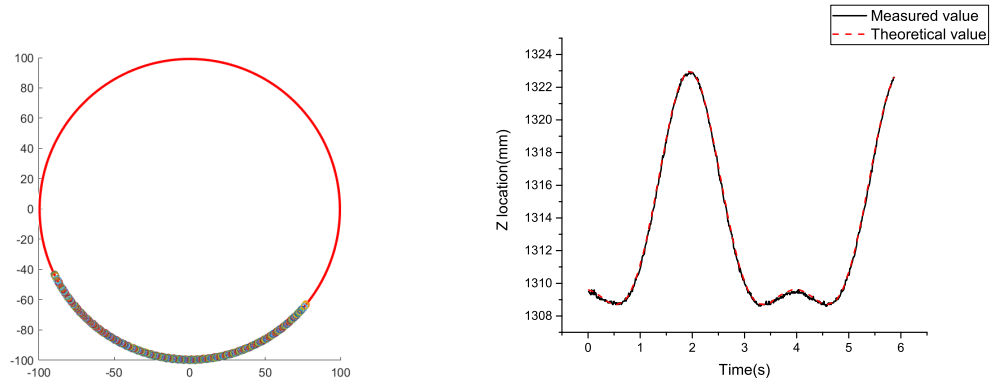


Figure 2.9: (a) The detected points projected on a horizontal plane. (b) Comparison of measurement and theoretical motion at a fixed point in xy plane.

ment method has yielded commendable results. Given that the motion of the cylinder adhered to a mathematical model represented as $X_0 = A \sin(\omega t + \psi)$, it is feasible to express the Z -coordinate of the surface of the cylinder as $Z = \sqrt{R^2 - (X - X_0)^2} + Z_0$ utilising fundamental geometry relationships. The wave frequency, denoted as ω , and the radius of the cylinder, represented as R , could be readily confirmed through the experimental setup. Additionally, the distance from the centerline, denoted as Z_0 , could be derived from the centerline distance of the cylinder within the measured data. However, certain parameters proved hard to determine directly, necessitating a fitting procedure based on the motion data acquired from a specific point. Figure 2.9 (b) illuminates the measurement results pertaining to the dynamic motion at a specific location. The outcomes of this experiment corroborate the theoretical predictions with exceptional fidelity, validating the reliability and precision of the dynamic measurement approach presented.

In the comparative context, the static result exhibits a higher degree of stability when compared with the outcomes of the dynamic cylinder measurement. This divergence in the dynamic measurements can be attributed to slight temporal disparities between the individual frames. Nevertheless, it is important

to note that, on the whole, the results pertaining to the cylinder shape exhibit remarkable similarity between the static and dynamic tests. Furthermore, the precision achieved in both scenarios consistently reaches the sub-millimetre level, further attesting to the efficacy of the measurement method under examination.

2.4.3 Sensitivity test

The sensitivity of the proposed method, when employed to measure water surface conditions, serves as an essential part of assessing its overall performance. In this evaluative study, the method was utilised to gauge the radiated waves generated by small spheres of varying sizes and masses. These spheres were released from a height of 150mm above a small water tank, with the camera situated at a distance of 1m from the water surface.

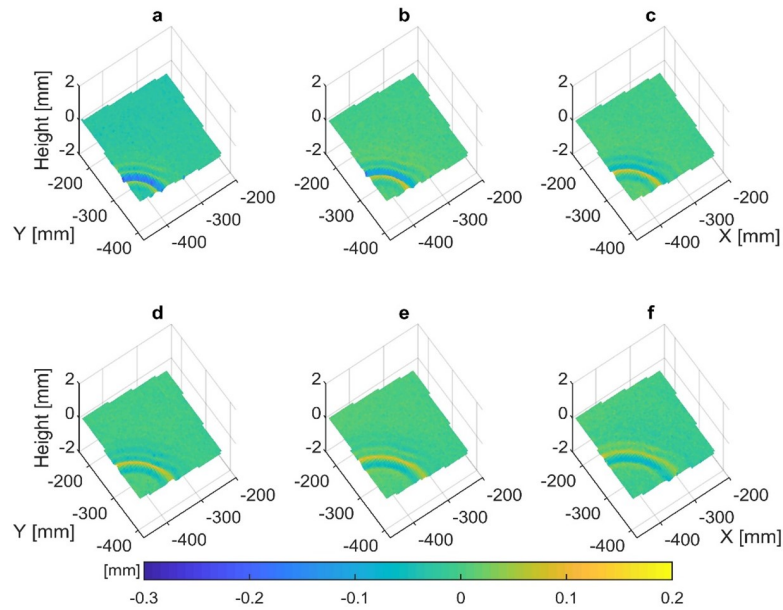


Figure 2.10: Radiated waves on the free surface.

Throughout the course of the experiment, the radiated waves exhibited minimal visibility to the human eye. Nevertheless, their presence and behaviour be-

came distinctly apparent when analysing the results as depicted in Figure 2.10 (a) to (f). A close examination revealed that the wave gradually propagates outward and continues to decay. Notably, the minimum wave amplitude recorded during this dynamic process was a mere 0.02 millimetres, originating from a sphere with a diameter of 4.10mm and a mass of 0.1 grams. This test unequivocally demonstrated the remarkable sensitivity of the method, which measured at a remarkable 0.0016%. This exceptional sensitivity endows the optical technique with multiple applications across various scenarios.

2.5 Measurement results

2.5.1 Regular wave

Following a series of validation and sensitivity tests, regular wave experiments were undertaken to assess the viability of the proposed method. The experimental setup was comprehensively detailed in Section 2.3.2. Positioned beneath the projector, a compact tank, boasting a length of 600mm and a width of 120mm, served as the test facility. The projector projected intricate image patterns directly onto the water surface, which was deliberately dyed with glass bubbles (3M K1, density: $0.125\text{g}/\text{cm}^2$). In this case, most light was diffused by the glass bubble instead of reflected by the water surface. The generation of waves was achieved by a screw equipped with a step motor, meticulously programmed to execute a sinusoidal motion. During the experimental phase, two distinct frequencies were deployed: 1Hz and 3Hz. The outcome of these wave tests was depicted in Figure 2.11 (a) and (b), illustrating the projected pattern and the captured frames on the water surface. The precision of grid detection was paramount; therefore, sub-pixel methods were employed to pinpoint the cross points of the checkerboard. This approach ensured accuracy, even without the need for high-resolution cameras or

projectors.

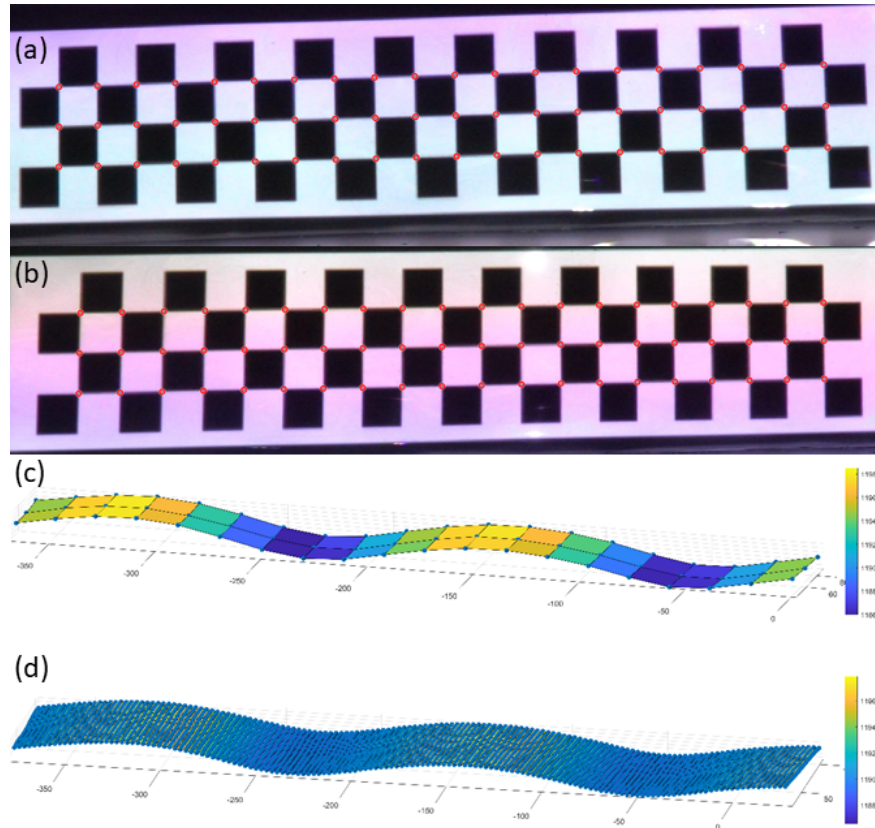


Figure 2.11: Regular wave measurement result. (a) Filmed image and recognised points in camera 1. (b) Filmed image and recognised points in camera 2. (c) Reconstructed wavy surface with low-density checkerboard. (d) Reconstructed wavy surface with high-density checkerboard.

To evaluate the reliability of the grid detection program at varying resolutions, the regular wave tests utilised checkerboard patterns of both low and high densities. For the low-density test, the mesh length between points approximated 20mm. In contrast, the high-density test featured a much finer mesh, with a mesh size of approximately 2.5mm—ideal for high-resolution wave reconstruction. Notably, each block on the high-density checkerboard consisted of a mere 16 pixels (4x4), and the captured pixel length for each block was a mere 10 pixels,

highlighting the contrast with the low-density scenario.

Figure 2.11 (c) and (d) illustrate the water wave reconstruction, with the frame exhibiting the highest wave height being the focal point. The height variance in these two results remained within the minuscule margin of 1mm. In practical terms, the low-density patterns offered the potential for real-time wave measurements, boasting a detection rate of twenty frames per second—provided sufficient computing power was available. However, it should be noted that high-density measurements, while invaluable for achieving high-resolution results, presented a trade-off in terms of computational demands. The detection rate for high-density measurements extended to a few minutes per frame, rendering it impractical for real-time monitoring with existing hardware capabilities. The significance of high-density measurements became evident when considering experiments where high-resolution outcomes took precedence over real-time monitoring, such as studies related to ship waves. This innovative method distinguished itself from conventional wave probes, which could only capture information at a single point. The results obtained from these measurements, as visually represented in Figure 2.11, elucidate that this approach not only permits the direct extraction of wave height and frequency but also facilitates the determination of other crucial parameters like wavelength, wave speed, and wave direction.

2.5.2 Irregular wave

The preceding section of this study demonstrated the prospective utility of the proposed method in the context of regular wave experiments. In this subsequent section, the study undertook a broader exploration, focusing on the evaluation of the viability and dependability of the method in the presence of irregular wave conditions. The experiment was conducted within a 500x500x400 mm wave tank without any wave-damping countermeasures. In this experimental setting,

Chapter 2. Methodology

a cylindrical body, subjected to heave motion, was strategically positioned at the corners of the tank to instigate wave generation. In order to ascertain the precision of the water surface measurements derived from the proposed method, an ultrasonic wave probe operating at a frequency of 100Hz was incorporated as a reference component within the experimental setup, which was visually depicted in Figure 2.12. Two cameras were placed approximately 1m away from the water surface, and a glass bubble layer was added to enhance reflectivity.

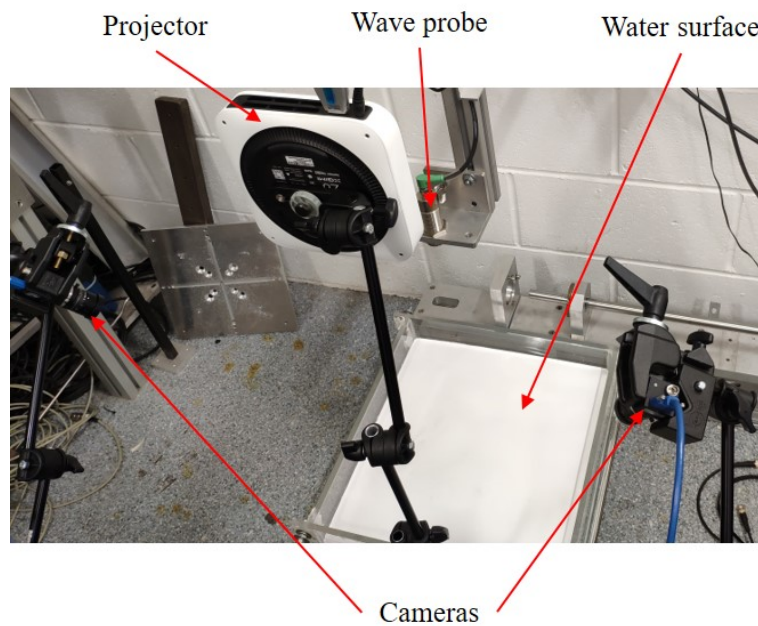


Figure 2.12: Irregular wave measurement result.

The result obtained from this experiment shows the progression of wave characteristics. Initially, upon the entry of the cylindrical body into the water, the waves appear in a radial pattern, as shown in Figure 2.13 (a). However, as time advanced, a complex interplay of multiple wave components originating from diverse sources commenced, leading to the emergence of an irregular wave pattern, as illustrated in Figure 2.13 (b)~(f).

A comparative analysis of the outcome achieved via the proposed method and

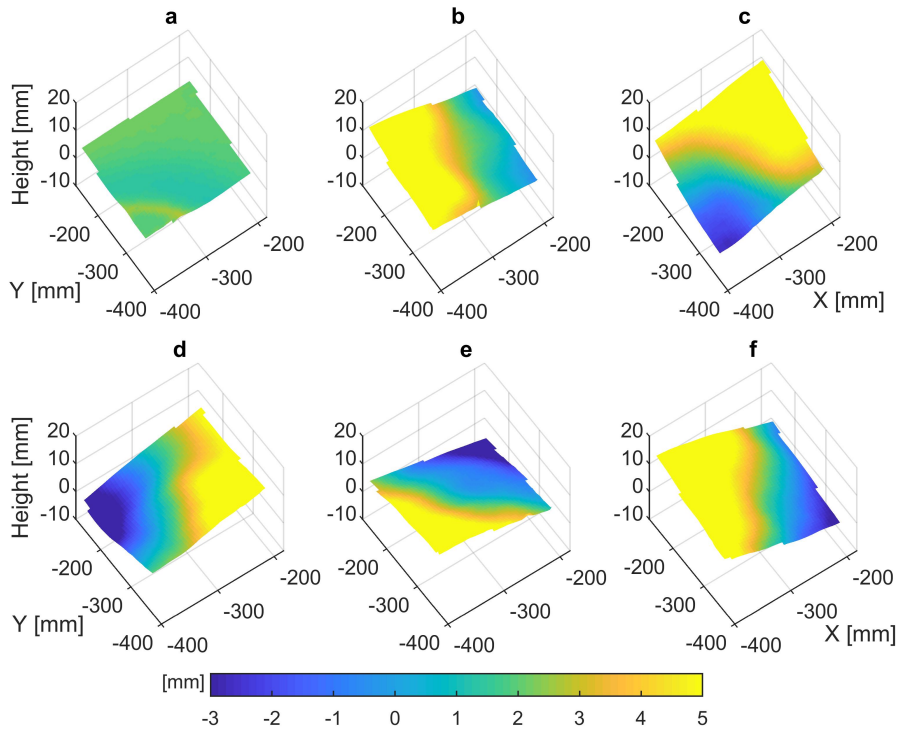


Figure 2.13: Irregular wave measurement result.

the one obtained through the ultrasonic wave probe was shown in Figure 2.14. The findings of this comparative analysis attest to a high level of overall concordance between the two measurement techniques. Nevertheless, it is important to acknowledge that the proposed method exhibits a relatively coarser temporal resolution in comparison to the ultrasonic wave probe. Consequently, it is worth noting that certain rapid changes occurring within the time frame of 8-10 seconds are not fully captured by the proposed method. It is pertinent to underscore that this limitation is not of paramount concern, as the temporal resolution constraints can be effectively mitigated by employing higher-grade cameras.

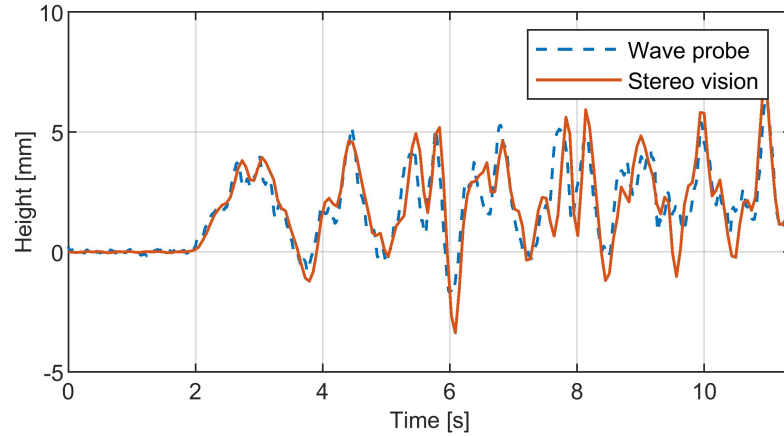


Figure 2.14: Comparison with ultrasonic wave probe.

2.6 Summary

This research study introduces a novel approach for contactless full-field measurement of water waves by implementing a stereo vision system in conjunction with structured light. The utilisation of a checkerboard box pattern facilitates sub-pixel point detection, enabling multiple point measurements by adjusting the checkerboard density. This adaptability allows for customisation of measurement speed or the number of data points, thereby tailoring the system to specific applications. Meanwhile, this method demonstrated sub-millimetre accuracy. The validation tests confirm the capability of the system to reconstruct dynamic water surfaces, exemplifying its effectiveness and accuracy.

Traditionally, researchers seeking to explore the intricate details of water surfaces often resort to wave probe arrays, which pose challenges, including potential interference between the probes. The approach presented here offers an innovative solution to these issues. By adopting this method, researchers can transcend the limitations of conventional wave probes and enhance the quality and reliability of their experiment results.

The ongoing efforts involve the application of this method to the wave tank at

Chapter 2. Methodology

the Kelvin Hydrodynamics Laboratory, where the aim is to eliminate the presence of floating particles. However, during these experiments, certain limitations were found. For example, the low reflectivity of the water surface hinders the visibility of the texture projected onto the water by the projector when observed by the cameras. These challenges were addressed to complete the wave behaviour reconstruction within the tank. Once resolved, this method promises to significantly enrich wave tank experiments, offering more detailed and dependable results, and thereby advancing the understanding of water wave dynamics.

Chapter 3

Comparative analysis of optical and traditional wave measurement techniques

3.1 Introduction

In hydrodynamics laboratories, the acquisition of wave data stands as an indispensable facet of research, influencing studies in ocean wave mechanics, naval architecture, and marine engineering. Currently, wave measurement techniques employed within hydrodynamics laboratories can be categorised into two distinct classes: surface-piercing and non-contact types.

The surface-piercing wave probes have a resistance type and a capacitance type. The resistance wave probe consists of two parallel rods. One end of it is connected to the data acquisition system (power supply and data acquisition are carried out at the same time). It is an open circuit situation when there is no contact with water because the two rods are not in contact with each other. When it is fixed vertically across the water surface, the circuit between the two rods

Chapter 3. Comparative analysis of optical and traditional wave measurement techniques

becomes a path due to the conductivity of the tank water. When the height of the water between the two rods changes, it causes a change in resistance. After the voltage change caused by the resistance change is read, it can be converted into the real-time height of the water surface through the corresponding relationship. The capacitance wave probe is similar to the resistance wave probe in that they both need to be fixed vertically through the water surface, and one end is connected to the data acquisition system. Finally, the corresponding relationship between voltage and water surface height is used to measure the data. However, it has only one taut insulated wire. The wire core has high conductivity, and the insulating layer is a dielectric material (Lawrence et al., 2012). The change in the height of the water around it will cause a change in its capacitance, which will cause a change in voltage. In addition to these two common surface-piercing wave probes, as technology advances, there is also a wave probe that utilises a motion capture system called Qualisys. The Qualisys system uses at least two cameras that simultaneously record the movement of specific markers to obtain coordinates in 3D space (Malý and Lopot, 2014). Therefore, placing these specific markers on a buoy that can only move vertically provides information on the water level at that position.

The non-contact measurements include the ultrasonic wave probe, pressure transducers and optical techniques. Ultrasonic wave probe is composed of a transmitter and a receiver or a transceiver that combines these two functions (Kelemen et al., 2015). Emitting ultrasonic waves that rebound from the water surface, the sensor computes water levels using the time-of-flight principle. Pressure transducers, instruments used to measure pressure, are deployed by researchers at the bottom of the water to pick up pressure changes due to changes in water surface height. The Transfer Function Method is generally used in the information conversion process. This method is based on the linear wave theory, and the pres-

Chapter 3. Comparative analysis of optical and traditional wave measurement techniques

sure information in a period of time is used to obtain the water surface height information by spectral analysis (Bishop and Donelan, 1987). Initially, it was unsuitable for shallow water due to the high nonlinearity in that condition. As more people study this, many improvements have been proposed for nonlinear component (Marino et al., 2022; Bonneton et al., 2018; Oliveras et al., 2012; Neumeier and Amos, 2006). Optical techniques encompass various approaches, such as particle-based techniques, water surface refraction methods, and image projection methodologies. These methodologies employ cameras to capture water surface motion under specific light sources, subsequently converting two-dimensional camera plane data into three-dimensional information within the world coordinate system using algorithmic processes. The particle-based method entails the dispersion of specialised particles on the water surface, stimulated by specific light sources, such as ultraviolet light (Fleming et al., 2018). These particles are then identified in camera images, with their movement in the world coordinate system utilised to deduce water surface height. In contrast, wave refraction methods generate underwater image patterns at predefined depths, employing two or more cameras to capture patterns refracted by the water surface. By analysing pattern displacements due to the deformation of the water surface (Moisy et al., 2009), the algorithm reconstructs the water surface to facilitate measurement. Lastly, the image projection method projects patterns onto the water surface, with changes in pattern shape corresponding to water surface movements. The shape of the water surface can be obtained by restoring the three-dimensional result of the pattern, thereby obtaining the required data. The three-dimensional representation of the pattern allows the acquisition of the requisite data. However, this technique relies on the reflectivity of the water surface, which is typically low, requiring the addition of dyes to enhance its reflectivity in the past (Tsubaki and Fujita, 2005; Cochard and Ancey, 2008).

An experiment was carried out in Kelvin Hydrodynamics Laboratory (KHL) with the proposed image projection method without any re-processing of water, a resistance wave probe (see Figure 3.1 (a)), and an ultrasonic wave probe (see Figure 3.1 (b)). This chapter addressed the merits and demerits of these methodologies, drawing upon the author’s expertise and insights.



Figure 3.1: Left: The resistance wave probe. Right: The ultrasonic wave probe.

3.2 Experiment setup

The experiment was performed in the 3D compact wave tank mentioned in Section 2.3.1.

During the experiment, two Z CAM E2 film cameras were deployed, boasting a resolution of 3840 pixels in the horizontal (H) dimension by 2160 pixels in the vertical (V) dimension, to record the dynamic behaviour of the free surface. These high-quality cameras were equipped with a maximum shooting frequency of 60 frames per second and were configured to capture imagery in 4k resolution. To project structured patterns onto the free surface, the capabilities of a DLP (Digital Light Processing) projector from Optoma were harnessed. It is important to note that, due to the presence of other equipment within the ex-

Chapter 3. Comparative analysis of optical and traditional wave measurement techniques

perimental setup, the image pattern was constrained to comprising a relatively modest 300 measurement points onto an area measuring 0.4m in length and 0.2m in width. To enhance the reflection of the image pattern from the water surface, the projector acts as the sole light source in response to the cleanliness of the tap water. Furthermore, the incident angle and reflection angle of the light in the experimental setup were considered, with the aim of optimising the visualisation of the reflected patterns on the water surface.

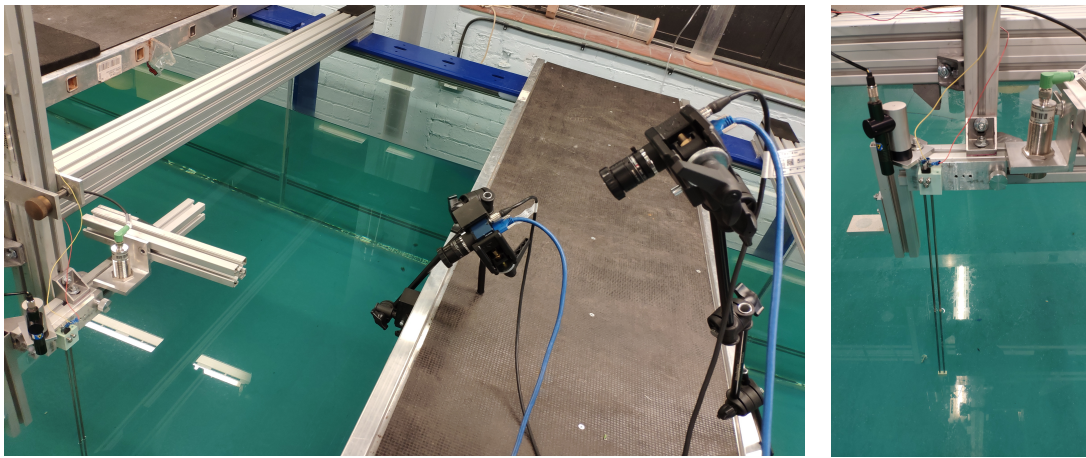


Figure 3.2: Experiment setup. Left: General setup. Right: wave probes.

In addition to the optical technique, a resistance wave probe and an ultrasonic wave probe were used (see Figure 3.2), both of which were connected to their respective amplifiers. The signal from the amplifiers was subsequently transmitted to the analogue-to-digital converter, where it was digitised and logged by a computer for further analysis. It is essential to underscore that the error associated with the wave profile in the direction perpendicular to the wave propagation was assumed to be negligible. All measurement devices were ensured to align in a co-linear fashion in this specific direction, as shown in Figure 3.3.

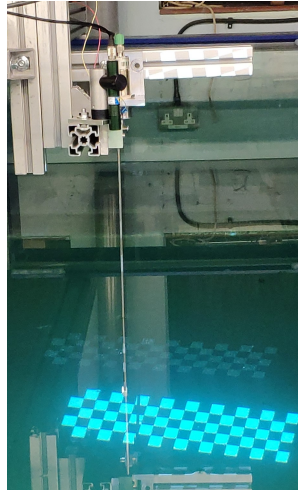


Figure 3.3: Measuring position.

3.2.1 Calibration

Before commencing the experiment, it is necessary to ensure the precise calibration of the instruments. In pursuit of this objective, a dedicated calibration plate was crafted within the laboratory setting. This plate, which serves a pivotal role in the calibration process, features two distinct rows of minuscule apertures, as shown in Figure 3.4. These rows of apertures are uniformly spaced at intervals of 2mm in the vertical dimension, and the separation between apertures in the same row is consistently 4mm.

To facilitate the calibration of the resistance wave probe, which involves the determination of voltage values in the absence of a pre-established calibration factor, a well-defined process was employed. Specifically, the probe was systematically moved downwards in eight discrete increments of 4mm, and subsequently, it was returned to its initial position in a comparable manner. This calibration process estimated the calibration factor for the relationship between water height and voltage, based on the measurements obtained. A 95% coverage was ascertained following the guidelines from ITTC, yielding a value of 0.302mm.

The time-of-flight principle, utilised in ultrasonic wave probes, necessitates

Chapter 3. Comparative analysis of optical and traditional wave measurement techniques

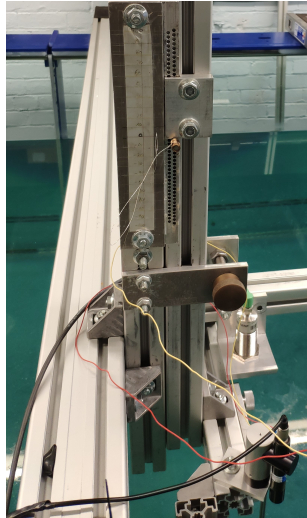


Figure 3.4: Calibration plate and set up.

solely the knowledge of the speed of ultrasonic waves for calibration. In this context, the calibration setup, as shown in Figure 3.5, was uncomplicated. It entailed the fix of the distance separating the transceiver from the object, thereby affording the calibration factor, which is the speed of ultrasonic waves. During the experimental phase, this calibration setup was interfaced with the Ref port of the ultrasonic wave probe controller.



Figure 3.5: Ultrasonic wave probe calibration

As delineated in Section 2.3.3, the calibration of the cameras was executed utilising Zhang's method (Zhang, 2000). Each of the two cameras was tasked with capturing a series of 10-20 photographs of a checkerboard pattern, charac-

Chapter 3. Comparative analysis of optical and traditional wave measurement techniques

terised by dimensions measuring 30x30mm, positioned at varying locations and orientations. Subsequent to the analysis of the image data, the camera parameters were deduced, enabling the computation of the spatial coordinates of the real-world points. Notably, a discrepancy of 0.15 pixels was observed following the calibration process.

3.2.2 Validation

Following the calibration procedures, to gauge the precision and reliability of these methods, a validation experiment was executed. In this experiment, a checkerboard plate was securely affixed to the resistant wave probe and ultrasonic wave probe system, which was then systematically displaced in a controlled manner by moving vertically eight times, each increment spaced 4mm apart.

The outcome of this validation exercise is presented in Table 3.1. Notably, a negative sign characterises the results obtained from the ultrasonic wave probe calibration. This is a consequence of the inherent ability of the method to measure the diminishing distance between the object and the receiver as the system descends vertically. A similar characteristic was observed in the results from the optical technique. However, in contrast, the optical technique, during the validation experiment, does not exhibit a negative sign in its outcomes. This divergence arises from the fact that, during the post-processing of the image, the negative sign has already been applied.

Upon close scrutiny, it becomes evident that the maximum error recorded in the validation experiment was 0.419mm for the ultrasonic wave probe, 0.185mm for the resistance wave probe, and 0.322mm for the optical technique. Additionally, in compliance with ITTC regulations, a 95% uncertainty band was established for these three calibration methods. The uncertainty band for the ultrasonic wave probe was $\pm 0.571\text{mm}$, while the resistance wave probe exhibited an

Table 3.1: Different wave measurement techniques Validation

Real distance (mm)	Ultrasonic wave probe (mm)	Resistance wave probe (mm)	Optical technique (mm)
4.000	-4.419	4.048	4.236
8.000	-7.651	8.100	8.100
12.000	-11.822	11.889	11.843
16.000	-16.206	16.182	16.144
20.000	-19.922	20.030	20.096
24.000	-23.809	23.978	24.031
28.000	-28.331	28.185	28.322

uncertainty band of $\pm 0.205\text{mm}$, and the optical technique was $\pm 0.490\text{mm}$. It is noteworthy that all measurement residuals fell within these specified uncertainty bounds, underscoring the reliability of the calibration results and thus affirming their suitability for employment in subsequent experimental endeavours.

3.2.3 Test plan

During the experimental phase, an analysis was conducted to study the influence of both wave frequency and wave height on the obtained measurement outcomes. For a comprehensive overview of the experimental design, the specifics are outlined in Table 3.2. Initially, the wave amplitude remained constant while the wave frequency was systematically varied from 0.4Hz to 1.0Hz, with incremental intervals of 0.1Hz. This particular phase of the experiment was primarily focused on investigating the impact of wave frequency. Concurrently, the investigation into the implications of wave height entailed the utilisation of three pre-set frequencies: a low frequency of 0.4Hz, a medium frequency of 0.7Hz, and a high frequency of 1.0Hz.

This test plan enabled an evaluation of the interplay between wave height and the chosen frequencies. These devised experimental sets were structured to

Table 3.2: Test matrix.

Test ID	Wave frequency (Hz)	Wave amplitude (mm)
01	0.4	5
02	0.5	5
03	0.6	5
04	0.7	5
05	0.8	5
06	0.9	5
07	1.0	5
08	0.4	10
09	0.4	15
10	0.4	20
11	0.7	10
12	0.7	15
13	0.7	20
14	1.0	10
15	1.0	15
16	1.0	20

facilitate a comprehensive analysis of the performance of all three measurement methods in relation to amplitude, frequency, and wave steepness (Zhang et al., 2021).

3.3 Results

3.3.1 Spatial information

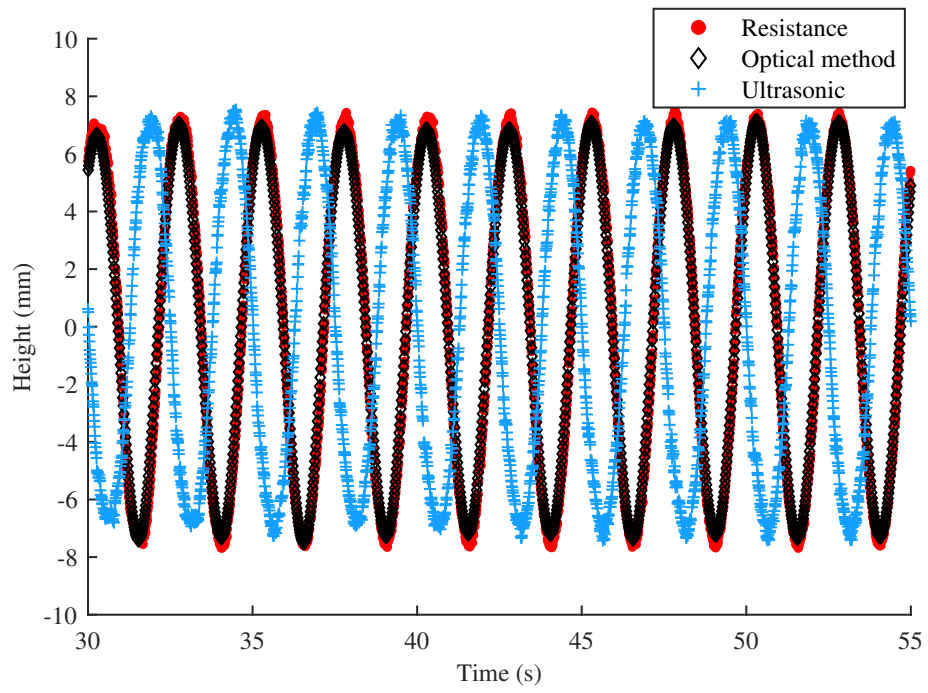
Due to inherent constraints in the available equipment, it was impractical to establish a direct connection between the Z CAM and the data acquisition systems responsible for monitoring the resistance wave probe and the ultrasonic wave probe. Consequently, the cameras lacked the capability to directly receive the commencement signal emitted by the wave maker. This technical limitation precluded the synchronisation of data acquisition between the optical technology

Chapter 3. Comparative analysis of optical and traditional wave measurement techniques

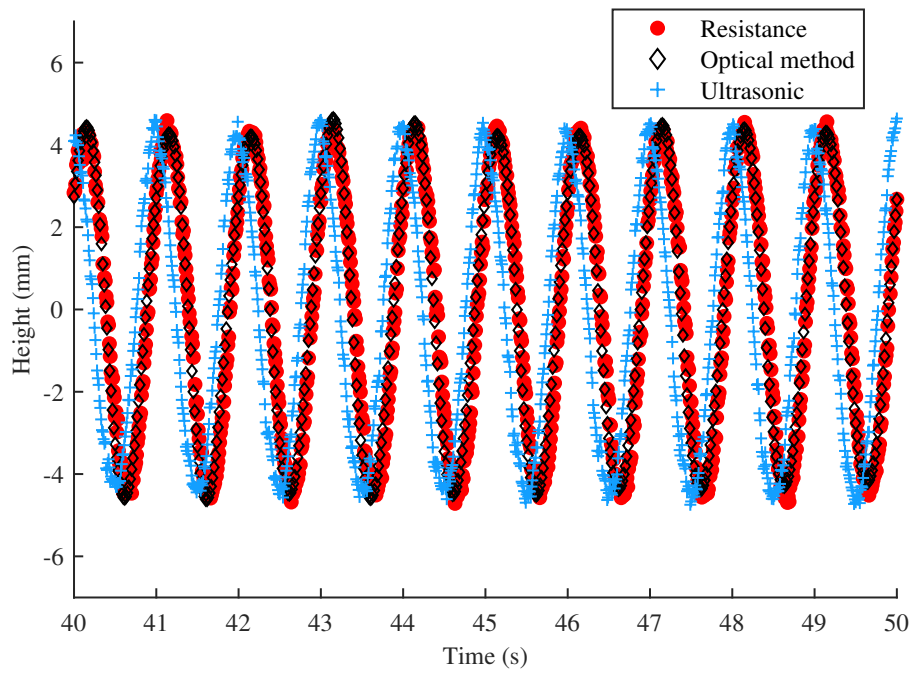
and the wave probes during the experimental phase. Moreover, an evident phase disparity was noted in the results of the ultrasonic wave probe in comparison to those derived from the resistance wave probe. The ultrasonic wave probe exhibited a discernible lag, which stemmed from the necessity to await the return of the emitted ultrasonic wave to the receiver. To overcome this issue and facilitate a more cohesive comparison of results, manual adjustments were carefully executed to ensure the synchronisation of outcomes between the optical technology and the resistance wave probe. This strategic intervention was deemed necessary, particularly in light of the accurate time information of the resistance wave probe.

Subsequently, a comparison of results obtained through these distinct measurement techniques revealed a remarkable degree of concordance, as shown in Figure 3.6. Under conditions characterised by low wave amplitudes, the maximum observed error was a mere 0.384mm. This margin of error, falling well within the ambit of the 95% confidence intervals for those methods, which were established at $\pm 0.571\text{mm}$, $\pm 0.205\text{mm}$, and $\pm 0.490\text{mm}$, respectively, was deemed to be within the range of reasonable tolerance. Conversely, in scenarios involving high wave amplitudes, the maximum error becomes more pronounced, particularly in the comparison between the ultrasonic wave probe and the optical technique, where it reaches 0.91mm. Nevertheless, this error remains lower than the cumulative upper limit of the two 95% confidence intervals, which amounted to 1.061mm. It is noteworthy that this system-induced error, as influenced by the quality of calibration and inherent camera characteristics, exhibited consistency within a defined range. Importantly, this system error did not exhibit an upward trend in response to the increased wave height.

Chapter 3. Comparative analysis of optical and traditional wave measurement techniques



(a)



(b)

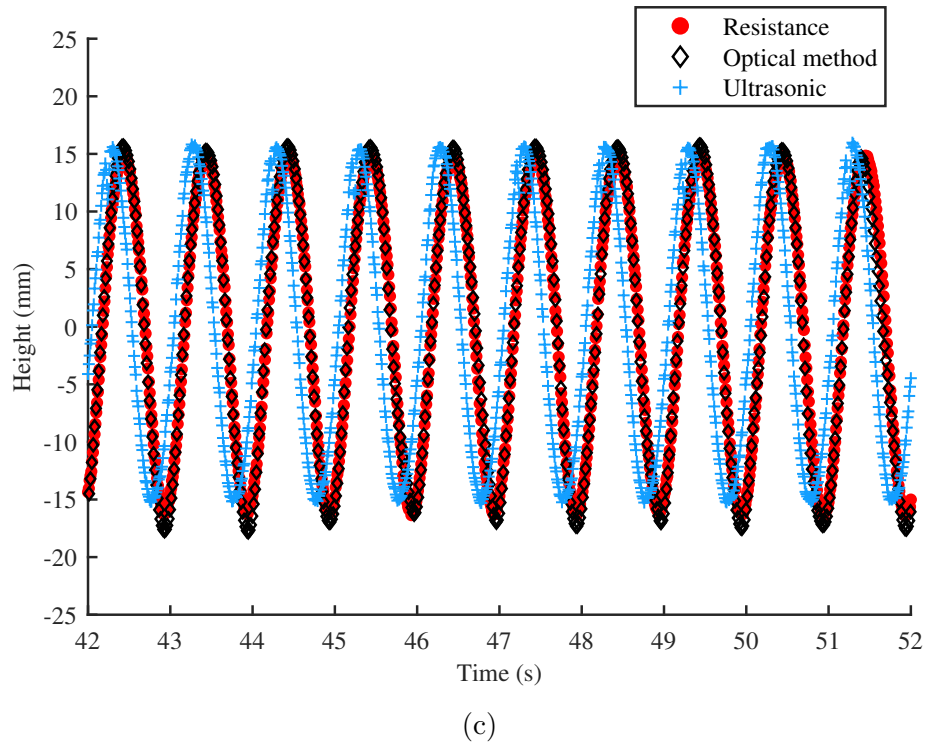


Figure 3.6: (a) Test 01; (b) Test 07; (c) Test 16.

Furthermore, while the outcomes yielded by the resistance wave probe are slightly lower, attributed to the meniscus-shaped interface formed by surface tension between the two rods constituting the probe, these variances were adjudged to be non-significant in the context of the presented experimental conditions. Meanwhile, the optical technique also possesses the capacity to furnish spatial information, as shown in Figure 3.7. This spatial information constitutes an additional dimension that a single wave probe is incapable of delivering, including details about wave direction. By modulating the resolution and size of the projection image pattern, one can easily tailor the quantity and spatial coverage of data points acquired in the physical domain.

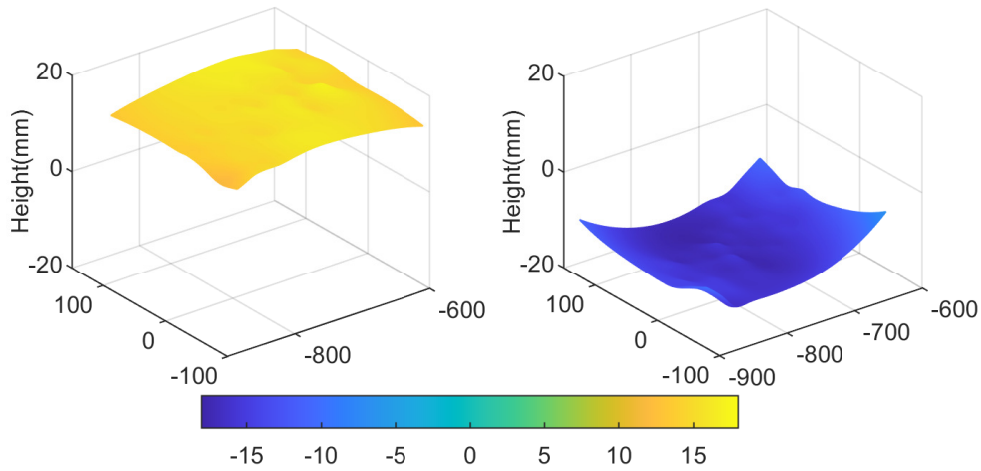


Figure 3.7: Wavefield measurement results of the optical technique. Left: crest; Right: trough.

3.3.2 Time information

The resistance wave probe was endowed with the flexibility to modulate its sampling frequency, allowing for adjustments of up to 20MHz within the acquisition software. This feature empowers the instrument to capture intricate wave information across the entire spectrum of wave frequencies. In stark contrast, the sampling speed of the ultrasonic wave probe was constrained by the time it takes for the ultrasonic wave to travel, consequently establishing an upper boundary of 100Hz for this specific experimental setup. Meanwhile, the sampling speed of the optical technique was contingent upon the capabilities of the cameras and the transmission of data. Notably, in the course of this experiment, the Z CAM camera was utilised, delivering a video frame rate of 60 frames per second (fps), thereby dictating the sampling frequency of the optical technique. It is noteworthy that the attainment of higher sampling frequencies is feasible with the utilisation of more advanced equipment, such as high-speed cameras capable of frame rates reaching into the thousands or even tens of thousands.

Furthermore, it is imperative to underscore the impact of sampling frequency

on the results, as shown in Figure 3.6. The data collected during Test 07, conducted at a higher frequency, exhibits a sparser distribution of data points, even though the amplitude recorded in Test 01 surpasses that of Test 07 by nearly 2mm. This observation was similarly replicated in Test 16 and Test 07, both executed at identical frequencies, where increased amplitudes lead to a reduced data point density. It is noteworthy that the point density at the wave crest and trough exhibits no significant disparity, a phenomenon that can be ascribed to the rate of change in the wave. The derivative of the wave height near the crest and trough has smaller values, signifying a slower rate of change, while the derivative between the crest and trough has larger values, indicating a more rapid rate of change, which, in turn, results in the sparsity of data.

Although the 60Hz sampling frequency might initially give the impression of discontinuity in the results, it is able to effectively capture critical wave peaks and troughs with a high level of detail at the wave amplitude of 15mm and wave frequency of 1Hz (refer to Figure 3.8). Consequently, it is reasonable to infer that a sampling frequency of 60Hz was adequate for the analysis of regular waves. However, it is necessary to consider the adoption of higher sampling frequencies in forthcoming experiments, especially when analysing irregular waves. This measure would ensure the capture of finer details and a more seamless continuity of data.

3.4 Discussions

Based on the experiments conducted in this study, as well as insights gleaned from the literature, this section will provide a comparative analysis of these wave measurement methods: the resistance wave probe, the ultrasonic wave probe, and optical technology. This discussion aims to present a thorough evaluation of the advantages and disadvantages associated with each method, thereby serving as

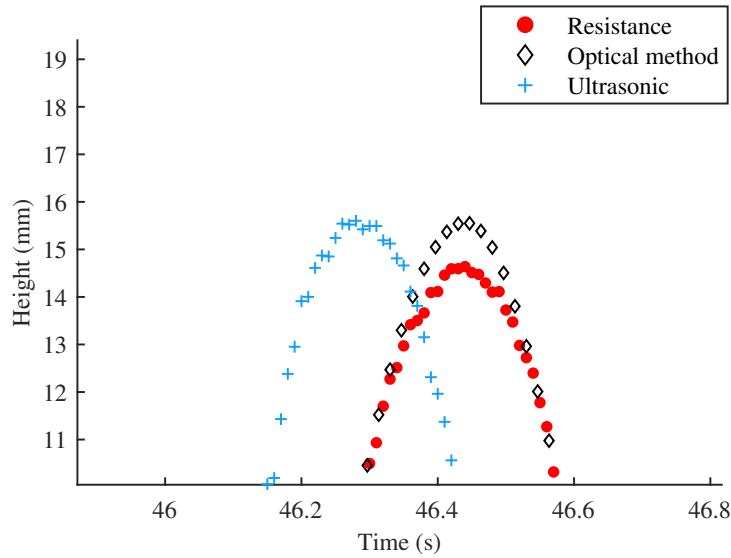


Figure 3.8: Close-up examination of one peak in the measurement results of Test 16.

a valuable point of reference for future experimental designs when selecting an appropriate wave measurement technique.

3.4.1 Resistance wave probe

Nowadays, the resistance wave probe stands as the most prevalent and widely utilised technique in hydrodynamic laboratories. Comprising two parallel metallic conductors, these can take the form of rods or metal wires, with the sole prerequisite being the stable maintenance of their structural integrity throughout the experiment. The necessity for this stability stems from the susceptibility of even minor alterations to affect the precision of experimental results. However, this requirement is readily achievable, minimising concerns in this respect. The resistance wave probe is characterised by its cost-effectiveness, straightforward assembly, and a notable lack of constraints, rendering it compatible with a wide array of signal acquisition systems. Furthermore, it offers a high degree of accuracy and flexibility in adjusting the sampling frequency.

Nonetheless, it is essential to highlight certain shortcomings associated with the resistance wave probe. Primarily, this method relies on the linear relationship between voltage and the length of the metallic conductor for data acquisition. However, this linearity is compromised within the 15% range at both ends of the conductor, limiting the effective data collection to the central 70% of the conductor. Additionally, the penetration of the metal conductor through the water surface generates radiation and diffraction wave fields, introducing systematic errors in the data. As mentioned earlier, the meniscus-shaped water surface created by surface tension similarly exhibits a marginal influence. Lastly, spatial requirements pertaining to the length and stiffness of the metallic conductor pose installation challenges, restricting its application in compact spaces.

3.4.2 Ultrasonic wave probe

In comparison to the resistance wave probe, the ultrasonic wave probe is less commonly employed. Notably, it boasts a compact form factor and does not come into direct contact with the water surface, alleviating concerns related to water surface distribution and spatial constraints. Calculating the distance from the water surface based on the time-of-flight principle, this method obviates the need for time-consuming calibration processes. Instead, a reference device for computing the flight speed of ultrasonic waves must be integrated into the acquisition system. Nevertheless, inherent limitations accompany the use of ultrasonic wave probes. Firstly, this method introduces a phase difference between the collected data and actual wave information due to its reliance on flight time. Additionally, it imposes a maximum limit on the achievable sampling frequency. Furthermore, maintaining a suitable distance from the water surface is imperative to facilitate effective ultrasonic wave reflection. Due to the limitation of flight time, the ultrasonic wave probe cannot be too close to the water surface. As emission in a

diffused manner results in average measurements across a small area, excessive distance may impede the reception of reflected waves, rendering data acquisition unfeasible. Finally, the stability of this method may be compromised on rare occasions, as environmental factors can cause fluctuations in the flight speed of ultrasonic waves, resulting in anomalous experimental data.

3.4.3 Optical technology

In recent years, optical technology has gained significant attention as an emerging wave measurement methodology. The rapid advancement of technology, marked by the proliferation of high-performance computers and cameras, has rendered optical technology promising. Presently, several principles underlie this technology, with our focus herein centring on the specific optical technology employed in this study. This method relies on camera-captured projections of pattern deformations on the water surface, necessitating relatively modest spatial requirements compared to ultrasound wave probes. Furthermore, optical technology offers adaptability to various measurement requirements through adjustments in image pattern size, position, and characteristic point density, obviating the need for additional calibration processes or equipment. This not only saves preparation time but also enhances the acquisition of valuable data within the same experimental time frame.

However, the advantages of optical technology are balanced by a set of concerns. Foremost, it may impose a significant financial burden on experiments, as the deployment of two or more high-pixel and high-frame-rate cameras, along with potentially costly camera lenses, incurs substantial costs. For instance, the Z CAM cameras and lens combination utilised in this study amounted to approximately £5,000, while high-speed cameras capable of achieving even higher frame rates demanded expenditures exceeding £10,000. Reflectivity issues asso-

Chapter 3. Comparative analysis of optical and traditional wave measurement techniques

ciated with the water surface present inevitable uncertainties, as relying solely on naturally occurring dust may result in incomplete coverage. To circumvent this problem, some methodologies introduce particles into the water, thereby raising safety and cleanliness issues. In instances characterised by steep waves, optical technology may encounter limitations, as reflected light may not be captured by cameras, leading to incomplete wave information. Finally, achieving high-frequency real-time measurements with increasingly higher spatial resolutions presents a formidable challenge, with no effective solutions currently available.

3.5 Summary

Section 3.4 provides an in-depth examination of the merits and demerits associated with various techniques employed in the measurement of waves. This analysis facilitates an exploration into the applicability of each category of wave measurement probe in distinct scenarios.

In the temporal dimension, resistance wave probes exhibit superior resolution characteristics. Notably, their influence on the water surface can be disregarded beyond a certain threshold of wave height, rendering them well-suited for a wide range of situations. They are particularly suitable for scenarios providing reference values of waves at a certain distance in front of the device or providing wave data for regions that are not in close proximity to the device. In contrast, ultrasonic probes, with their distinctive capability to measure the value over a confined spatial area, find their niche in applications characterised by expansive experimental dimensions and gradual spatial changes in the water surface. Furthermore, their compatibility with small waves is advantageous, as they exert no impact on the water surface. A notable application of ultrasonic probes is to measure the height of the water column within an oscillating water column (OWC) device. This is primarily due to the generally presumed flat and relatively stable

Chapter 3. Comparative analysis of optical and traditional wave measurement techniques

nature of the water column within an OWC, affording an ultrasound wave probe the capacity to furnish high-precision water surface height information.

Optical techniques, conversely, offer high spatial resolution, and their temporal resolution can be enhanced through the utilisation of advanced camera systems. However, their practicality hinges on a high degree of camera capture, thus rendering them particularly well-suited for the measurement of fine wave fields that neither compromise the integrity of the captured feature points by the camera nor induce issues related to wave steepness. Indeed, optical techniques excel in the examination of wave fields generated by the uniform motion of small underwater models, representing a niche of application where their capabilities truly shine.

Chapter 4

Water surface inside Oscillating Water Column

4.1 Introduction

In recent years, the increasingly severe problem of environmental pollution has prompted significant research efforts worldwide to address environmental management issues. Traditional energy sources such as coal and oil have met the energy demands of daily life, but the greenhouse gases generated during combustion are a significant obstacle to environmental management. As a result, environmentally sustainable new energy sources have gradually entered the vision of the public, such as wind and solar energy, which are now relatively common. In the field of ocean engineering, new energy sources such as wave energy and tidal energy have also been proposed.

The Oscillating Water Column (OWC) is a distinct Wave Energy Converter (WEC) device that harnesses the natural blow holes found in limestone cliffs (Heath, 2012). It consists of two primary components: an air chamber and a power take-off (PTO) system. When waves interact with the OWC device, the air

inside the chamber undergoes compression and is subsequently directed through the PTO system, leading to the generation of power. One notable characteristic of OWC devices is their ability to maintain a high level of energy conversion efficiency even when the main structure is stationary. This feature makes them well-suited for integration with other renewable energy technologies like wind turbines (Bayoumi, 2013), as the relative motion between the devices reduces the risk of collisions during severe weather conditions. Furthermore, OWC devices can share infrastructure components such as electrical cables, power transfer equipment, and mooring systems, offering potential cost reductions. Due to their robustness, OWC devices have been widely recognised and favoured as a prominent choice among WECs since the early stages of wave energy technology.

The experimental design of OWC devices can be categorised into 2D and 3D approaches. In 2D experiments, the OWC device is represented by two adjacent vertical parallel plates, which serve as a simplified representation of the actual device (Sarmento, 1992). On the other hand, in 3D experiments, the dimensions of the real-world OWC device are scaled down to model dimensions based on a certain scale factor (Gouaud et al., 2010). Historically, early research on OWC devices was primarily based on linear surface-wave theory. This approach aimed to calculate the energy conversion efficiency of OWC devices by considering the motion of the water column as analogous to a rigid piston (EVANS, 1978). However, this simplistic model failed to accurately capture the spatial variations in the internal water level of the OWC. As a result, an alternative method was developed. The pressure inside the OWC device was measured to describe the energy conversion process more accurately (Evans, 1982). Comparative studies have shown that both the rigid piston model and pressure-based methods yield similar results in terms of the maximum energy extraction efficiency (Sarmento and Falcão, 1985). Consequently, in most experimental designs conducted thus

far, a single wave probe is typically positioned at the central location within the OWC device to measure the liquid level of the internal water column. In a few experiments, three wave probes were deployed inside the OWC (Ning et al., 2016). Apart from the centrally positioned probe, the other two probes were placed near the walls, one in the front and one in the rear. This arrangement ensured that the liquid surface of the water column moved like a rigid piston. However, due to the limited data points provided by this measurement method, its persuasiveness is compromised. Such limitations highlight the current constraints of measurement techniques in accurately assessing the dynamic behaviour of OWC devices.

In order to overcome these limitations and gain a more comprehensive understanding of the spatial distribution of the surface of the internal water column, this study employs the innovative optical wave measurement method mentioned in Chapter 2. This emerging technique offers improved capabilities for tracking and analysing the complex behaviour of the internal water column within the OWC device.

A Fixed Symmetry Cylindrical OWC (FSCOWC) device was selected as the test setup to conduct the experimental investigation. The experiments were performed in the large towing tank at the Kelvin Laboratory, providing a controlled and realistic environment for studying the performance and characteristics of the OWC device. By employing advanced measurement techniques and conducting comprehensive experiments on the device, this study aims to contribute valuable insights into the spatial dynamics and energy conversion efficiency of OWC devices. The findings obtained from this research endeavour will not only enhance our fundamental understanding of OWC technology but also inform the design and optimisation of future OWC devices for wave energy conversion.

4.2 Experiment

4.2.1 Test facility

The experiment was performed in the Kelvin Hydrodynamics Tank mentioned in Section 2.3.1.

4.2.2 Model

For this experiment, the OWC chamber utilised in the experiment was constructed from acrylic material. To ensure a smooth entrance and prevent vortexes that could result in energy loss, a filleted plastic ring was installed at the end of the chamber (Zhang et al., 2012). The model was positioned at the centre of the tank using a wooden frame, situated 34m away from the wave maker. The geometric details of the design and the corresponding measurements can be found in Figure 4.1 and Table 4.1, respectively. These dimensions also dictated that

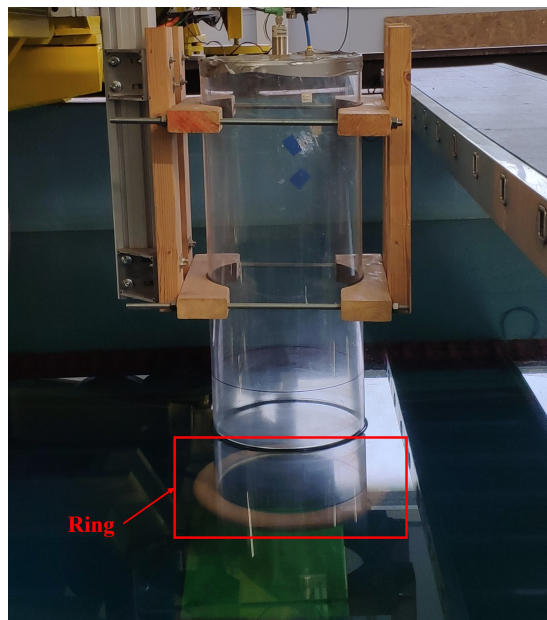


Figure 4.1: OWC model used in the test.

Table 4.1: Geometry details of the OWC

Component	Parameters	Value (mm)
OWC model	Total length	1045.0 ± 0.5
	Draft	350.0 ± 5.0
	Outer Diameter	299.0 ± 0.5
	Inner Diameter	287.0 ± 0.5
Ring	Thickness	45.3 ± 0.2
	Fillet radius	22.0 ± 0.2
	Outer Diameter	390.0 ± 0.5
	Inner Diameter	299.3 ± 0.5

the experiment must be conducted in the large towing tank of the Kelvin Hydrodynamics Laboratory, which is 74m long and 4.15m wide. The water depth can be varied, and it was precisely set at 2.10 ± 0.01 m in this test.

It is important to note that the draft measurements exhibit a relatively large relative uncertainty of 2.86%. This uncertainty arises due to challenges in aligning the OWC with the intended water line inside the chamber, primarily caused by the thickness of the draft line (2.0 ± 0.1 mm) and the meniscus effect. Additionally, alignment was conducted at the same level as the top of the device, introducing visual effects such as the refraction effect of the transparent acrylic tube. The impact of the draft uncertainty on the results will be further discussed in subsequent sections.

4.2.3 Set up

The experimental configuration, as depicted in Figure 4.2, involved the utilisation of two small global shutter industrial cameras positioned on an extrusion located above the OWC. These cameras were strategically placed on the same side of the device to capture optimal reflected light. Conversely, the projector was mounted on the same extrusion but positioned on the opposite side of the device relative to the cameras. This arrangement ensured that the image planes of cameras

Chapter 4. Water surface inside Oscillating Water Column

received the maximum amount of reflected light, leading to more reliable and precise results. Given the limited space within the OWC and the controllable up and down movement of the water column inside it, glass bubbles were dispersed on the surface of the water column. This was done to enhance reflection and mitigate the influence of reflected light originating from the bottom of the tank. Following the experiment, only a small area inside the OWC required cleaning to remove the glass bubbles without causing any contamination concerns. An ultrasonic wave probe was deployed at the centre of the OWC to obtain the reference height value of the water column. This probe provided essential data for the validation of the optical measurement results. Additionally, a resistance wave probe was positioned a few meters in front of the OWC to acquire information regarding the incoming wave characteristics.

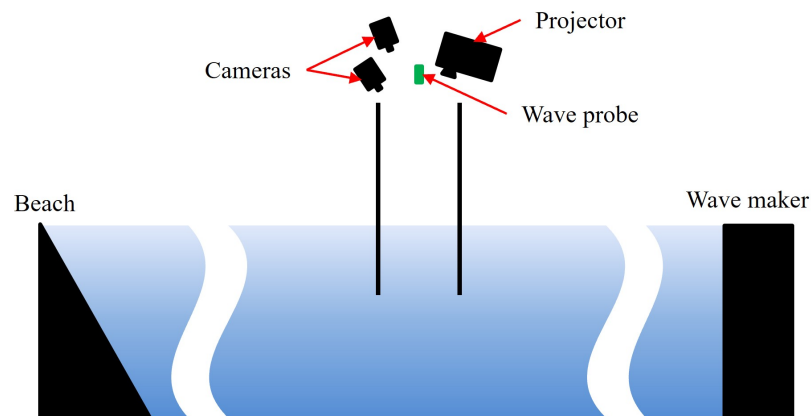


Figure 4.2: Experiment setup of the OWC.

In order to measure the water surface inside the OWC using the optical technique, the model dimensions must meet certain requirements. Due to relying on the camera capturing the projection on the water surface, the model diameter must be large enough to allow the cameras to capture the variation in the internal water surface from the top. There must be sufficient space for the projection area to remain unaffected by the cameras, meanwhile enabling it to cover the surface

of the water column as much as possible.

4.2.4 Test plan

Ocean structures often utilise a crucial parameter called the Response Amplitude Operator (RAO) to assess their dynamic response to waves. This parameter is determined by dividing the amplitude of the dynamic response by the wave height and effectively represents the magnitude of the dynamic response of the structures in waves. It is desirable to minimise RAO values for most marine structures within the frequency range of waves present in their working area to enhance the operational capabilities in the ocean. However, wave energy devices aim to maximise their RAO values within the frequency domain of waves to optimise their energy capture potential.

In the assessment of OWC devices, the determination of the RAO value was predicated upon the division of water column height by wave data acquired through the utilisation of a resistance wave probe. The formulation of this experimental approach was guided by the dynamic responsiveness exhibited by the OWC, with consideration given to the selection of incoming wave frequencies. The RAO exhibits a tendency towards one at the low-frequency end, while it approaches zero at the high-frequency end. To enhance the clarity in illustrating the response of the device, one low-frequency (0.4Hz) wave and one high-frequency (1.15Hz) wave were chosen. Simultaneously, the natural frequency of the device and its proximal frequencies were chosen for comprehensive analysis. Previous tests conducted at the Kelvin Hydrodynamics Laboratory have identified the peak RAO value of the OWC device at the frequency of 0.779Hz. Consequently, in this experiment, five data points were selected in the vicinity of the peak frequency (0.779Hz) to illustrate the variation trend near the peak. A detailed test matrix outlining the specific points selection was provided in Table 4.2.

Table 4.2: Test matrix for OWC

Test ID	Wave frequency (Hz)	Wave amplitude (mm)
01	0.400	10
02	0.693	10
03	0.750	10
04	0.779	10
05	0.795	10
06	0.866	10
07	1.150	10

4.3 Results

4.3.1 Calibration uncertainty

In this section, the calibration results of ultrasonic wave probes and the optical method used in the experiment are presented in Table 4.3 to estimate uncertainties, following the guidelines from ITTC. The standard estimated error (SEE) obtained from the study was 0.231mm, slightly exceeding the specified technical resolution from the manufacturer. This deviation was likely due to the environmental factors impacting sound propagation velocity during calibration. It also introduces supplementary sources of uncertainty, such as A/D conversion uncertainty. All these disparities yield an unequal calibration factor and result in a final wave probe measurement uncertainty of $\pm 0.693\text{mm}$ at a 95% confidence level in this test. Furthermore, the calibration error of the optical technique was estimated by the same method mentioned in Section 3.2.2, yielding a measurement uncertainty of $\pm 0.602\text{mm}$ at a 95% confidence level.

4.3.2 Measured results

In this experiment, the measurement results from the optical technique were compared with those from the ultrasonic wave probe. Notably, the ultrasonic wave

Table 4.3: Calibration of the Ultrasonic wave probe and optical method

Real distance (mm)	Ultrasonic wave probe (mm)	Optical technique (mm)
0.000	-0.000	0.000
4.000	-4.269	4.299
8.000	-7.781	8.322
12.000	-12.367	11.975
16.000	-15.872	15.972
20.000	-19.740	19.879
24.000	-23.787	24.289
28.000	-28.099	27.802
32.000	-31.977	31.717

probe inherently computes the average value across a confined region during the data processing phase. To facilitate a more robust comparison, two distinct outcomes generated by the optical technique were employed. The first result involved the utilisation of data extracted from the central point within the measurement area, while the second result utilised the average value derived from the central region of a circular area with a diameter measuring 28mm.

As shown in Figure 4.3, during the measurement of the inner water column within an Oscillating Water Column (OWC) device, the disparity between the average value within the central region and the value at the central point is notably minimal. This observation implies that, despite the ultrasonic probe measuring the average value of an area, its influence on the outcomes within this experiment remains marginal. Furthermore, this observation establishes a foundational element for asserting the dependability of subsequent result comparisons.

Figure 4.3 reveals a notable observation: the measured results obtained through both methodologies exhibit a high degree of temporal alignment, thus suggesting a congruence between the two approaches. In order to better verify the accuracy of the optical technique, a *sine* fitting was subsequently applied to all measurement outcomes. A time period after the wave stabilised was used for fitting. A

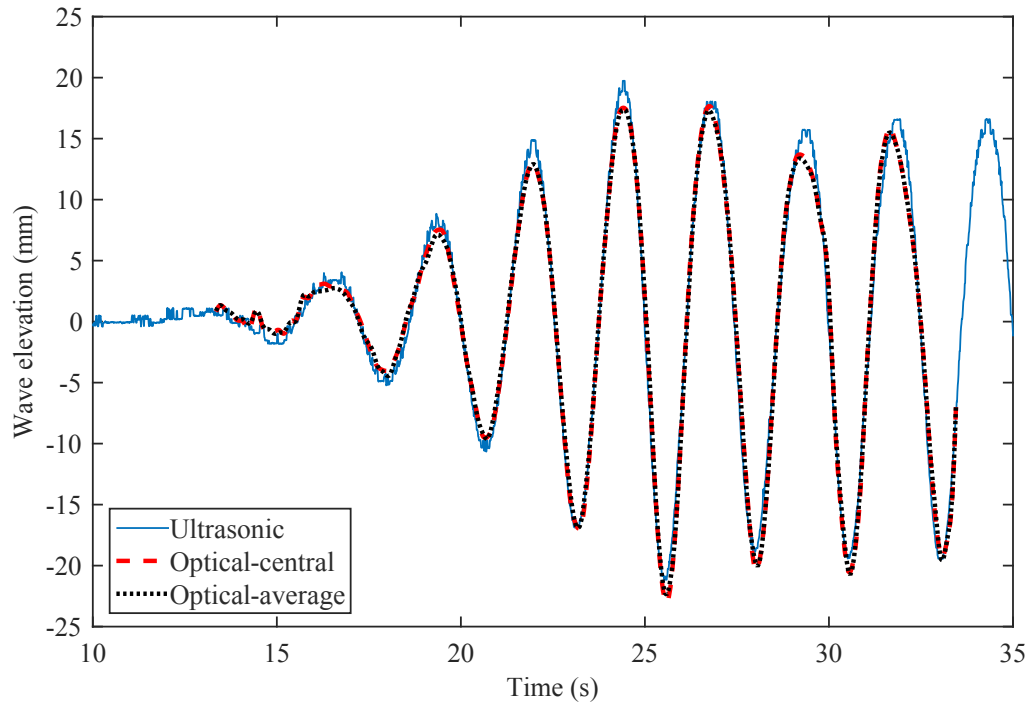


Figure 4.3: Comparison of measurement results.

comparative analysis of the amplitudes within the fitting results, as presented in Table 4.4, yielded a maximum deviation of 0.892mm, which is included in the combination of the uncertainty from these two measurements.

Table 4.4: The water column motion amplitude obtained after *sine* fitting of the measurement results

Wave frequency (Hz)	Ultrasonic wave probe (mm)	Optical technique (mm)
0.400	17.921	18.789
0.693	43.177	43.238
0.750	49.251	49.190
0.779	105.732	104.840
0.795	49.251	49.190
0.866	13.079	13.637
1.150	0.671	0.983

Based on the second-order linear ordinary differential equation (ODE) for a

Chapter 4. Water surface inside Oscillating Water Column

damped harmonic oscillator, at low frequencies, the marine structures exhibit a tendency to move in synchrony with the incident waves. Conversely, at high frequencies, the devices display a greater degree of stability in their response to the wave action. This behaviour is also observed in the movement of the water column within the OWC. The key process is determining the RAO of the OWC in this experiment, which involved the division of the water column heights acquired through the ultrasonic wave probe and the optical technique by the wave heights measured using the resistance wave probe. The results of this analysis were visually represented in Figure 4.4, where the RAO data was graphically depicted. One of the key observations from the RAO data was the manifestation of dynamic response characteristics of the OWC device. Specifically, by examining the RAO data depicted in Figure 4.4, several critical frequency points stood out. At the frequency of 0.400Hz, the RAO of the water column is approximately 1, indicating a strong correlation between the wave motion and the movement of the water column. Conversely, at the frequency of 1.150Hz, the RAO approached 0, suggesting a minimal response of the OWC device to waves at this frequency. Notably, at the frequency of 0.779Hz, the RAO reached its peak value, signifying an optimal response regime for the device. The identification of this peak becomes pivotal in establishing operational parameters that optimise energy conversion within the OWC system.

Upon tests beyond the natural frequency, a precipitous decline in the RAO value is discerned at higher frequencies. This precipitous descent signals a swift diminution in the efficiency of the OWC device within environments characterised by higher frequencies. Conversely, on the lower-frequency side, the gradient of the RAO curve exhibits a comparatively subdued descent. This observation suggests that lower frequencies possess the potential to yield more sustained energy output, particularly when subjected to appropriate control methodologies. The contrast

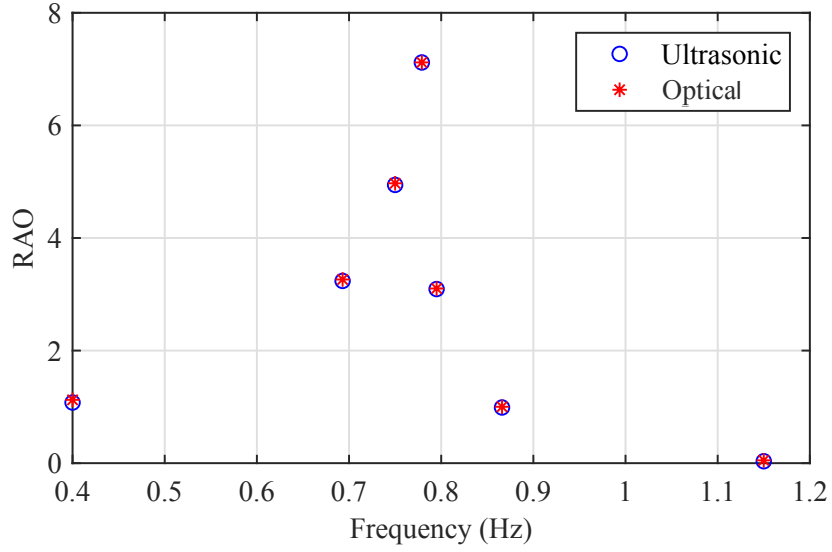


Figure 4.4: Response Amplitude Operator (RAO) of these two wave measurement techniques.

in the gradient on either side of the natural frequency imparts valuable insights into the differential energy extraction potential based on the frequency profile, informing strategic considerations in the design and optimisation of OWC devices.

The influence of uncertainty in the draft, particularly with regard to the estimation of the natural frequency of the OWC, constitutes a critical aspect of the analysis. To assess this influence, a fundamental assumption was made, positing the OWC as a rigid body. This assumption is paramount as it allows for the estimation of the natural frequency ω_n using Equation 4.1. ρ represents the density of water, while g signifies the gravitational acceleration. A_w denotes the water plane area of the tube, with d representing the draft of the device and D denoting the diameter of the tube.

$$\omega_n = \sqrt{\frac{\rho \cdot g \cdot A_w}{\rho \cdot d \cdot A_w + \frac{4}{3} \cdot \rho \cdot \left(\frac{D}{2}\right)^3}} \quad (4.1)$$

In this equation, the second term within the denominator corresponds to an em-

pirical equation designed for the estimation of the frequency-independent vertical added mass for a disk. A comprehensive discussion of this empirical equation can be found in the work of Bayoumi (2013), in which the authors delve into the intricate details of estimating the natural frequency of the OWC. Upon employing Equation 4.1 and incorporating the specific parameters pertaining to the OWC under investigation, the calculated natural frequency of the device was determined to be 0.777Hz. It is noteworthy that this calculated value closely approximated the experimental results. However, the presence of viscosity within the fluid medium introduces a notable caveat, necessitating consideration. According to fluid dynamics principles, the presence of viscosity tends to reduce the oscillation frequency, making it smaller than the theoretically estimated value. Thus, in this context, the presence of uncertainty in the draft arises from the need to account for this discrepancy, elucidating the rationale behind the higher natural frequency observed. When the error associated with the draft estimation is duly incorporated, the natural frequency is observed to fall within a specific range, spanning from 0.773 ~ 0.782Hz. Notably, the higher natural frequency obtained through this analysis suggests that the actual draft line of the OWC is situated lower than the initially designed draft. This observation underscores the significance of considering uncertainties and the impact they may exert on the estimation of critical parameters, such as the natural frequency in the context of OWC systems. Consequently, these findings shed light on the importance of accounting for factors like viscosity and draft estimation accuracy in the pursuit of accurate OWC system modelling and design.

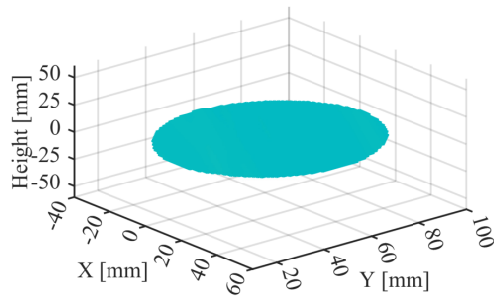
Currently, the investigation into the aforementioned assumption about the water surface inside the OWC is incomplete, mainly due to limitations imposed by available equipment. In a previous study (Çelik and Altunkaynak, 2018, 2021), a restricted deployment of three wave probes was utilised within the device to mea-

Chapter 4. Water surface inside Oscillating Water Column

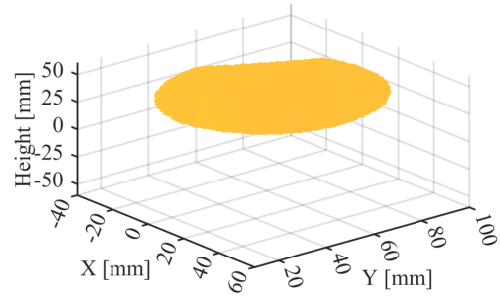
sure surface height along the wave propagation axis. These probes were strategically positioned near the front, middle, and rear walls of the device. However, the data from these probes introduced uncertainties that varied in their respective measurements. Consequently, drawing definitive conclusions about the water surface configuration within the device based solely on these measurements lacks robust confidence.

The utilisation of the optical technique in these tests revealed phenomena aligning with the initially assumed flat nature of the water column surface. As shown in Figure 4.5, despite some disturbance at the peak condition, the water column surface displays a planar shape in a full wave period (T_p). When the water column was subjected to the ascent induced by incident waves, the measured water surface area became narrower due to the projector projection method. Conversely, during the descent phase of the water column, a larger area was captured. Following the discussion in Section 2.4, an increase in measurement error was accompanied at this stage.

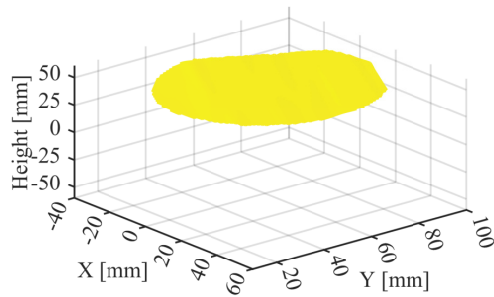
Chapter 4. Water surface inside Oscillating Water Column



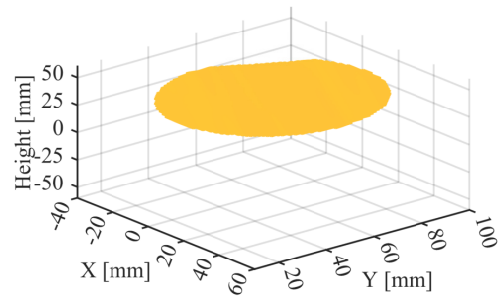
(a) $t=0$



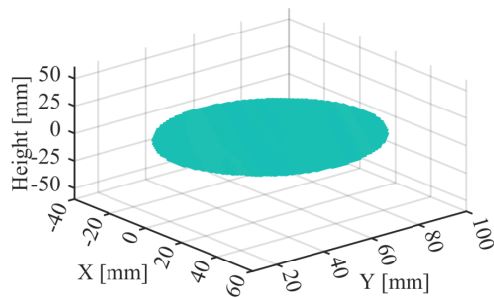
(b) $t = \frac{1}{8}T_p$



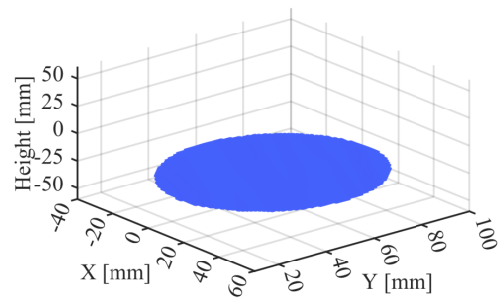
(c) $t = \frac{2}{8}T_p$



(d) $t = \frac{3}{8}T_p$



(e) $t = \frac{4}{8}T_p$



(f) $t = \frac{5}{8}T_p$

Chapter 4. Water surface inside Oscillating Water Column

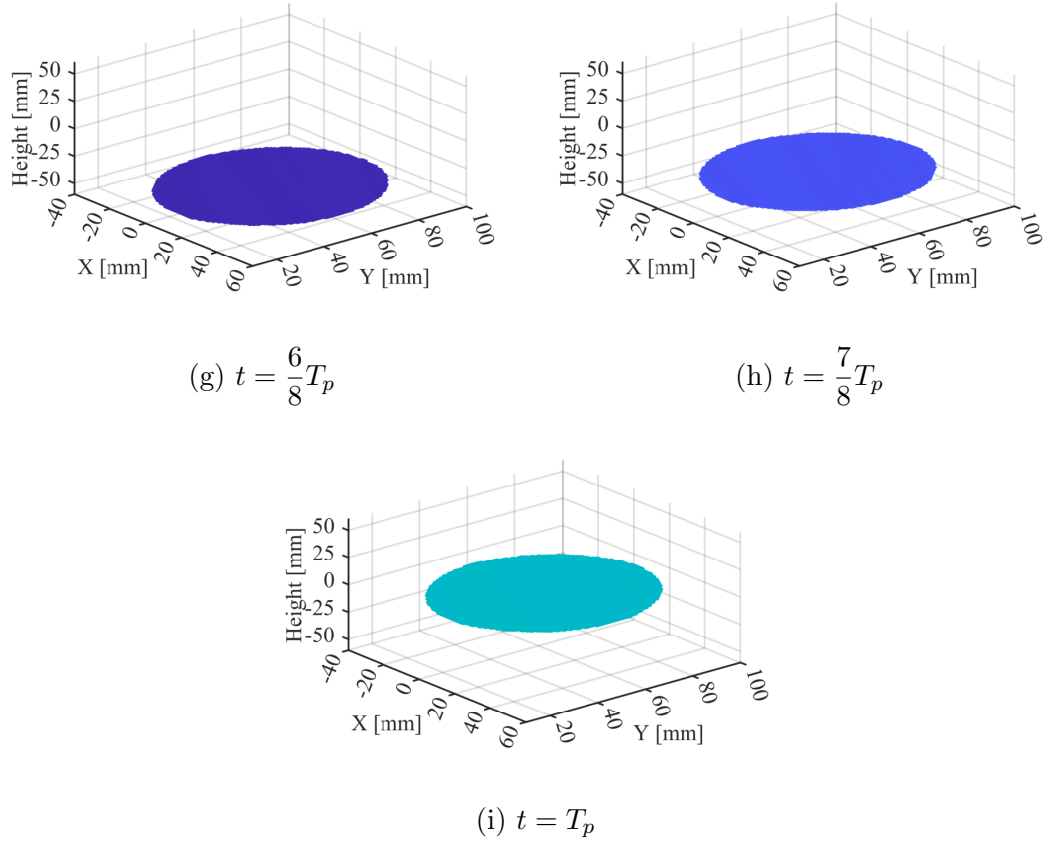


Figure 4.5: Water surface inside the OWC in one wave period (T_p).

Although the overall configuration appears uniform and can be approximated by its midpoint, there is a slight angle between the wave surface and the xy plane. This deviation is attributed to the application of a rotation matrix in the test, which contains some errors. However, these errors do not significantly impact the results, as the angle between the water surface and the xy plane is approximately 0.75° . The resulting difference is around 0.01%, which is considered negligible.

Unfortunately, the existing experimental setup imposes limitations, preventing the concurrent measurement of the water surface with the Power Take-off (PTO) system attached. Overcoming this limitation requires further modifications to make the system able to record the water surface under operational

conditions. It is worth noting that these adjustments are part of the ongoing efforts to enhance the experimental setup. By implementing these refinements, a more comprehensive understanding of the OWC device efficiency is aimed to be established, thereby contributing to a more informed assessment of their overall performance.

4.4 Summary

In conclusion, this study sought to address the existing limitations in understanding the spatial distribution of the water column surface inside an Oscillating Water Column (OWC) device by employing the optical wave measurement technique detailed in Chapter 2. The application of this emerging technique allowed for a more nuanced exploration of the complex dynamics within the OWC device.

The experimental investigation, conducted using a Fixed Symmetry Cylindrical OWC (FSCOWC) device in the controlled environment of the large towing tank at Kelvin Hydrodynamics Laboratory, utilised advanced measurement techniques. The results delved into the calibration uncertainties associated with the ultrasonic wave probes and the optical technique. The calibration error analysis revealed an estimated uncertainty in wave probe measurements and optical technique measurements of $\pm 0.693\text{mm}$ and $\pm 0.602\text{mm}$, respectively, at a 95% confidence level. Subsequent comparisons of measurement results between the optical technique and ultrasonic wave probe highlighted minimal disparities, affirming the reliability of the optical method.

Furthermore, the study explored the dynamic response characteristics of the OWC device by analysing the Response Amplitude Operator (RAO) curve. The findings showcased critical frequency points, providing insights into the optimal response regime and efficiency of the device. Notably, the analysis beyond the natural frequency underscored the potential for sustained energy output at lower

Chapter 4. Water surface inside Oscillating Water Column

frequencies, guiding considerations for OWC device design and optimisation.

The influence of uncertainties in the draft estimation, particularly in the context of the natural frequency, was addressed. This emphasised the significance of acknowledging uncertainties for accurate OWC system modelling.

While the investigation into the water surface configuration within the OWC remained incomplete due to equipment limitations, the utilisation of the optical technique revealed phenomena aligning with the initially assumed flat nature of the water column surface. Despite some distortion near the edge of the filming area, the overall configuration appeared uniform, with negligible deviations.

In conclusion, the findings of this study contribute to the evolving field of OWC technology, offering valuable insights into the spatial dynamics and operational considerations of these devices. The analysis presented in this chapter underscores the importance of addressing uncertainties, refining experimental setups, and embracing innovative measurement techniques for advancing the understanding and optimisation of OWC systems for sustainable wave energy conversion.

Chapter 5

Underwater ellipsoid

5.1 Introduction

Vehicles navigating in water generate waves, resulting in the generation of corresponding wave resistance. As one of the components of hydrodynamic resistance, wave resistance plays an important role in hull design, operation, and performance. Understanding the wave field is of paramount importance for predicting the behaviour of these vehicles, optimising their missions, and ensuring their safety. Recent advancements in underwater technology, such as the development of underwater Remotely Operated Vehicles (ROV) and Autonomous Underwater Vehicles (AUV), have expanded research focus beyond wave fields solely generated by surface-piercing vehicles.

The early research proposed an analytical equation to quantify the wave resistance encountered by underwater ellipsoids (Havelock, 1931). It also examines the effect of different aspect ratios (representing the proportions of length, width, and height) on the relationship between wave resistance and velocity and found that different aspect ratios had little effect on the results. Subsequently, with the advancement of technology, different numerical methods were proposed to

Chapter 5. Underwater ellipsoid

study the wave patterns and other related content created by the movement of the underwater model (Amiri et al., 2019; Wilson-Haffenden et al., 2009; Wu et al., 2019; Xue et al., 2020). Even though these numerical studies proposed some rigorous theoretical foundations, the experimental data are still needed to support their findings.

An experiment on the resistance components of an underwater ellipsoid was first tested in the towing tank of the Iowa Institute of Hydraulic Research (Farell and Güven, 1973). However, due to technical limitations, wave information was not collected at that time. In the subsequent phases of the research, the complexity of obtaining a comprehensive wave field requires a specific measurement process, as elucidated in Kim's study (Kim et al., 2001). The experimental process is complex and time-consuming, and the results rely on certain assumptions. Therefore, there is not much complete wave surface information currently measured using this method. Later, the large number of airborne images monitoring sea surface conditions was used as a valuable resource for in-depth analysis, especially in studying the characteristics of the Kelvin wave system caused by the movement of surface or underwater vehicles (Rabaud and Moisy, 2013; Xue et al., 2021). At the same time, with the rapid development of computer vision, the use of this technology to measure wave fields and water surfaces has attracted more and more attention. Whether it is the movement of objects on the water surface or underwater, the wave field information generated has been measured (Gomit et al., 2013; Wang et al., 2020). However, current computer vision methods require special treatment of the water, such as particle addition or dye infusion.

With the proposed optical technique in this thesis for measuring the wave/water surface, The wave field generated by the uniform motion of an underwater ellipsoid is studied. The wave elevations in both temporal and spatial aspects were obtained to provide more detailed wave information.

5.2 Experiment

The experiment was performed in the 3D Compact Wave Tank mentioned in Section 2.3.1.

5.2.1 Model

The ellipsoid model utilised in this experiment was crafted from Divinycell foam, a material with good robustness and capable of withstanding compressive strength of up to 1 MPa. Consequently, throughout the experimental procedure, it could be ensured that the shape of the model remained unchanged. Due to the significantly lower density of foam compared to that of water, it became necessary to introduce additional mass blocks within the foam structure to maintain a neutral buoyant condition for the ellipsoid when submerged (see Figure 5.1). The selection of the size of the model was based on prior research (Havelock, 1931) and the dimensions of the water tank. The final dimensions were determined to be a length of 500mm, with both width and height measuring 100mm. In an effort to mitigate the effects of viscosity within the small-scale model, the entire surface of the model was coated with paint and subsequently subjected to a smoothing treatment.

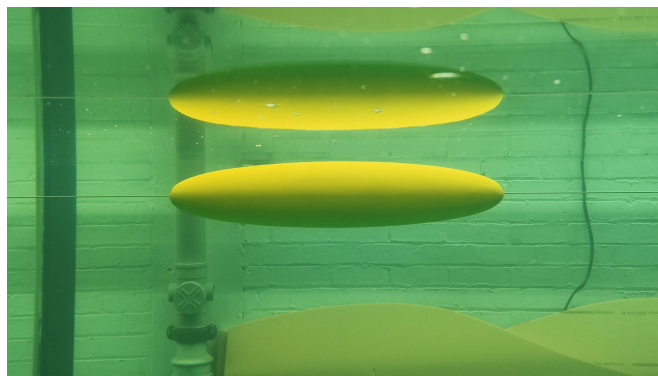


Figure 5.1: The ellipsoidal model maintains neutral buoyancy in water.

5.2.2 Setup

The experimental setup was based on the underwater model towing experiments performed before (Kozin and Zemlyak, 2012). In order to build such a towing system, two $90\times 90\text{mm}$ extrusions were utilised above the water surface in the 3D compact wave tank, to which two $45\times 45\text{mm}$ extrusions are respectively fixed perpendicular to the water surface. Each end of the $45\times 45\text{mm}$ extrusions was equipped with a pulley (see Figure 5.2), one submerged underwater and the other positioned above the water surface. A stepper motor was fixed on one of the extrusions, approximately 300mm from the top. Attached to the motor shaft was a 10.00mm diameter collar. A thin fishing line (0.40mm in diameter) was wound around this collar and passed through four pulleys, connecting two ends of the model to form a closed loop. The fishing line was pre-tensioned to ensure it remained taut, limiting the motion of the model as much as possible. Additionally, the tension ensured that the friction between the line and the collar could drive the model at the set velocity. A stainless steel wire was secured to the two $45\times 45\text{mm}$ extrusions and penetrated the centerline of the model (Figure 5.2), also tensioned to maintain a taut state using the turnbuckle. This further minimised motion in directions other than the travel direction. Consequently, the difference between the submerged depths of the model at the two ends of the stainless wire is only 1.00mm.

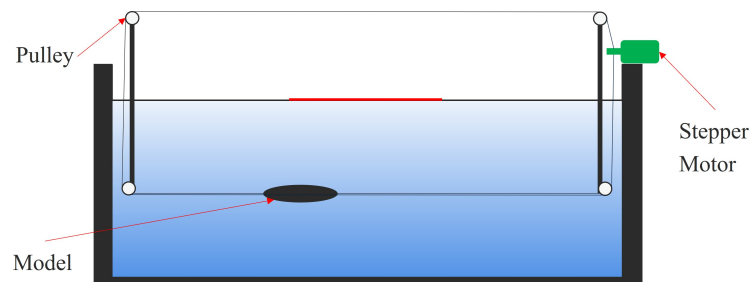


Figure 5.2: Details of the experimental setup, the red line indicates the projection area on the water surface.

Chapter 5. Underwater ellipsoid

For the projection light source in the experiment, an Optoma projector was selected. It provided a luminous intensity of approximately 4000 lumens and achieved a projection quality of 1080p. The projector was fixed on one side of the water tank, elevated 1m above the water surface. The projection area was located on the opposite side of the model towing path to avoid the reflection of the underwater ellipsoid on the projected pattern, which could affect subsequent processing. Two Z Cam E2 movie cameras (Figure 5.3) were employed to capture the results at 4k resolution and 60Hz frame rate. The distance between the camera centres and the centre of the projection area was also approximately 1m to ensure minimal errors in restoring the water surface wave information.



Figure 5.3: Projector (left) and cameras (right) used for the stereo vision system.

The control of the stepper motor was accomplished using the MyRIO device manufactured by National Instruments, along with its accompanying LabVIEW software. The overall process involved the design of a program within the LabVIEW software to define the desired motion parameters for the model. Subsequently, these parameters were transmitted to the MyRIO device, which generated the necessary control signals for the stepper motor. These control signals were subsequently read and implemented by the stepper motor drive. The Geckodrive G203V model was employed as the driver in this experiment to ensure precise control over the stepper motor. This driver can ensure precise control over the stepper motor by offering the capability to subdivide each stepper motor step into ten micro steps. Additionally, this feature had the advantage of providing

greater control over the position of the model, enhancing the overall accuracy and reliability of the experimental setup. Overall, the combination of the MyRIO device, LabVIEW software, and the Geakodrive G203V driver facilitated a robust and precise control system for the stepper motor in the experiment.

5.3 Results

In this section, the accuracy of the proposed optical technique was initially assessed through validation tests. With this information, this technique was then utilised to measure the wave field created by the underwater ellipsoid. Meanwhile, the velocity measurement was also performed by using a computer vision method with one camera, which will be discussed in the following subsection.

5.3.1 Validation of the optical technique

The detailed information for the calibration process is mentioned in Section 2.3.3. As a result, the error in this experiment was approximately 0.41 pixels. To estimate the effect of the calibration error on the wave/water surface measurement, the validation procedure was executed in accordance with the methodology outlined in Section 3.2.2. A flat plate featuring a distinct image pattern was driven by a linear actuator with a fixed displacement step of 4mm, continuously moving in the negative direction of the z-coordinate axis within the global coordinate system. This process was recorded using the calibrated cameras, and subsequently, the entire movement sequence of the plate was reconstructed to measure the displacement for each step. A comparison between the measured displacement and the preset displacement was conducted. The maximum difference between each step was found to be only 0.32mm. According to the guidelines established by ITTC regulation, the calculated estimated error is 0.164mm. Consequently, it

can be inferred that with a 95% confidence level, the true value falls within a range of $\pm 0.492\text{mm}$ from the measured value.

5.3.2 Velocity measurement and results

In the experiment, although the stepper motor exhibits high precision, ensuring the accuracy of results requires measuring the velocity of the ellipsoid. Given that the entire experimental setup was unprecedented within the Kelvin Hydrodynamics Laboratory, existing techniques for velocity measurement within the laboratory were found to be inadequate. To address this issue, computer vision techniques were employed. As shown in Figure 2.4, the sidewalls of the 3D compact wave tank are constructed from glass, facilitating observations of phenomena occurring within the water tank. This provides a convenient condition for measuring the velocity of the ellipsoid. A third camera (a smartphone) was positioned alongside the water tank to document the movement of the underwater ellipsoid. To establish precise length measurements in the real world, a rule was introduced along the stainless wire within the image plane of the camera. The video footage was captured at a frame rate of 30 fps. To measure the velocity of the model, two video frames with a temporal separation of six frames were randomly selected and compared the deviation in pixel positions between them. This analysis allowed us to calculate the displacement, which, in turn, unveiled the velocity. This procedure was performed three times, and the average results were chosen as the final motion velocity of the ellipsoid.

From the results in Table 5.1, it can be seen that the maximum deviation from the predetermined movement velocity is 5.65%. Although there is a certain deviation, the control signal was not modified here because the velocities were measured. With the known velocities, the wave field measurement experiments can proceed.

Table 5.1: Velocity measurement

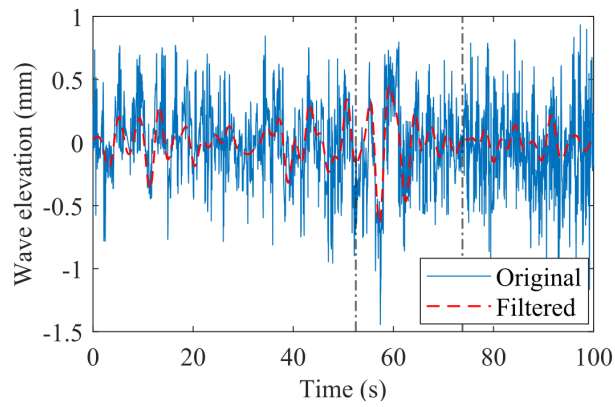
Designed velocity (m/s)	Measured velocity (m/s)	Error (%)
0.177	0.187	5.65
0.301	0.305	1.33
0.554	0.572	3.41

5.3.3 Wave information measurement

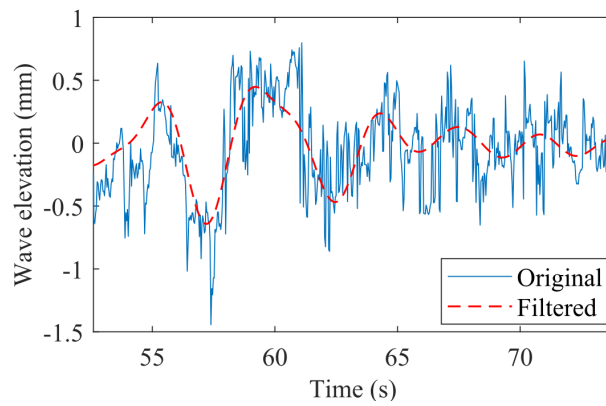
Due to time constraints, measurements of the ellipsoid wavefield were limited to two different velocities at a specific submersion depth. The final testing conditions involved a distance of 25mm from the upper surface of the ellipsoid to the water surface, with velocities denoted as 0.187 m/s and 0.305 m/s, respectively.

The measurement result at a velocity of 0.187 m/s is presented in Figure 5.4. It can be seen from the time history data of the entire motion process that when the ellipsoid moves at this velocity, the waves generated are minimal. The original measurement results are seriously affected by measurement noise, making it difficult to obtain valuable data. In this case, a low-pass filter was applied to the original data, leading to a substantial reduction in measurement noise. As a result, the Bernoulli hump caused by the motion of the ellipsoid can be easily distinguished. Subsequently, data on the transverse waves were also relatively well obtained. The time difference between the two peaks of the Bernoulli hump is measured to be 3.73 s.

In Figure 5.5, spatial information is depicted, synthesising data derived from multiple frames. This wave field is a product of the uniform motion of an underwater ellipsoid, resulting in a correlation between the spatial location of the Bernoulli hump and the position of the ellipsoid. The employed optical measurement technique facilitates the synchronous collection of both temporal and spatial information. Consequently, it becomes feasible to estimate the velocity of the ellipsoid from the acquired measurements. In this particular instance, the



(a)



(b)

Figure 5.4: When the speed is 0.187m/s, the measured time history data of a specific point on the centre line. (a) Data for the entire movement. The vertical cursors indicate the period during which the ellipsoid passes through the measurement area. (b) Zoom in to the range within the cursors.

Chapter 5. Underwater ellipsoid

measured distance between the two peaks is 0.694m. With this measured distance and the corresponding time data, the velocity of the ellipsoid can be calculated as 0.186m/s, a value close to the experimental settings.

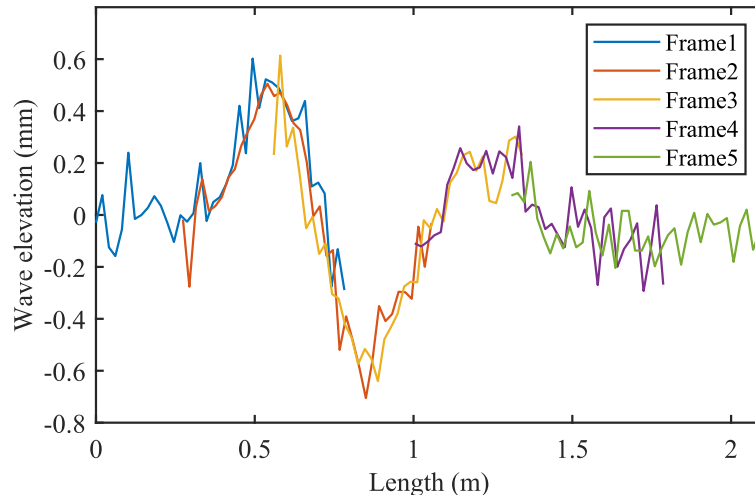


Figure 5.5: When the speed is 0.187m/s, the measured spatial data. The number only represents the order of each frame and does not refer to the frame number in the video.

However, in surface measurements (shown in Figure 5.6), due to the presence of noise at all measurement points on the surface, only the Bernoulli hump was observable under this velocity condition. The Transverse wave, being minimal, cannot be discerned from the surface measurement results.

Conversely, when the velocity matches 0.305 m/s, the entire wave group formed by the uniform motion of the ellipsoid was distinctly visible. Figure 5.7 provides a visual representation of the time history data along the centre axis of the ellipsoid, acquired using the same methodology as in the prior scenario. In this case, the time difference between the two peaks of the Bernoulli hump was measured to be 1.77 seconds.

Meanwhile, the spatial information was shown in Figure 5.8, comprising results synthesised from multiple frames. Building upon the approach applied in

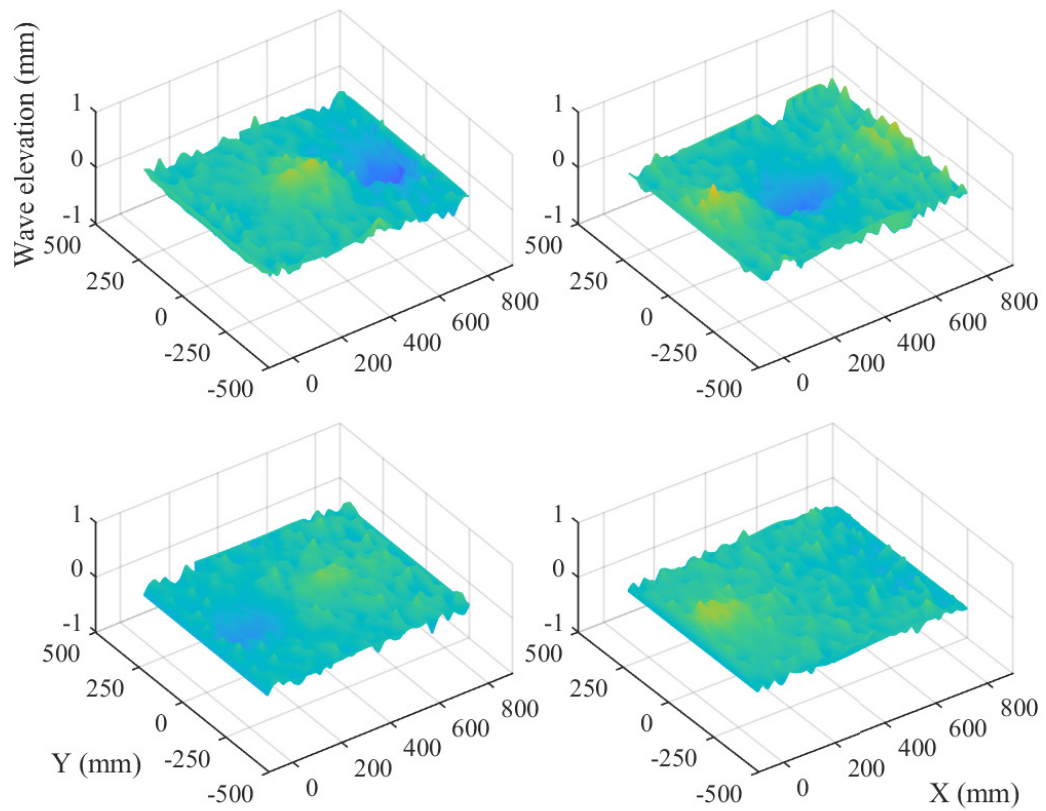
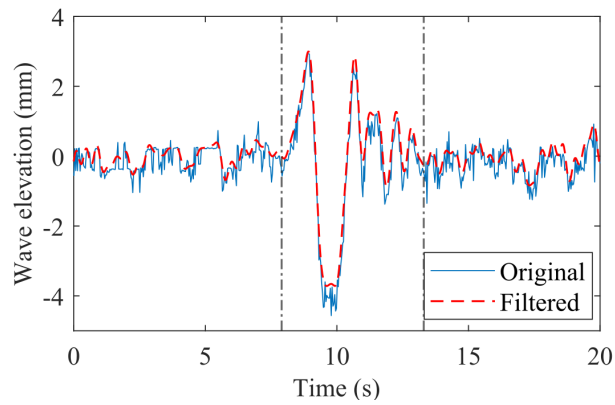
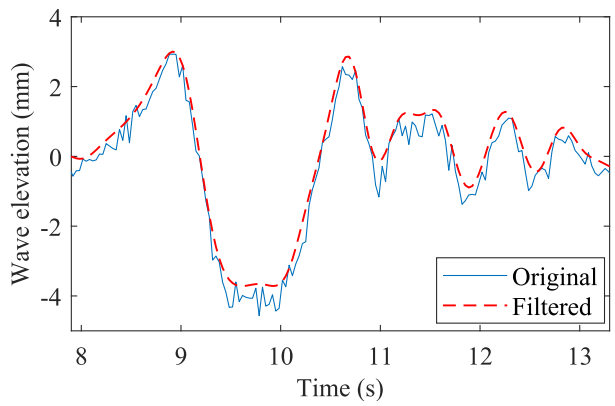


Figure 5.6: Wave Field Measurement at Velocity 0.187 m/s: Entering Moment (Upper Left), Model Arrival at Middle (Upper Right), Leaving Moment (Lower Left), Model Fully Exiting (Lower Right)



(a)



(b)

Figure 5.7: When the velocity was 0.305 m/s, the measured time history data of a specific point on the centre line. (a) Data for the entire movement. The vertical cursors indicate the period during which the ellipsoid passes through the measurement area. (b) Zoom in to the range within the cursors.

the low-velocity case, the measured distance between the two peaks in this instance was 0.54m. Employing this distance and the corresponding time data, the velocity of the ellipsoid was calculated as 0.305 m/s, a value consistent with the experimental settings.

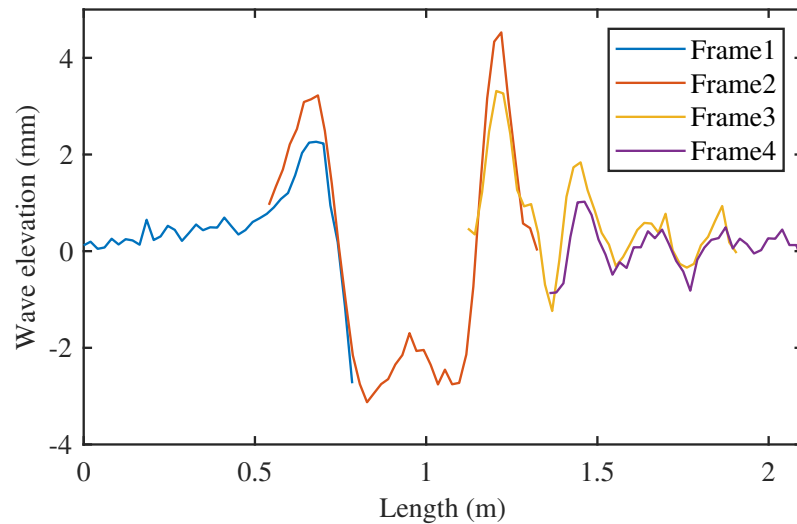
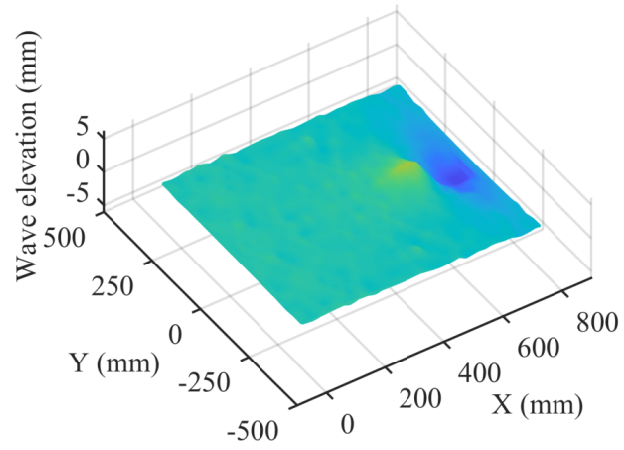
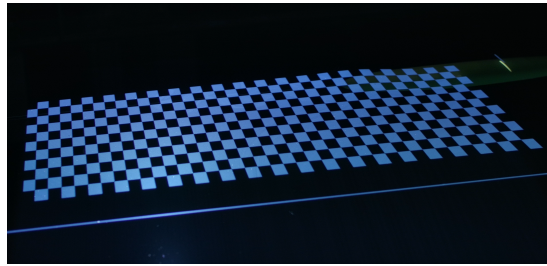


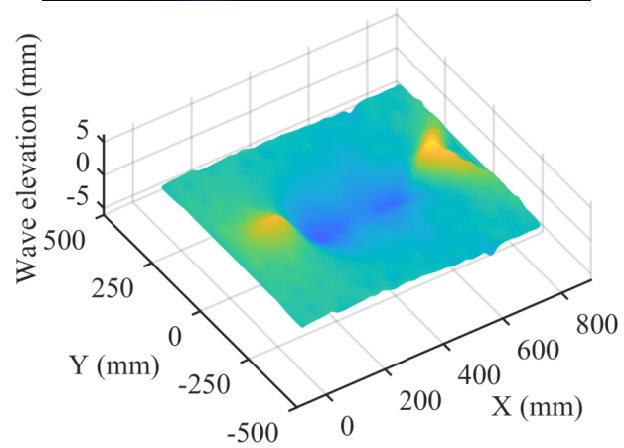
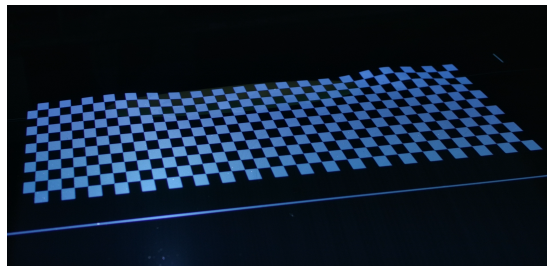
Figure 5.8: When the velocity was 0.305 m/s, the measured spatial data. The number only represents the order of each frame and does not refer to the frame number in the video.

Furthermore, a comparison between the results obtained from wave field measurements (Figure 5.9 and the previous low-speed case reveals that, as the generated wave elevation increases, the influence of noise gradually diminishes. The appearance of the entire wave field becomes distinctly visible, including previously imperceptible Transverse waves behind the ellipsoid, which are now observable. It is important to note that while the complete reconstruction of the entire ellipsoidal motion remains pending due to time constraints, this task remains feasible and can be accomplished through subsequent adjustments.

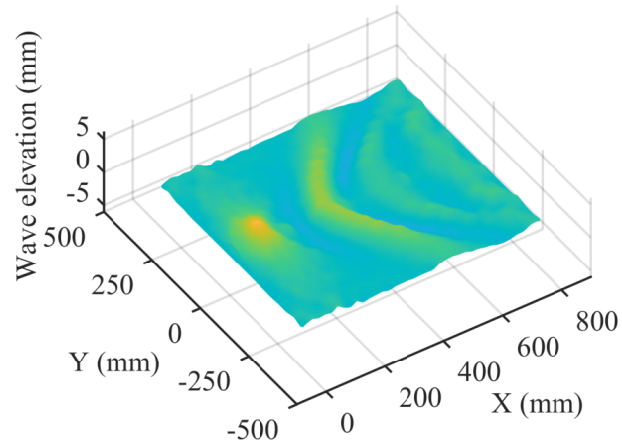
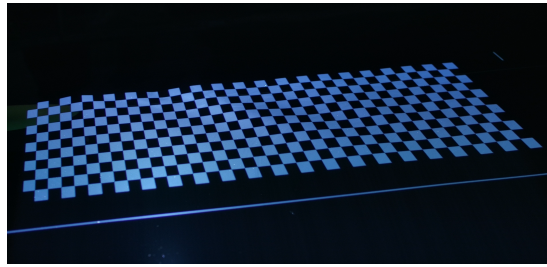
Chapter 5. Underwater ellipsoid



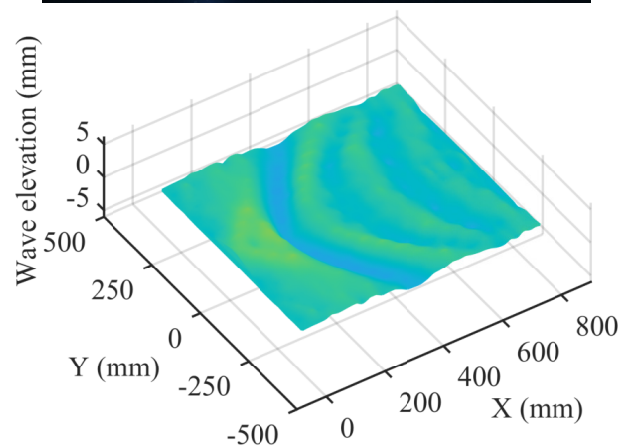
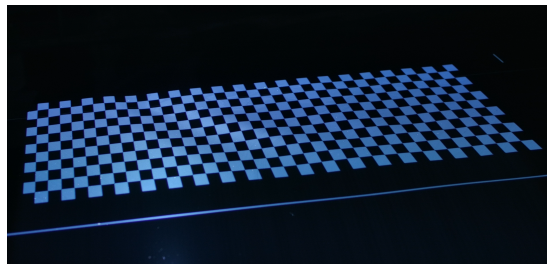
(a) entering the measurement area;



(b) at the middle of the measurement area;



(c) leaving the measurement area;



(d) Transverse waves behind the ellipsoid;

Figure 5.9: Wave field measurement at the velocity equal to 0.305 m/s.

5.4 Summary

In conclusion, this chapter focused on the implementation of the proposed optical technique for measuring the wave/water surface generated by the uniform motion of an underwater ellipsoid. The accuracy of the optical technique was rigorously assessed through calibration, revealing a minimal error of approximately 0.41 pixels. The validation procedure, adhering to established methodologies, demonstrated that the calibrated cameras provided precise measurements, with a calculated estimated error well within acceptable limits.

To address the challenge of measuring the velocity of the underwater ellipsoid in an unprecedented experimental setup, computer vision techniques were employed. The use of a smartphone camera alongside the 3D compact wave tank allowed for precise velocity measurements, ensuring the accuracy of the experimental results. The calculated velocity deviations were within 5 %, affirming the reliability of the employed towing method. The subsequent section delved into the measurement of the wave field generated by the underwater ellipsoid at different velocities and submersion depths. Despite time constraints limiting measurements to two specific velocities, the optical technique facilitated the synchronous collection of both temporal and spatial information. Low-pass filtering was applied to reduce measurement noise, enabling the identification of key wave features, such as the Bernoulli hump.

The presented results showcased the effectiveness of the optical technique in capturing wave information, with distinct visualisations of wave patterns at different velocities. The correlation between spatial location and the motion of the ellipsoid was evident, allowing for the estimation of ellipsoid velocity from the acquired measurements. While challenges such as noise in surface measurements were acknowledged, the overall success of the optical technique in revealing wave field details highlighted its potential for comprehensive wave surface analysis.

Chapter 6

Lock entry problem

6.1 Introduction

The issue of vessel entry into locks has always been a hot topic, particularly due to the existence of inland waterway transportation, which requires continuous improvements to the efficiency of canal navigation through ongoing lock modifications. From the perspective of ship fluid dynamics, the manoeuvrability of a vessel in a lock is affected by many factors, and our understanding of these factors is not yet complete.

In the experiment section, the entire development process gradually increased restrictions from pure shallow water conditions to the lock entry, and most of the experiments focused on measuring information about the ships themselves. In earlier experiments, the motion of ships in shallow water conditions was mainly measured (Fujino, 1968; Kazerooni and Seif, 2014). After that, a side wall that narrowed the channel was added to the shallow water, and the forces and yaw moment acting on the ship were measured (Vantorre et al., 2003). In a recent open model test conducted jointly by Flanders Hydraulics Research and Ghent University (Vantorre and Delefortrie, 2013; Vergote et al., 2013), in addition to

Chapter 6. Lock entry problem

the propulsive force, position, and speed of the self-propelled ship model, the waves at the bow of the ship and the end of the lock were also measured.

Several different methods have been developed in the simulation section (Du et al., 2017; Helsloot, 2016; Yuan, 2019; Tezdogan et al., 2016), but ultimately, the accuracy of these methods has been validated mainly using information from the vessel itself. Although the water surface height information at the bow of the ship and the end of the lock has been measured in experiments, this is not sufficient to verify the water surface information during the simulated process of entering a lock. The currently available wave measurement methods have been described in detail in Chapter 3 and will not be repeated here. In the low-speed lock entry problem, the amplitude change of the water surface is limited and the space is compact, so wave penetration probes are unsuitable. Ultrasonic wave probes measure the average value of a small area due to the limitation of their size and require sufficient sound wave reflection, so they are also not suitable for this type of problem. optical techniques have a much smaller space requirement than other methods. Only a pattern needs to be projected onto the water surface from a distance. Even after the ship enters the lock and gradually destroys the projected pattern, the remaining part of the pattern can still provide wave information during this process. This makes optical techniques more suitable than other wave measurement technologies for lock entry problems.

This chapter employs the optical measurement technique currently in development to investigate water surface height information when a small underwater ellipsoid (length: 0.5m) enters a rectangular lock. Subsequently, the study extends to the water surface height information when a large floating box (length: 2.4m) enters the lock. The objective is to gain a deeper understanding of the lock entry problem through the analysis of wave field information. Furthermore, this experimental data can provide a more detailed and compelling validation basis

for future numerical simulation methods.

6.2 Experiment set up

6.2.1 Underwater ellipsoid

In this experimental phase, a ship lock model was incorporated based on the underwater ellipsoid towing experiment outlined in Chapter 5. The distance from the highest point on the upper surface of the ellipsoid to the water surface remained at 25mm. The ellipsoid continued to be drawn by a stepper motor along a taut stainless steel cable at a consistent speed. Recognising that the entry into the lock chamber generally occurs at low velocities, three distinct low-speed conditions with F_r values of 0.025, 0.050, and 0.135 were implemented for this experiment. The actual motion speeds were measured to be F_r values of 0.022, 0.051, and 0.136 using the video recording method outlined in the preceding chapter.

The lock model was constructed using Marine Plywood. 45*45mm extrusions were affixed to maintain the lock model in the correct position, as shown in Figure 6.1. The width of the lock area was 1.5 times the width of the ellipsoid, measuring 150mm, while the length was 1000mm, twice the length of the ellipsoid. Two different water depths within the dock area were employed. The first water depth is the depth of the 3D compact wave tank itself, amounting to 1000mm. The second water depth was set at 175mm, achieved by inserting a plate parallel to the still water surface in the lock area. Simultaneously, the space beneath this plate was sealed at the lock entrance. In this configuration, the entry of the ellipsoid into the lock equated to an instantaneous transition from deep water to shallow water conditions.

Due to the restricted lock area and shallow water conditions, the large image

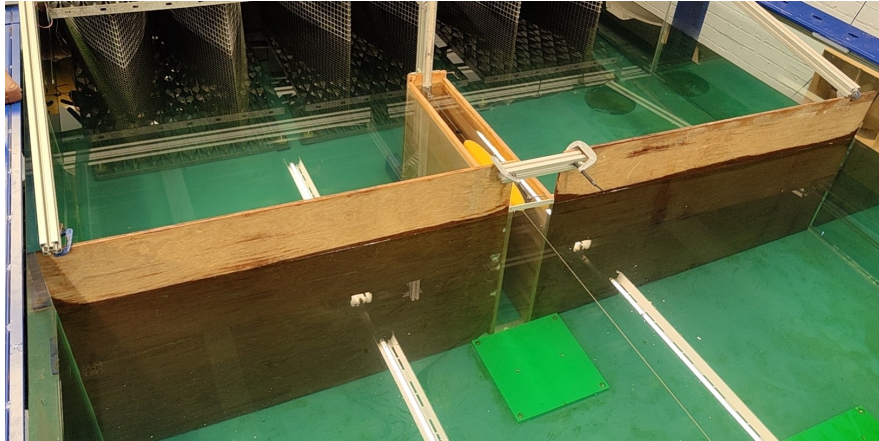


Figure 6.1: Ellipsoid inside the lock area.

pattern reflected from both the side walls and the bottom will destroy the feature points on the water surface. To address this, a laser pointer, specifically a Class 1M with a green light, was employed to establish a stable feature point on the water surface. Importantly, this choice ensured the absence of safety concerns throughout the experiment process. Four measurement points were chosen in this setup. As shown in Figure 6.2, these points include $Wp1$ at the centre of the lock gate, $Wp2$ at the midpoint of the lock, $Wp3$ halfway along the length of the lock near the side wall, and $Wp4$ positioned 50mm from the end of the lock.

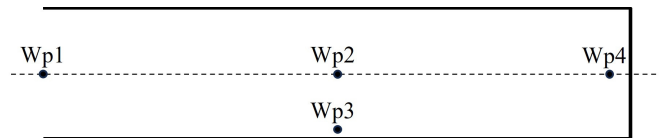


Figure 6.2: Measurement points inside the lock area.

6.2.2 Floating box

After the underwater ellipsoid experiment, a large floating object entering the lock experiment was performed to address a more realistic problem. Following the research done by Delefortrie et al. (2008), the Third Set of lock chambers of

the Panama Canal was chosen as the lock model. To simplify filming and ensure distinct visual clarity, a box model was chosen due to its straightforward structure. The dimensions of the ship hull from the Bulk carrier, closely aligning with a block coefficient (CB) closest to 1, were utilised in designing the experimental box model. The experiment was conducted at a scale factor of 1/115, and the geometric details are outlined in Table 6.1.

Table 6.1: Geometry details of the box and lock

Component	Parameters	Value (mm)
Lock	Length	3500.0 ± 1.0
	Breadth	50.0 ± 1.0
	Height	30.0 ± 1.0
	Draft	22.5 ± 1.0
Box	Length	2400.0 ± 1.0
	Breadth	40.0 ± 1.0
	Height	20.0 ± 1.0
	Draft	15.0 ± 1.0

This experiment took place within the large towing tank at the Kelvin Hydrodynamics Laboratory (refer to Section 2.3.1). To secure the lock model in place, L-shaped wooden frames were affixed to its sidewalls, allowing weights to be positioned for stability (refer to Figure 6.3). Four resistance wave probes were attached to these side walls, positioned at distances of $0.30 \pm 0.01\text{m}$ ($Wp1$), $2.40 \pm 0.01\text{m}$ ($Wp2$), $2.80 \pm 0.01\text{m}$ ($Wp3$), and $3.20 \pm 0.02\text{m}$ ($Wp4$) from the gate of the lock. The box was towed by the carriage equipped with a computer-controlled digital drive, capable of achieving speeds of up to 5m/s. It is worth noting that the box was rigidly fixed to the carriage, ensuring that apart from the motion provided by the carriage, no additional movement was allowed for the box itself. At the connection point of the carriage and the box, a 6-DOF load cell provided by a company called Kistler was set to capture the resistance of the box during the lock entry process.

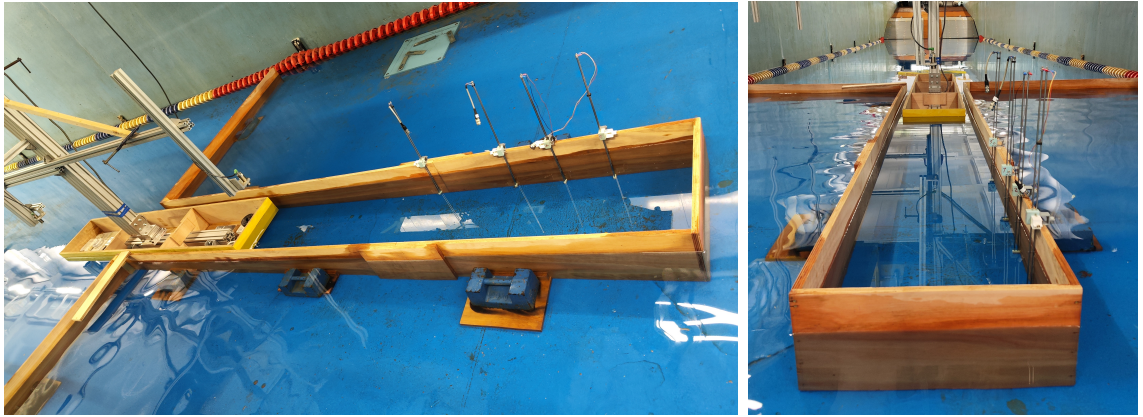


Figure 6.3: Floating box entering the lock.

As shown in Figure 6.4, the optical technique under development was employed to measure the water surface within the lock area. The Optoma projector, previously discussed in Chapter 5, served as the projection light source for this experiment as well. Positioned at the end of the lock and elevated 3m from the middle, the projector covered 90% of the lock area. Given the shallow water conditions, the particle described in Chapter 2 was utilised to mitigate the impact of light reflection from the side walls and bottom. Two Z Cam E2 movie cameras, capturing results at 4k resolution and 60Hz frame rate, were positioned on a sub-carriage above the towing tank, situated more than 5m away from the middle of the lock.

6.3 Results

The hydrodynamics of ships navigating through a lock are inevitably influenced by shallow water and bank effects. As a ship enters or leaves a lock with a sealed end, it triggers a piston phenomenon caused by trapped waves between the ship and the lock end.

As the ship enters the lock at a constant speed U , the volume of water confined



Figure 6.4: Experiment setup for measuring the water surface inside the lock area

between the ship and the closed end increases, calculated as

$$\Delta V = U A_s(t) \cdot \Delta t \quad (6.1)$$

where A_s denotes the cross-sectional area of the ship at time t . This causes a rise in the free surface within the lock. Simultaneously, this increased water volume prompts a return flow, equal to the water leaking through the narrow gap between the ship and the lock (Yuan, 2019). As the distance between the bow of the ship and the lock end diminishes, the velocity of this return flow increases. Meanwhile, the free surface drops.

In this section, both results from the underwater ellipsoid and floating box will be presented and analysed.

6.3.1 Ellipsoid

As shown in Figure 6.5, the comparison between the measured results from both $Wp2$ (middle of the lock) and $Wp3$ (near the middle of the side wall) was conducted at first. t_1 denoted the moment the ellipsoid reached the lock gate, and t_2 indicated the instant the model was entirely inside the lock. Despite some

data noise, a remarkable alignment in the overall trends of data curves was observed. This suggests a consistent behaviour of the water surface at the plane perpendicular to the model propagation direction. Thus, the data points along the centreline can be sufficiently representative.

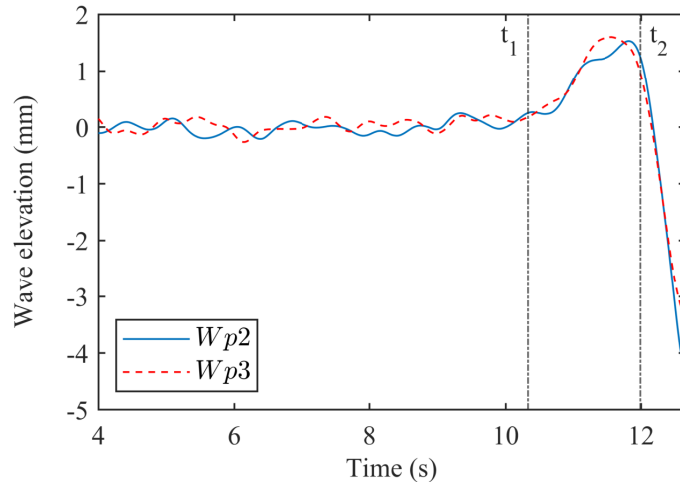
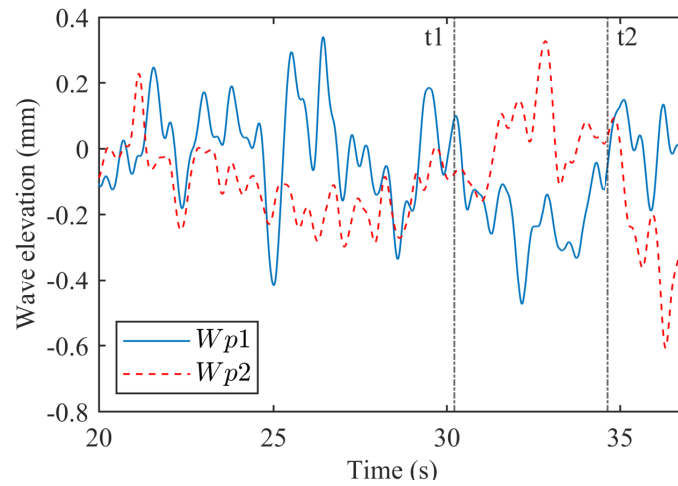


Figure 6.5: Time history results of $Wp2$ and $Wp3$.

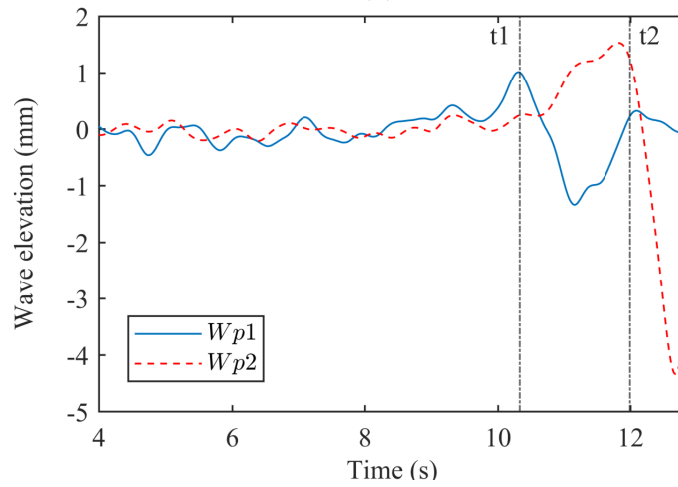
Measurements of the free surface elevation were captured at $Wp1$ (centre point at the gate), $Wp2$ and $Wp3$ when the ellipsoid entered the lock at different speeds under 1m water depth. The recorded free surface elevation is visually presented in Figure 6.6. As shown in Figure 6.6 (a), the variance in the free surface was insignificantly small when F_r equated to 0.051, yielding a limited informative value. However, at F_r equal to 0.136 (see Figure 6.6 (b)), the free surface behaviour exhibited greater variance. At the onset of the entry of the lock, the water heights at $Wp1$ and $Wp2$ displayed differing trends. Analysis from the wavefield results in Chapter 5 provides some insight into the wave information at $Wp1$. The underwater ellipsoid generated a Bernoulli hump to move along with the model, observable in the results at $Wp1$. Concurrently, the piston phenomena at this stage caused a rise in the free surface between the model and the lock end. Post the complete entry of the lock, a noticeable drop in water height at $Wp2$

Chapter 6. Lock entry problem

occurred. Because it was determined by the pressure field around the ellipsoid. Even though it was not very clear, the lower speed case showed the same trend. Unfortunately, owing to operational errors, the laser pointer at $Wp4$ failed to function in these cases. Consequently, the piston phenomena inside the lock area could not be fully studied.



(a)



(b)

Figure 6.6: Measured result of the ellipsoid entering the lock under 1m water depth condition. (a) $F_r = 0.051$; (b) $F_r = 0.136$.

With the inclusion of the step bottom, a more intricate hydrodynamics prob-

Chapter 6. Lock entry problem

lem was investigated. As shown in Figure 6.7, the recorded data at $Wp1$ does not exhibit any discernible differences under varying water depth conditions. This suggests that the wave elevation at the lock gate remains unaffected by alterations in the lock depth, primarily relying on the velocity of the model. Meanwhile, the wave elevation within the lock experiences substantial influence from the water depth. Under the stepped bottom condition, the water height at $F_r = 0.051$ ascends to the same level as that observed under the 1m condition at $F_r = 0.136$.

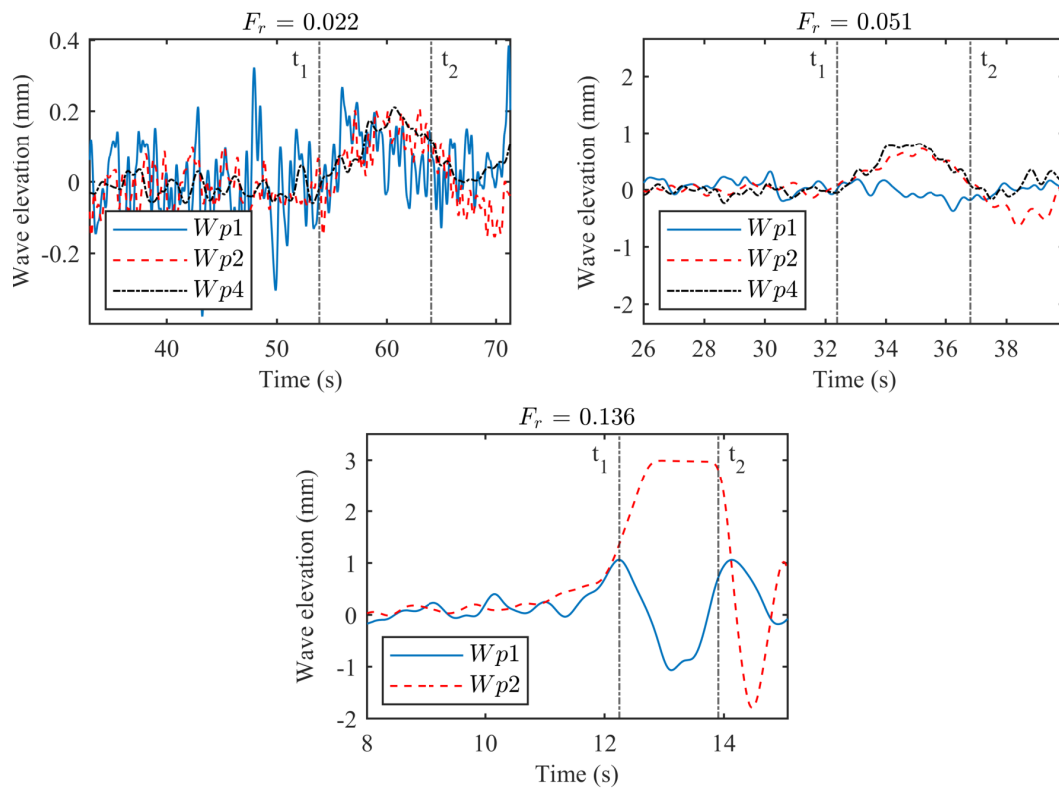


Figure 6.7: Measured result of the ellipsoid entering the lock with the step bottom under different speeds.

The piston phenomena become evidently apparent in Figure 6.7 (a) and (b), as the wave elevation at $Wp4$ (near the end of the lock) was also gauged in these experiments. During the entry phase of the model, the measurement results for

$Wp2$ and $Wp4$ closely coincide. Approaching full entry, the water height at both $Wp2$ and $Wp4$ experiences a simultaneous decline. This suggests that at this specific juncture, the return flow attains its maximum velocity.

6.3.2 Box

Examining the ship lock problem, the investigation extended to the hydrodynamic phenomena encountered during the entry of a box into a lock.

Owing to the introduction of seeding, it is imperative to investigate the impact of the particle on the water surface from the very outset. Within this experiment, the wave probes positioned in the lock recorded water height data, facilitating an investigation into the aforementioned effect. The visual representation of results from the lowest and highest speeds in the experiment is shown in Figure 6.8. In the examination conducted at the slowest speed, there is an observable discrepancy of approximately 5mm in the water height information at $Wp2$ (situated 2.4m away from the lock gate). A similar occurrence is noted in the test with the highest speed at $Wp4$ (located 3.2m away from the gate). Even when accounting for uncertainties in the equipment, this variance suggests that the particle exerts an influence on the behaviour of the water surface. However, other outcomes demonstrate a high degree of concurrence. In essence, the results, whether with or without seeding, exhibit consistency at some level. This deduction prompts further analysis utilising the outcomes derived from the optical technique currently in development.

The wave elevation of box entry at different speeds is shown in Figure 6.9. The X axis denotes the distance from the bow of the box to the gate of the lock. Initially, upon entering the lock, a slight alteration in fluid volume resulted in a negligible change in the free surface. Subsequent entry caused the conversion of kinetic energy into gravitational potential energy, leading to a rapid rise

Chapter 6. Lock entry problem

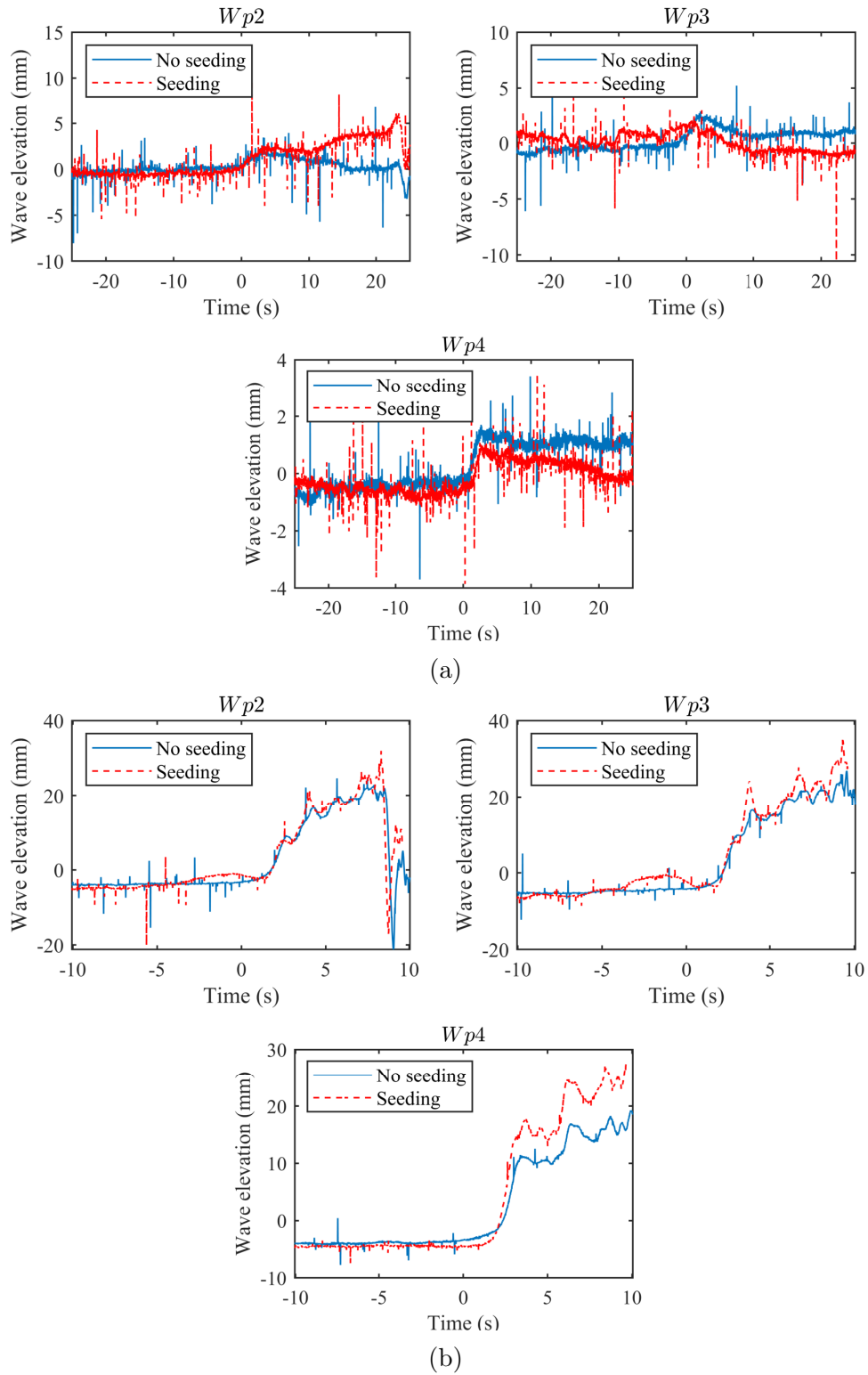


Figure 6.8: Wave probe result of the box entering the lock with and without seeding. (a) $F_r = 0.021$; (b) $F_r = 0.062$.

Chapter 6. Lock entry problem

in the free surface. It is worth noting that, except for $F_r = 0.021$, the water level increases in order according to the distance from the gate. The free surface achieved an initial equilibrium at a position corresponding to 0.9m at speeds of $F_r = 0.021$ and $F_r = 0.041$. However, at $F_r = 0.062$, equilibrium was not attained until the position reached 1.35m. This indicated a balance in the exchange of kinetic energy and gravitational potential energy. Then the gravitational potential energy was converted back into kinetic energy, resulting in fluid outflow and an overall reduction in the free surface. This phenomenon was only observed in the results of *Wp2* and *Wp3* at $F_r = 0.021$. At $F_r = 0.041$, the water height exhibited sustained oscillations around the equilibrium value. At $F_r = 0.062$, a step increase ensued. This is attributed to the limited distance between the lock side walls and the box in this experiment, constraining the flow of fluid from both sides of the box to the outside. In this setup, with increasing speed, the water level will rise even higher. There is a noticeable decline in the latter segment of the measurement results for *Wp2* at various speeds. This decline coincided with the moment the bow of the box passed *Wp2*. The occurrence was attributed to the pressure field generated around the box due to its continuous motion.

The wave filed measurement results were given in Figure 6.10. When entering the lock, the water level initially rises from the gate to the end. Subsequently, the phenomenon of piston action occurs.

The total resistance of the box is shown in Figure 6.11. To effectively depict the variations within the lock at different speeds, the resistance and moment were treated as 0 before the box commenced its entry into the lock. In order to enhance the alignment of the force outcomes, the distance from the bow of the box to the gate of the lock was utilised as the X axis as well. During the trial at the lowest speed, the resistance and moment of the box proved to be inconsequentially small, rendering them of limited informational value. However,

Chapter 6. Lock entry problem

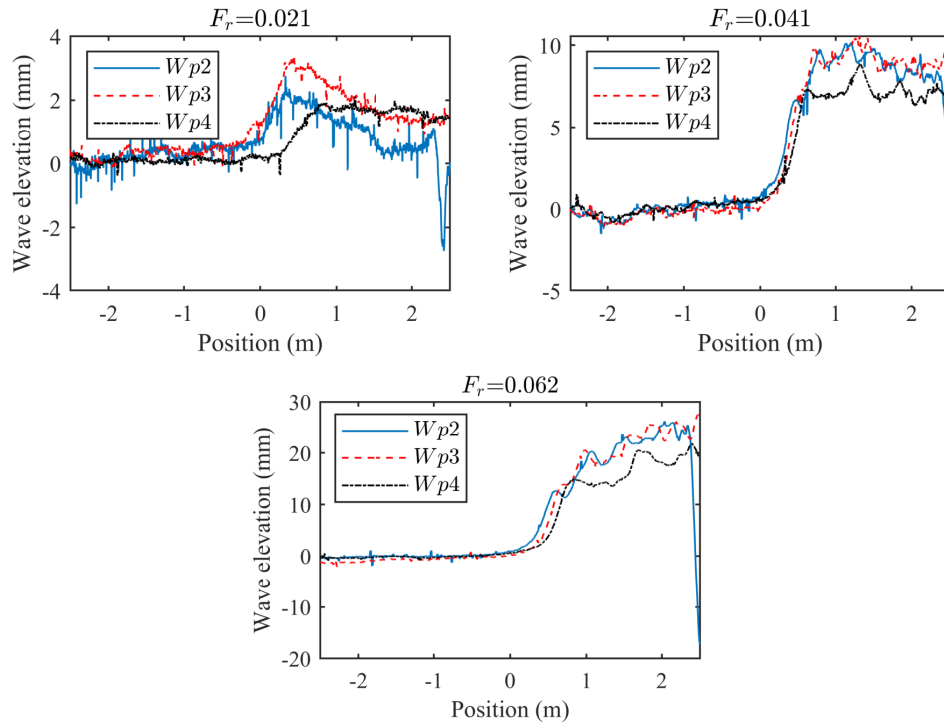


Figure 6.9: Wave probe result of the box entering the lock at different speeds.

at the other two speeds, the resistance exhibits a discernible two-step increment. The initial rise transpires as the box initiates entry into the lock, while the second rise occurs when the free surface within the lock attains its initial equilibrium. Concurrently, in the measurement of moment, the results portray a one-step increment. The initial rise manifests at the entry position, and a peak value is discernible simultaneously with the second rise of the force, even in the test conducted at the lowest speed. Subsequently, the moment fluctuates around the value of the initial rise.

The water level at the front of the box and resistance exhibit a similar step-like rise (refer to Figure 6.12). The fluid in close proximity to the bow of the box is consistently subjected to more pronounced effects of return flow compared to positions nearer to the banks. This disparity can be attributed to the entry of the box, which acts as the primary initiator of the return flow phenomenon.

Chapter 6. Lock entry problem

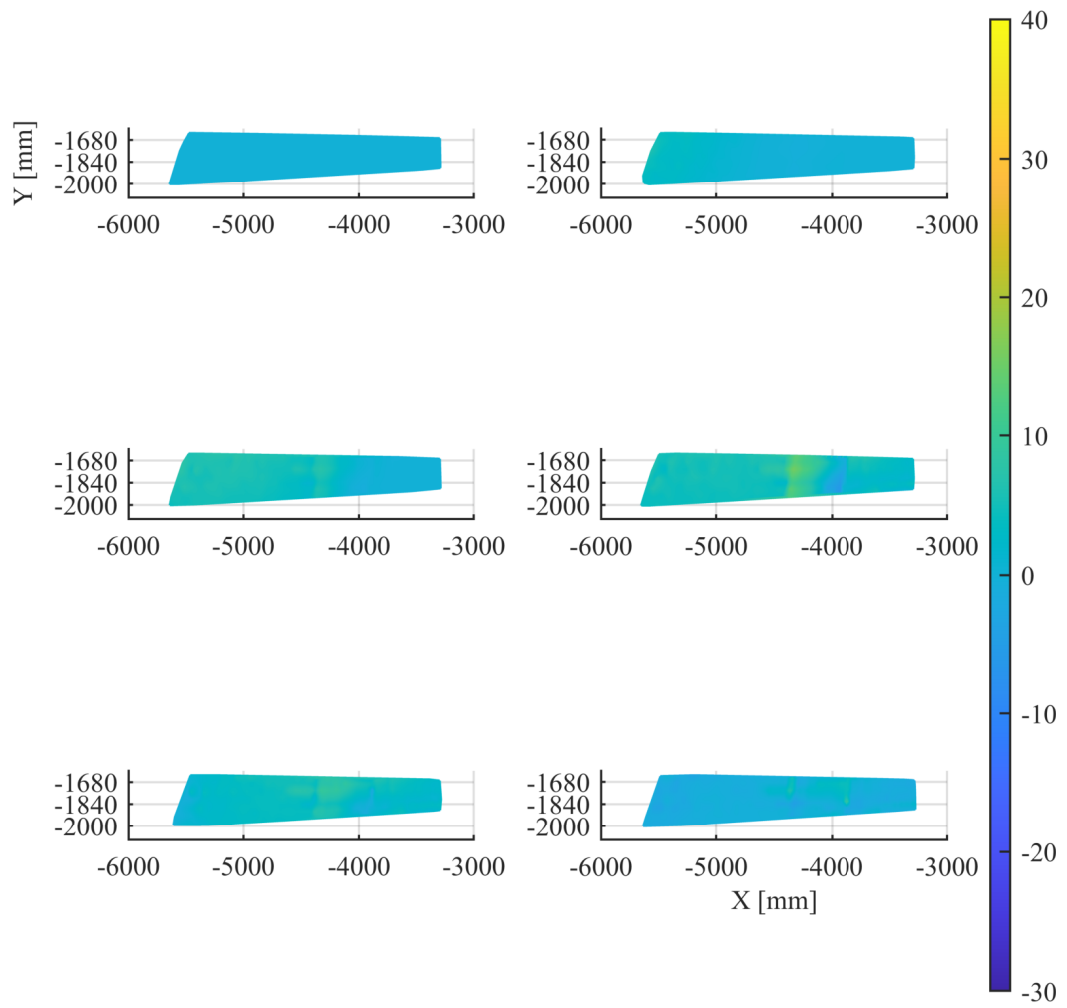


Figure 6.10: Wave field measurement results. From box entry to Piston phenomenon occurs.

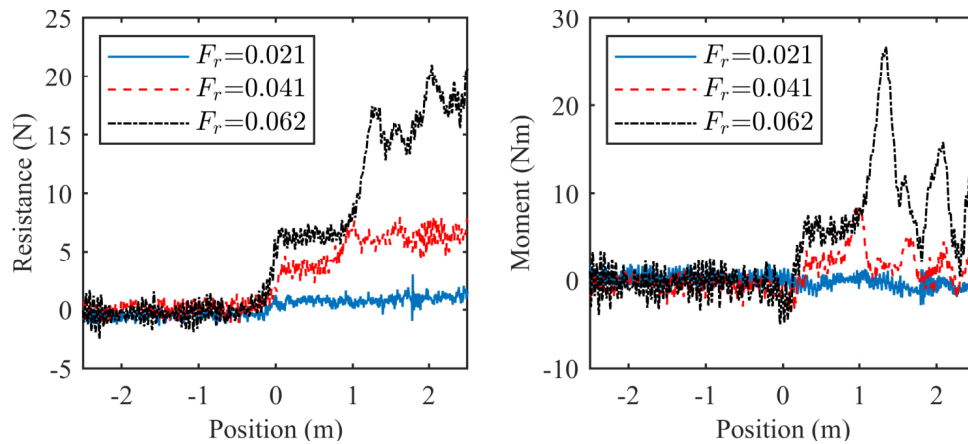


Figure 6.11: Resistance and moment of the box entering the lock at different speeds

As a result, the flow field around the bow, moving in tandem with the box, naturally displays a more pronounced correlation with the return flow in contrast to the free surface at fixed positions situated at a distance from the box. It is noteworthy that the step phenomena observed in the experimental results are closely associated with unsteady effects as well. This elucidates why the step phenomena become more conspicuous as the velocity of the box increases. A heightened entry velocity induces more significant unsteady effects on the free surface within the lock. Furthermore, the unsteady effects of the free surface contribute to the piston phenomenon inside the lock.

6.4 Summary

This research chapter utilised an optical measurement technique under development to explore water surface height information during the entry of a small underwater ellipsoid (length: 0.5m) and a large floating box (length: 2.4m) into a rectangular lock. The primary aim was to comprehensively understand the lock entry problem through the analysis of wave field information, providing a detailed

Chapter 6. Lock entry problem

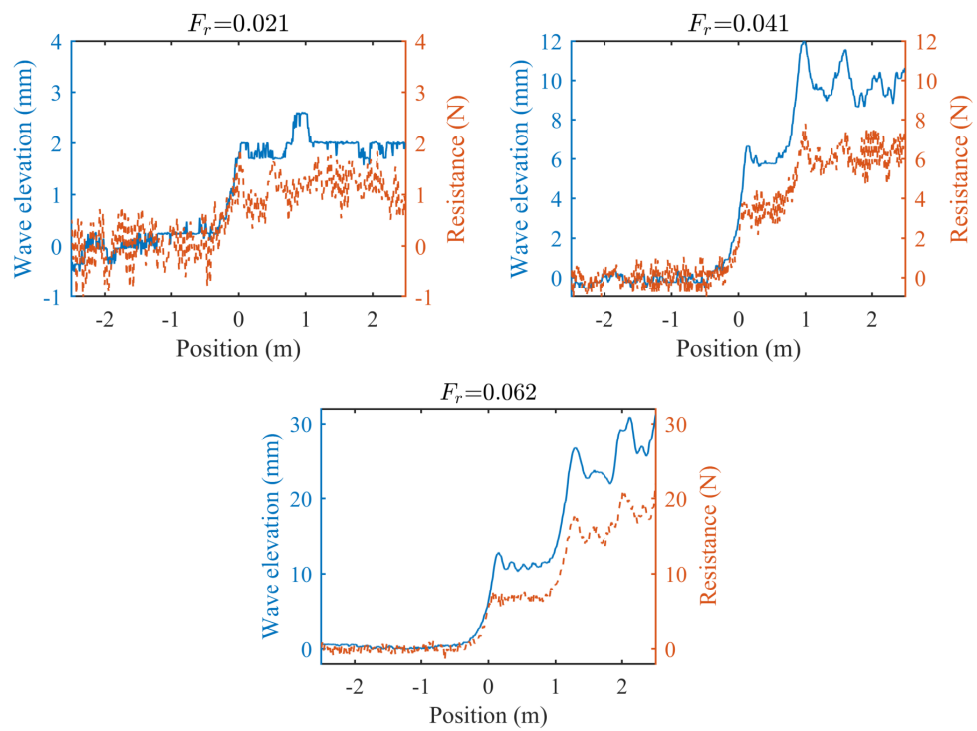


Figure 6.12: Wave and resistance of the box entering the lock at different speeds.

Chapter 6. Lock entry problem

and compelling validation basis for future numerical simulation methods.

The hydrodynamics of ships navigating through a lock are intricately influenced by shallow water and bank effects, manifesting as the Piston phenomenon during entry or exit. As a ship enters at a constant speed, a confined water volume increase leads to a rise in the free surface, accompanied by induced return flow and subsequent free surface drop.

The experimental focus in this chapter includes the entry of an underwater ellipsoid and a floating box into the lock. Examination of the entry of the ellipsoid under different conditions revealed consistent water surface behaviour perpendicular to the model propagation. A Bernoulli hump generated by the ellipsoid and the evident Piston phenomenon during entry, related to return flow velocity, were observed. The introduction of a step bottom added complexity to the hydrodynamics problem.

The investigation extended to the entry of a large floating box. The impact of seeding for the optical technique on the water surface was studied, revealing some influence on the behaviour of the water surface. The wave elevation during box entry at different speeds showed complex hydrodynamics phenomena of return flow and unsteady effect, resulting in fluctuations and step-like increases in the free surface. The resistance and moment of the box exhibited step-like increments, providing insights into the dynamics of box entry.

In summary, the research presented in this chapter contributes valuable insights into the hydrodynamics of lock entry. The optical measurement technique proves effective in capturing detailed wave field information, enhancing the understanding of the complex phenomena associated with ship navigation within a lock. These findings provide a robust foundation for further numerical simulations and contribute to the broader understanding of lock entry dynamics in the field of maritime engineering.

Chapter 7

Conclusions & Future work

7.1 Conclusions

Embarking on an exploration of water wave dynamics and wave-structure interactions, this doctoral thesis constitutes a contribution to the field. The core innovation lies in the introduction and development of a pioneering approach for contactless full-field measurement of water waves, harnessing a combination of stereo vision and structured light with a specific image pattern. The key strength of this methodology lies in its unmatched adaptability in data point spatial density, facilitated by the ease with which the image pattern can be modified. Leveraging sub-pixel point detection, validation tests substantiate its sub-millimetre accuracy, firmly establishing it as a potent tool for reconstructing dynamic water surfaces with precision.

Wave measurement techniques

The various wave measurement techniques were dissected, providing a comprehensive analysis of resistance wave probes, ultrasonic probes, and the proposed optical technique. Through a set of wave tests, their strengths and weaknesses

were explored. In the temporal dimension, resistance wave probes display superior resolution, proving effective up to a specific wave height threshold and ideal for scenarios requiring reference values or data from distant regions. Ultrasonic probes, on the other hand, excel in applications with expansive dimensions and gradual spatial changes. Optical techniques, boasting high spatial resolution, become practical with advanced camera systems, excelling in fine wave field measurements without compromising integrity. The insights gained not only inform the selection of appropriate techniques for distinct experimental scenarios but also lay the groundwork for future advancements in wave measurement technology.

Oscillating Water Column

The proposed optical technique was deployed to overcome limitations in comprehending the spatial distribution of the water column surface within an Oscillating Water Column (OWC) device, a crucial step in understanding and optimising wave energy conversion. Conducted in the controlled environment of Kelvin Hydrodynamics Laboratory's large towing tank, the experimental investigation focused on a Fixed Symmetry Cylindrical OWC (FSCOWC) device, employing advanced measurement techniques. The study delved into the dynamic response characteristics of the OWC device through the analysis of the Response Amplitude Operator (RAO) curve, identifying critical frequency points that offer insights into optimal response regimes and device efficiency. Beyond the natural frequency, the analysis indicated the potential for sustained energy output at lower frequencies, guiding considerations for OWC device design and optimisation.

Addressing uncertainties in draft estimation, especially concerning natural frequency, emphasised the importance of acknowledging uncertainties for accurate OWC system modelling. Despite the incomplete investigation into the water

surface configuration due to equipment limitations, the use of the optical technique revealed a predominantly uniform configuration aligning with the initially assumed flat nature of the water column surface. In conclusion, this study contributes valuable insights into OWC technology, emphasising the need to embrace innovative measurement techniques for advancing sustainable wave energy conversion.

Underwater ellipsoid

The wave/water surface generated by the uniform motion of an underwater ellipsoid was measured by implementing the proposed optical technique. The calibration demonstrated minimal optical technique error of approximately 0.41 pixels, ensuring precision. Computer vision techniques, including a smartphone camera in the 3D compact wave tank setup, accurately measured the velocity of the underwater ellipsoid. The deviations were within 5 %, confirming the reliability of the self-made towing system.

Exploring the wave field at different velocities and depths, the optical technique synchronously collected temporal and spatial data, unveiling key wave features like the Bernoulli hump. Through the application of low-pass filtering, the measurement noise was reduced and able to reveal distinct visualisations of wave patterns at varying velocities. Acknowledging challenges like surface measurement noise, the overall success of the optical technique showcased its potential for comprehensive wave surface analysis, emphasising its effectiveness in capturing intricate wave details.

Lock entry

Extending the optical measurement technique to investigate water surface height during the entry of a small underwater ellipsoid (length: 0.5m) and a large floating

box (length: 2.4m) into a rectangular lock, it delves into the complex hydrodynamics of ship navigation. The primary objective was to grasp the lock entry problem by analysing wave field data and establishing a solid validation basis for future numerical simulations in marine engineering.

The hydrodynamics of ship entry into a lock, influenced by shallow water and bank effects, were explored, revealing a Piston phenomenon during entry. The entry of the underwater ellipsoid demonstrated consistent water surface behaviour perpendicular to the propagation direction of the model, with observable Piston phenomenon and return flow. The introduction of a step bottom added complexity to the hydrodynamics. During the entry of a large floating box, the influence of seeding for the optical technique on the water surface was examined. The wave elevation during box entry at different speeds unveiled complex hydrodynamic phenomena, contributing insights into the dynamics of box entry.

The effectiveness of the optical measurement technique in capturing detailed wave field information was shown. These findings serve as a robust foundation for numerical simulations and enhance the broader understanding of lock entry dynamics in maritime engineering.

In conclusion, this PhD thesis represents a stride forward in the understanding of water wave dynamics and measurement techniques. The novel optical measurement approach, characterised by its adaptability, precision, and reliability, opens new frontiers for research in fluid dynamics and maritime engineering. The analysis of existing wave measurement techniques, combined with experimental applications in diverse scenarios, not only demonstrates the versatility and potential impact of the proposed methodology but also positions it at the forefront of advancements in the field. As the scientific community navigates the analysis of water waves in various contexts, this research provides not only a toolkit for exploration but also a contribution to advancing their understanding of

fluid dynamics in complex environments. The journey outlined in this thesis not only enriches the current state of knowledge but also lays the foundation for continued exploration, innovation, and transformative insights into the fascinating world of water wave dynamics.

7.2 Future improvement

Although the optical technique showcased remarkable performance across various scenarios in this thesis, it is essential to acknowledge certain limitations that were not explored. The utilisation of structured light technology to project discernible patterns onto the water surface necessitates adherence to specific clarity standards for these patterns. This adherence ensures the optimal functionality of stereo vision technology in capturing and aligning feature points. At present, the reflectivity of the water surface relies solely on the presence of dust. In the absence of structures, dust can blanket the entire water surface without affecting pattern clarity. However, upon introducing structures, the radiation and diffraction waves generated alter the distribution of dust, potentially obscuring feature points and rendering the optical technique impractical. However, this constraint can potentially be mitigated by employing a more potent light source. This modification would reduce the requisite dust coverage on the water surface, thereby expanding the applicability of the technique.

Another significant consideration is the limitation imposed by wave steepness. Beyond a certain threshold, cameras may fail to capture reflected light effectively. One potential solution involves deploying additional cameras to encompass a broader range of light reflection directions. Figure 7.1 illustrates a tentative camera installation scheme. Within this camera array, any pair can function as stereo vision cameras. Following calibration, the capture of an object with distinct features in all directions facilitates the integration of reconstruction

results. Feature extraction and pairing from various 3D outcomes enable the alignment of different camera coordinate systems (refer to Section 2.2.1) into a unified global coordinate system.

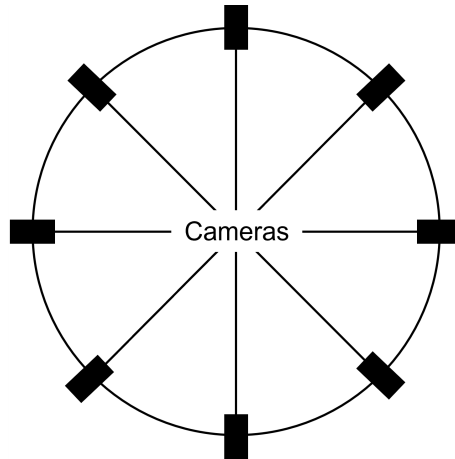


Figure 7.1: New cameras set up in the future.

Additionally, this technique holds promise for achieving real-time measurements. With a higher-performance computer, matrix operations can be executed more rapidly. Furthermore, a lower spatial density image pattern is required. However, the limitation of spatial density for real-time measurement warrants further investigation in future studies.

Bibliography

- M. M. Amiri, S. H. Sphaier, M. A. Vitola, and P. T. Esperança, “Investigation into the wave system of a generic submarine moving along a straight path beneath the free surface,” *European Journal of Mechanics-B/Fluids*, vol. 76, pp. 98–114, 2019.
- F. Aureli, A. Maranzoni, P. Mignosa, and C. Ziveri, “An image processing technique for measuring free surface of dam-break flows,” *Experiments in fluids*, vol. 50, no. 3, pp. 665–675, 2011.
- J. Awange and J. Kiema, “Light detection and ranging (lidar),” in *Environmental Geoinformatics*. Springer, 2019, pp. 291–306.
- A. S.-E. M. Bayoumi, “Development of numerical wave power prediction tool offshore oscillating water column wave energy converter,” 2013.
- F. Bergamasco, A. Torsello, M. Sclavo, F. Barbariol, and A. Benetazzo, “Wass: An open-source pipeline for 3d stereo reconstruction of ocean waves,” *Computers & Geosciences*, vol. 107, pp. 28–36, 2017.
- D. Bergmann, “New approach for automatic surface reconstruction with coded light,” in *Remote sensing and Reconstruction for three-dimensional objects and scenes*, vol. 2572. SPIE, 1995, pp. 2–9.

Bibliography

- C. T. Bishop and M. A. Donelan, “Measuring waves with pressure transducers,” *Coastal Engineering*, vol. 11, no. 4, pp. 309–328, 1987. [Online]. Available: <https://www.sciencedirect.com/science/article/pii/0378383987900317>
- P. Bonneton, D. Lannes, K. Martins, and H. Michallet, “A nonlinear weakly dispersive method for recovering the elevation of irrotational surface waves from pressure measurements,” *Coastal Engineering*, vol. 138, pp. 1–8, 2018.
- K. L. Boyer and A. C. Kak, “Color-encoded structured light for rapid active ranging,” *IEEE Transactions on Pattern Analysis and Machine Intelligence*, no. 1, pp. 14–28, 1987.
- J. Canny, “A computational approach to edge detection,” *IEEE Transactions on pattern analysis and machine intelligence*, no. 6, pp. 679–698, 1986.
- B. Carrhill and R. Hummel, “Experiments with the intensity ratio depth sensor,” *Computer vision, graphics, and image processing*, vol. 32, no. 3, pp. 337–358, 1985.
- D. Caspi, N. Kiryati, and J. Shamir, “Range imaging with adaptive color structured light,” *IEEE Transactions on Pattern analysis and machine intelligence*, vol. 20, no. 5, pp. 470–480, 1998.
- A. Çelik and A. Altunkaynak, “Experimental and analytical investigation on chamber water surface fluctuations and motion behaviours of water column type wave energy converter,” *Ocean Engineering*, vol. 150, pp. 209–220, 2018.
- , “An in depth experimental investigation into effects of incident wave characteristics front wall opening and pto damping on the water column displacement and air differential pressure in an owc chamber,” *Energy*, vol. 230, p. 120827, 2021.

Bibliography

- S. Cochard and C. Ancey, "Tracking the free surface of time-dependent flows: Image processing for the dam-break problem," *Experiments in Fluids*, vol. 44, pp. 59–71, 2008.
- G. Delefortrie, M. Willems, E. Laforce, M. Vantorre, T. De Mulder, J. De Regge, and J. Wong, "Tank test of vessel entry and exit for third set of panama locks," in *The Proceedings of the International Navigation Seminar following PIANC AGA 2008*, China Communications Press, 2008, pp. 517–530.
- U. R. Dhond and J. K. Aggarwal, "Structure from stereo-a review," *IEEE transactions on systems, man, and cybernetics*, vol. 19, no. 6, pp. 1489–1510, 1989.
- D. Douxchamps, D. Devriendt, H. Capart, C. Craeye, B. Macq, and Y. Zech, "Stereoscopic and velocimetric reconstructions of the free surface topography of antidune flows," *Experiments in Fluids*, vol. 39, no. 3, pp. 535–553, 2005.
- P. Du, A. Ouahsine, K. Toan, and P. Sargent, "Simulation of ship maneuvering in a confined waterway using a nonlinear model based on optimization techniques," *Ocean Engineering*, vol. 142, pp. 194–203, 2017.
- A. Elahi, J. Lu, Q.-D. Zhu, and L. Yong, "A single-shot, pixel encoded 3d measurement technique for structure light," *IEEE Access*, vol. 8, pp. 127 254–127 271, 2020.
- D. V. EVANS, "The Oscillating Water Column Wave-energy Device," *IMA Journal of Applied Mathematics*, vol. 22, no. 4, pp. 423–433, 12 1978. [Online]. Available: <https://doi.org/10.1093/imamat/22.4.423>
- D. V. Evans, "Wave-power absorption by systems of oscillating surface pressure distributions," *Journal of Fluid Mechanics*, vol. 114, p. 481–499, 1982.

Bibliography

- C. Farrell and O. Güven, “On the experimental determination of the resistance components of a submerged spheroid,” *Journal of Ship Research*, vol. 17, no. 02, pp. 72–79, 1973.
- A. Fleming, B. Winship, and G. Macfarlane, “Application of photogrammetry for spatial free surface elevation and velocity measurement in wave flumes,” *Proceedings of the Institution of Mechanical Engineers Part M: Journal of Engineering for the Maritime Environment*, 2018.
- M. Fujino, “Experimental studies on ship manoeuvrability in restricted waters,” *International Shipbuilding Progress*, vol. 15, no. 168, pp. 279–301, 1968.
- D. B. Gennery, “Object detection and measurement using stereo vision,” in *Proceedings of the 6th international joint conference on Artificial intelligence-Volume 1*, 1979, pp. 320–327.
- G. Gomit, L. Chatellier, D. Calluau, and L. David, “Free surface measurement by stereo-refraction,” *Experiments in fluids*, vol. 54, no. 6, p. 1540, 2013.
- F. Gouaud, V. Rey, J. Piazzola, and R. Van Hooff, “Experimental study of the hydrodynamic performance of an onshore wave power device in the presence of an underwater mound,” *Coastal Engineering*, vol. 57, no. 11-12, pp. 996–1005, 2010.
- J. Gühring, “Dense 3d surface acquisition by structured light using off-the-shelf components,” in *Videometrics and Optical Methods for 3D Shape Measurement*, vol. 4309. SPIE, 2000, pp. 220–231.
- J.-E. Ha, “Automatic detection of chessboard and its applications,” *Optical engineering*, vol. 48, no. 6, p. 067205, 2009.

Bibliography

- O. Hall-Holt and S. Rusinkiewicz, "Stripe boundary codes for real-time structured-light range scanning of moving objects," in *Proceedings Eighth IEEE International Conference on Computer Vision. ICCV 2001*, vol. 2. IEEE, 2001, pp. 359–366.
- M. Hansard, S. Lee, O. Choi, and R. P. Horaud, *Time-of-flight cameras: principles, methods and applications*. Springer Science & Business Media, 2012.
- R. Hartley and A. Zisserman, *Multiple view geometry in computer vision*. Cambridge university press, 2003.
- T. H. Havelock, "The wave resistance of an ellipsoid," *Proceedings of the Royal Society of London. Series A, Containing Papers of a Mathematical and Physical Character*, vol. 132, no. 820, pp. 480–486, 1931.
- T. Heath, "A review of oscillating water columns," *Philosophical Transactions of the Royal Society A: Mathematical, Physical and Engineering Sciences*, vol. 370, no. 1959, pp. 235–245, 2012.
- T. Helsloot, "The development of a method to predict ship-bank interaction in real-time," 2016.
- E. Horn and N. Kiryati, "Toward optimal structured light patterns," *Image and Vision Computing*, vol. 17, no. 2, pp. 87–97, 1999.
- D. D. Hung, "3d scene modelling by sinusoid encoded illumination," *Image and Vision Computing*, vol. 11, no. 5, pp. 251–256, 1993.
- M. Ito and A. Ishii, "A three-level checkerboard pattern (tcp) projection method for curved surface measurement," *Pattern Recognition*, vol. 28, no. 1, pp. 27–40, 1995.

Bibliography

- M. F. Kazerooni and M. S. Seif, “Experimental study of a tanker ship squat in shallow water,” *Jurnal Teknologi*, vol. 66, no. 2, 2014.
- M. Kelemen, I. Virgala, L. Kelemenová, T. and Mikova, P. Frankovský, T. Lipták, and M. Lörinc, “Distance measurement via using of ultrasonic sensor,” *Journal of Automation and Control*, vol. 3(3), pp. 71–74, 2015.
- W. Kim, S. Van, and D. Kim, “Measurement of flows around modern commercial ship models,” *Experiments in fluids*, vol. 31, no. 5, pp. 567–578, 2001.
- V. Kozin and V. Zemlyak, “Study on wave resistance of a submarine moving under an ice sheet,” in *ISOPE International Ocean and Polar Engineering Conference*. ISOPE, 2012, pp. ISOPE–I.
- P. Lange, B. Jähne, J. Tschiersch, and I. Ilmberger, “Comparison between an amplitude-measuring wire and a slope-measuring laser water wave gauge,” *Review of Scientific Instruments*, vol. 53, no. 5, pp. 651–655, 1982.
- J. Lawrence, B. Holmes, I. Bryden, D. Magagna, Y. Torre-Enciso, J. Rousset, H. Smith, M. Paul, L. Margheritini, and J. Cândido, “D2. 1 wave instrumentation database,” *Work Package*, vol. 2, 2012. [Online]. Available: https://tethys.pnnl.gov/sites/default/files/publications/D2.01_Wave_Instrumentation_Database.pdf
- P. Malý and F. Lopot, “Qualisys system applied to industrial testing,” in *Experimental Stress Analysis 51*, ser. Applied Mechanics and Materials, vol. 486. Trans Tech Publications Ltd, 3 2014, pp. 135–140.
- M. Marino, I. C. Rabionet, and R. E. Musumeci, “Measuring free surface elevation of shoaling waves with pressure transducers,” *Continental Shelf Research*, vol. 245, p. 104803, 2022. [Online]. Available: <https://www.sciencedirect.com/science/article/pii/S027843432200156X>

Bibliography

- D. Marr and E. Hildreth, "Theory of edge detection," *Proceedings of the Royal Society of London. Series B. Biological Sciences*, vol. 207, no. 1167, pp. 187–217, 1980.
- M. Maruyama and S. Abe, "Range sensing by projecting multiple slits with random cuts," *IEEE Transactions on Pattern Analysis and Machine Intelligence*, vol. 15, no. 6, pp. 647–651, 1993.
- M. Mimou, T. Kanade, and T. Sakai, "A method of time-coded parallel planes of light for depth measurement," *IEICE TRANSACTIONS (1976-1990)*, vol. 64, no. 8, pp. 521–528, 1981.
- F. Moisy, M. Rabaud, and K. Salsac, "A synthetic schlieren method for the measurement of the topography of a liquid interface," *Experiments in Fluids*, vol. 46, no. 6, pp. 1021–1036, 2009.
- R. A. Morano, C. Ozturk, R. Conn, S. Dubin, S. Zietz, and J. Nissano, "Structured light using pseudorandom codes," *IEEE Transactions on Pattern Analysis and Machine Intelligence*, vol. 20, no. 3, pp. 322–327, 1998.
- U. Neumeier and C. L. Amos, "The influence of vegetation on turbulence and flow velocities in european salt-marshes," *Sedimentology*, vol. 53, no. 2, pp. 259–277, 2006.
- D.-Z. Ning, R.-Q. Wang, Q.-P. Zou, and B. Teng, "An experimental investigation of hydrodynamics of a fixed owc wave energy converter," *Applied energy*, vol. 168, pp. 636–648, 2016.
- K. L. Oliveras, V. Vasani, B. Deconinck, and D. Henderson, "Recovering the water-wave profile from pressure measurements," *SIAM Journal on Applied Mathematics*, vol. 72, no. 3, pp. 897–918, 2012.

Bibliography

- J. Pages, J. Salvi, R. Garcia, and C. Matabosch, "Overview of coded light projection techniques for automatic 3d profiling," in *2003 IEEE International Conference on Robotics and Automation (Cat. No.03CH37422)*, vol. 1, 2003, pp. 133–138 vol.1.
- R. Pinkel and J. Smith, "Open ocean surface wave measurement using doppler sonar," *Journal of Geophysical Research: Oceans*, vol. 92, no. C12, pp. 12 967–12 973, 1987.
- J. L. Posdamer and M. D. Altschuler, "Surface measurement by space-encoded projected beam systems," *Computer graphics and image processing*, vol. 18, no. 1, pp. 1–17, 1982.
- M. Rabaud and F. Moisy, "Ship wakes: Kelvin or mach angle?" *Physical review letters*, vol. 110, no. 21, p. 214503, 2013.
- M. Rufli, D. Scaramuzza, and R. Siegwart, "Automatic detection of checkerboards on blurred and distorted images," in *2008 IEEE/RSJ International Conference on Intelligent Robots and Systems*. IEEE, 2008, pp. 3121–3126.
- J. Salvi, J. Batlle, and E. Mouaddib, "A robust-coded pattern projection for dynamic 3d scene measurement," *Pattern Recognition Letters*, vol. 19, no. 11, pp. 1055–1065, 1998.
- J. Salvi, S. Fernandez, T. Pribanic, and X. Llado, "A state of the art in structured light patterns for surface profilometry," *Pattern Recognition*, vol. 43, no. 8, pp. 2666–2680, 2010. [Online]. Available: <https://www.sciencedirect.com/science/article/pii/S003132031000124X>
- A. J. N. A. Sarmiento and A. F. d. O. Falcão, "Wave generation by an oscillating surface-pressure and its application in wave-energy extraction," *Journal of Fluid Mechanics*, vol. 150, p. 467–485, 1985.

Bibliography

- A. Sarmiento, “Wave flume experiments on two-dimensional oscillating water column wave energy devices,” *Experiments in fluids*, vol. 12, no. 4-5, pp. 286–292, 1992.
- T. Sato, “Multispectral pattern projection range finder,” in *Three-Dimensional Image Capture and Applications II*, vol. 3640. SPIE, 1999, pp. 28–37.
- R. Szeliski, *Computer vision: algorithms and applications*. Springer Nature, 2022.
- J. Tajima and M. Iwakawa, “3-d data acquisition by rainbow range finder,” in *[1990] Proceedings. 10th International Conference on Pattern Recognition*, vol. 1. IEEE, 1990, pp. 309–313.
- T. Tezdogan, A. Incecik, and O. Turan, “A numerical investigation of the squat and resistance of ships advancing through a canal using cfd,” *Journal of marine science and technology*, vol. 21, pp. 86–101, 2016.
- R. Tsubaki and I. Fujita, “Stereoscopic measurement of a fluctuating free surface with discontinuities,” *Measurement Science and Technology*, vol. 16, pp. 1894–1902, 2005.
- R. J. Valkenburg and A. M. McIvor, “Accurate 3d measurement using a structured light system,” *Image and Vision Computing*, vol. 16, no. 2, pp. 99–110, 1998.
- M. Vantorre and G. Delefortrie, “Behaviour of ships approaching and leaving locks: Open model test data for validation purposes,” in *3rd International Conference on Ship Manoeuvring in Shallow and Confined Water: with non-exclusive focus on Ship Behaviour in Locks*. Flanders Hydraulic Research, 2013, pp. 1–16.

Bibliography

- M. Vantorre, G. Delefortrie, K. Eloot, and E. Laforce, “Experimental investigation of ship-bank interaction forces,” 2003.
- T. Vergote, K. Eloot, M. Vantorre, and J. Verwilligen, “Hydrodynamics of a ship while entering a lock,” in *3rd International Conference on Ship Manoeuvring in Shallow and Confined water: with non exclusive focus on ship behaviour in locks*. Flanders Hydraulic Research, 2013, pp. 1–9.
- P. Vuylsteke and A. Oosterlinck, “Range image acquisition with a single binary-encoded light pattern,” *IEEE Transactions on Pattern Analysis and Machine Intelligence*, vol. 12, no. 2, pp. 148–164, 1990.
- X.-l. Wang, G. Wei, H. Du, and S.-d. Wang, “Reconstruction of 3-d surface waves generated by moving submerged sphere based on stereo imaging principle,” *Journal of Hydrodynamics*, vol. 32, pp. 139–147, 2020.
- S. Wilson-Haffenden, M. Renilson, D. Ranmuthugala, E. Dawson *et al.*, “An investigation into the wave making resistance of a submarine travelling below the free surface,” *Australian Maritime College, Launceston*, 2009.
- H. Wu, J. He, H. Liang, and F. Noblesse, “Influence of froude number and submergence depth on wave patterns,” *European Journal of Mechanics-B/Fluids*, vol. 75, pp. 258–270, 2019.
- F. Xue, W. Jin, S. Qiu, and J. Yang, “Wake features of moving submerged bodies and motion state inversion of submarines,” *IEEE Access*, vol. 8, pp. 12 713–12 724, 2020.
- , “Airborne optical polarization imaging for observation of submarine kelvin wakes on the sea surface: Imaging chain and simulation,” *ISPRS Journal of Photogrammetry and Remote Sensing*, vol. 178, pp. 136–154, 2021.

Bibliography

- Z.-M. Yuan, “Ship hydrodynamics in confined waterways,” *Journal of ship research*, vol. 63, no. 01, pp. 16–29, 2019.
- L. Zhang, B. Curless, and S. M. Seitz, “Rapid shape acquisition using color structured light and multi-pass dynamic programming,” in *Proceedings. First International Symposium on 3D Data Processing Visualization and Transmission*. IEEE, 2002, pp. 24–36.
- R. Zhang, S. Draycott, I. Gyongy, D. M. Ingram, and I. Underwood, “A novel contactless technique to measure water waves using a single photon avalanche diode detector array,” *Proceedings of the Royal Society A*, vol. 477, no. 2247, p. 20200457, 2021.
- S. Zhang, “High-speed 3d shape measurement with structured light methods: A review,” *Optics and Lasers in Engineering*, vol. 106, pp. 119–131, 2018.
- X. Zhang and C. S. Cox, “Measuring the two-dimensional structure of a wavy water surface optically: A surface gradient detector,” *Experiments in Fluids*, vol. 17, no. 4, pp. 225–237, 1994.
- Y. Zhang, Q.-P. Zou, and D. Greaves, “Air–water two-phase flow modelling of hydrodynamic performance of an oscillating water column device,” *Renewable Energy*, vol. 41, pp. 159–170, 2012.
- Z. Zhang, “A flexible new technique for camera calibration,” *IEEE Transactions on pattern analysis and machine intelligence*, vol. 22, no. 11, pp. 1330–1334, 2000.